Atomic Force Microscopy Characterization of Hydrogen Terminated Silicon (100) 2x1 Reconstruction

by

Taleana Huff

A thesis submitted in partial fulfillment of the requirements for the degree of

Master of Science

Department of Physics
University of Alberta

Abstract

Non-contact Atomic Force Microscopy (NC-AFM) is a Scanning Probe Microscopy tool offering unique non-perturbative analysis of surfaces and adsorbates at the atomic scale. AFM precisely oscillates a sharp tip above a sample. By monitoring the shift in resonance frequency of a quartz tuning fork caused by local changes in the tip-sample interaction potential, distinct forces due to electrostatic, van der Waals, or chemical interactions can be extracted and quantitatively analyzed.

Hydrogen terminated silicon (100) 2×1 (H:Si(100)) has already been explored as a surface for nano-electronic applications using other analysis techniques such as STM, where exploitation of dangling bonds acting as atomic silicon quantum dots have been investigated for uses in quantum cellular automata based nano-electronics, [1] [2] [3], ultra-fast wires [4] [5], and logic gates [6]. H:Si(100) also provides a promising platform for electronically decoupled examination of adsorbed atoms, physisorbed molecules [7] [8] [9], and chemisorbed molecular structures with organic electronics applications [10].

Despite these potential uses, studies of H:Si(100) using AFM have been rarely done in the literature, and only once has it been experimentally imaged [11]. NC-AFM is a valuable complementary form of analysis that would give access to unique

information on H:Si(100) such as unperturbed surface charge distributions, chemical bonding, and surface forces. Therefore, this thesis presents atom resolution images of H:Si(100) achieved in both constant frequency shift and constant height modes of NC-AFM.

As part of this analysis, AFM capabilities first had to be developed in our low-temperature ultra-high-vacuum system, and were optimized over many months of research, trial, and error. Stable operation was attained, and constant frequency shift images of H:Si(100) were taken first to compare to the one published image result [11]. Constant height AFM analysis had never been published on H:Si(100), and was explored next.

Constant height scans taken at incremented tip-sample distances above the surface, a novel analysis, demonstrate the evolution from attractive to repulsive surface forces, with repulsive forces showing the first observation of the chemical bond structure of H:Si(100).

Furthermore, site-specific force spectroscopy reveals unique force profiles for different surface locations. These differences have application in subtraction of background forces for aformentioned molecule or atom examination, as well as strongly contribute to our understanding of the surface structure of H:Si(100).

Imaging of the inert H:Si(100) surface highlights the sensitivity of our system, and opens the door for many other high-resolution AFM experiments.

This is how humans are:
We question all our beliefs,
except for the ones that we
really believe in, and those we
never think to question.

ORSON SCOTT CARD

Acknowledgments

I would like to foremost thank my supervisor, Dr. Robert Wolkow, for presenting me with the tools and inspiration to even complete this project. Your unfailing enthusiasm for physics is infectious. I hope that I have, at a minimum, proven that I can patch a bicycle tire, as well as write a thesis under your guidance and support.

I am also very indebted to Dr. Hatem Labidi, who was pivotal in developing our AFM. You are a wonderful mentor and friend. Thank you so much for sharing your precious time and knowledge with me, as well as correcting me when I went awry in the lab. I could not have done it without you.

Furthermore, I would like to thank our un-official AFM technicians Martin Cloutier, Mark Salomons, and Jason Pitters. Thanks for helping work out the kinks as they arose.

Also, a big thanks to the other members of our SPM research group: Marco Taucer, Roshan Achal, Moe Rashidi, Bruno Martins, Mohammad Koleini, Lucian Livadaru, Paul Piva, John Wood, and Radovan Urban. You made the lab a supportive, informative, and fun environment.

Last, I would like to thank my mom Debbie, my brother Tarlin, and my family for all their understanding and support. I love you all and appreciate everything you have done to help me get here.

Contents

List of Figures

xi

Chapter 1

Introduction

1.1 The History of AFM

Atomic force microscopy (AFM) is a relative newcomer to the scanning probe microscopy (SPM) field in the atom-resolution regime. First detailed in 1986 by inventors Binnig, Quate, and Gerber [22] their paper on AFM as a new SPM technique quickly went on to become one of the most cited papers in Physical Review Letters of all time. Arising from the need for a SPM technique that would be equally as effective on any material, AFM was a way to transcend the limitations imposed by Scanning Tunneling Microscope (STM) experiments where the surface of interest needed to be conductive. AFM extends the already vast applications of STM by acting as a sort of "finger" to gently probe and trace out the atomic structure of the surface. While simple in concept, the experimental challenges of AFM are complex and it took another decade to gain enough practical functionality to be a viable tool.

STM image interpretation is rather straightforward compared to AFM. In STM a conductive tip is approached within several Å of a conductive sample with an applied voltage (bias) between the two. This bias causes quantum mechanical tunneling of electrons between tip and sample through the vacuum barrier separating them, creating a measurable tunneling current. This tunneling current drops off as an exponential function of distance with a decay constant of about Å^{-1}, meaning

that a distance decrease between tip and sample of $\approx$ 100 pm results in roughly an order of magnitude increase in tunneling current [23]. With the size of an atom also being $\approx$ 100 pm, this means that the STM control scheme can be done on the presupposition that almost all tunneling current is going through the apex atom and to a good approximation, is independent of the shape and distribution of atoms near the tip apex. Conversely, AFM depends upon a much more complex interaction involving long ranged interaction among many tip and substrate atoms, with modeling procedures that evolved and improved over a period of many years.

The overall force acting on the AFM tip is a combination of many attractive and repulsive forces, each with a characteristic range of interaction and magnitude. On the attractive side, there are the long range electrostatic interactions, van der Waals, and magnetic dipole forces. In the repulsive regime, Pauli repulsion forces must be considered. The sum of these interactions leads to a non-monotonic force curve as seen in Fig. 3.1. Unlike STM, AFM scanning is not in general dominated by the apex atom. The long range character of some AFM forces mean tip atoms well removed from the apex can contribute to the sum of forces, necessitating care in the quantitative interpretation of AFM data.

A second problem is acquisition of force data. Typical peak forces are small on the order of nN, and must be acquired in short time intervals requiring high acquisition bandwidths. They can also change rapidly from repulsive to attractive with minor changes in position. This poses challenges in designing sensitive feedback signals for controlling AFM, as well as presents problems in obtaining a good signal to noise ratio (SNR).

Due to these complexities, even though AFM was invented in 1986 it took nearly 8 years to achieve true atomic resolution in vacuum. Early publications showed what appeared to be atom-resolved surfaces, but the lack of step edges and surface defects indicated it was not true single atom resolution [24] [25]. Step edges were first observed and published by Binning's student F. Ohnesorge in 1993 as seen in Fig. 1.1, but only using AFM in water where the van der Waals interaction of the tip with the water medium managed to cancel out the van der Waals interaction of the tip and sample enough to make imagining stable [12]. Though exciting, the principle

was one not easily applied to other samples.

The first true atomic resolution in vacuum was achieved in 1994 on Si(111)-7x7 as seen in Fig. 1.2 with a resolution of 6 Å lateral and 0.1 Å vertical by Franz J. Giessibl [13] using NC-AFM. The key to success was the implementation of a new dynamic scan style of AFM, an improvement over the previously used static AFM.
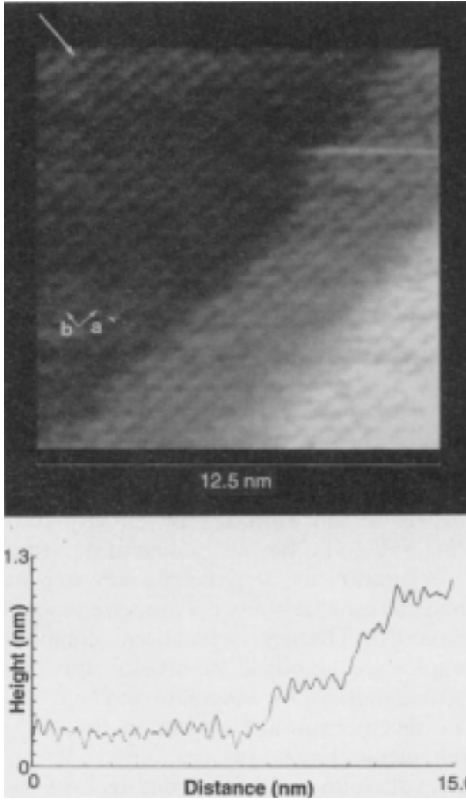
Figure 1.1: Constant Force AFM image in water of (1014) calcite with step edges proving true atomic resolution. Image size= 160 nm × 160 nm, V=-2.0, I=40 pA From [12].Reprinted with permission from AAAS.
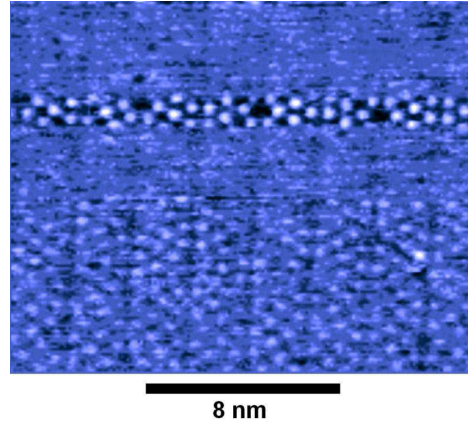
Figure 1.2: First AFM image showing atomic resolution with defects by Giessibl on Si(111)-(7 × 7). Imaging Parameters: k = 17 N/m, A = 34 nm, f_0 = 114 kHz, Δf =-70 Hz, Q = 28 000, and scan speed = 3.2 lines/s. Environment: ultra-high vacuum, room temperature. From [13]. Reprinted with permission from AAAS.

1.1.1 Static AFM

Before dynamic scanning, early AFM used a static method of imaging. A non-oscillating tip would be approached to the sample until a fixed deflection was detected, and feedback loops would change the z-height (the distance between tip and sample as seen in figures like 3.2) to keep that deflection. This deflection was small even when using low spring constant cantilevers, making it a difficult scanning mode. As mentioned before, the tip sample force is non-monotonic and can change between repulsive and attractive with very minor position changes. Regulating the z height precisely enough to not cause an instability in the feedback systems was challenging.

Cantilevers at that time also had very small spring constants meaning that if approached too close to the sample while scanning, the attractive force the sample could exert on the cantilever could become larger than the ability of the cantilever to resist. The sensor would be overwhelmed and pulled into the surface in what is colloquially termed a "jump to contact" event. All of this was fixed however by the adoption of both dynamic imaging and stiffer cantilevers.

1.1.2 Dynamic AFM: AM-AFM vs. FM-AFM

There are two types of dynamic AFM imaging: amplitude modulation(AM-AFM) and frequency modulation(FM-AFM). These scanning modes oscillate the cantilever at a fixed resonance frequency, allowing it to be modeled and regulated as a mass on a spring.

In AM-AFM the cantilever is excited at a fixed frequency near resonance with a known amplitude, with surface interactions registered as deviations thereof. To illustrate, driven slightly above the natural resonant peak for a sensor, an attractive force toward the surface would change the resonant frequency to a lower value. The frequency the excitation is acting on does not change, therefore the excitation is attempting to drive the cantilever far above the new resonance causing a decrease in amplitude. Conversely, if a repulsive force acts on the probe, the cantilever is being driven more toward resonance, increasing amplitude. Monitoring the amplitude variations, the sensor can be modulated. However, there are a few problems with

stably operating in this dynamic mode.

Large repulsive interactions can shift the resonance through and beyond the frequency the excitation is being applied at, to the point where it is exciting well off the resonance peak. This would decrease amplitude, falsely mimicking an attractive force. The feedback would compensate for this false signal by driving the cantilever harder, saturating the entire feedback loop and ruining the sensor through a tip crash. This is the AM-AFM dynamic "jump to contact".

A second problem with AM-AFM is it is not suited to high quality factor (Q) sensors. Tracking the amplitude is difficult if a high Q cantilever takes a long time to "ring down" to a stable amplitude value under change, necessitating very slow scan times. AM-AFM does have a few advantages though.

When compared to static scanning, it has much lower noise and reduced lateral force readings due to tip sample contact being broken during every oscillation cycle. Compared to FM-AFM, it also is a simpler control model with only one feedback loop being required for operation. Despite this, FM-AFM was used in preference to AM-AFM for all work presented because its advantages far outweigh its further challenges.

FM-AFM monitors changes in the resonant frequency and was a novel technique introduced by T.R. Albrecht et al. in 1991 [26]. This method requires multiple feedback loops to regulate a constant amplitude, phase, and either height or frequency shift depending on desired scanning method. Sensor oscillations on resonance are maintained by a phase lock loop (PLL), and amplitude and either z or Δf are managed by simple proportional/integral (PI) controllers as discussed in section 3.3. Coordinating the 3 feedback loops to work together can be a challenge, but has several distinct advantages.

A separate feedback loop for amplitude allows a record of any system damping of the oscillator, allowing examination of non-conservative forces. When doing quantitative analysis of a surface, Δf changes in constant height mode are easier to interpret from a quantitative analysis perspective as discussed in section 3.5. Finally, the AM-AFM "jump to contact" is not a problem in FM-AFM providing a stiff enough cantilever is used, as there is no way to saturate the feedback with false

values. This makes it easier to image rough or reactive features; an important capability for imaging highly reactive surfaces. With these advantages, FM-AFM quickly became the standard imaging mode in AFM, and a large push was made to image many different kinds of semi-conductors [27] [28] [29] [30] [31]. However, one problem remained.

Many of these studies continued to employ low spring constant cantilever designs. As mentioned earlier, these cantilevers have the unfortunate problem of not being stiff enough to resist the pull of attractive surfaces forces if brought too close, resulting in a jump to contact that causes a tip crash. To combat this, large oscillation amplitudes on the order of 10's of nm were used for early FM-AFM imaging with the idea that they would provide an energetic enough swing that could get out of the energy potential of the surface [32]. The problem with such large amplitudes is that they are much greater than the characteristic range of tip sample forces, effectively smearing them all together into a single Δf deflection contribution instead of allowing the targeted examination of different contributors through height regulation as discussed in section 3.1.1. Large amplitude scanning has now largely been abandoned in favor of small amplitude FM-AFM qPlus (a new sensor type discussed in detail in section 2.4.1) scanning and is the preferred method used by many prominent AFM groups.

1.2   NC-AFM Scanning of H:Si(100): Motivation

AFM has proven itself to be a marvelous tool for many different types of measurements. Recent work includes measuring the force needed to move an atom across a surface [33], the chemical identification of different adatom species from force spectroscopy [34], and three-dimensional force mapping of surfaces [35] [36]. One especially important result of AFM that influenced chosen analysis techniques on H:Si(100) in this work is shown below in Fig. 1.3.

Fig. 1.3 shows the detailed structure of the pentacene molecule obtained by constant height NC-AFM imaging by Gross et al. in 2012 sitting on a background surface. AFM has the capability to probe and display the delicate chemical bonds between atoms in this molecule, revealing unprecedented sub-angstrom resolution.
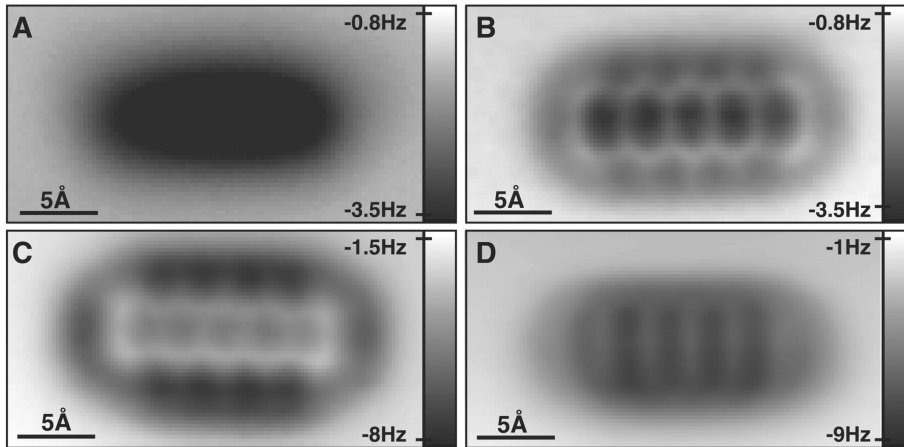
Figure 1.3: Constant-height AFM images of pentacene on NaCl(2ML)/Cu(111) using different tip modifications. (A) uses a Ag tip, (B) a CO tip (C) a Cl tip, and (D) a pentacene tip. The individual chemical bonds of the molecule are easily visible. From [14]. Reprinted with permission from AAAS.

This resolution is also obtained in what is, uniquely, a relatively non-perturbing way compared to other methods like STM which require a bias and tunneling current. AFM is superior to STM in these regards and should provide a beautiful and detailed examination of H:Si(100)-2 × 1. But, what is the motivation for a deeper examination of H:Si(100)?

1.2.1   H:Si(100) and Electronics Applications

Very extensive STM analysis on doped H:Si(100) has been conducted for years now as it offers an attractive surface for potential beyond CMOS nano-scale electronics implementations [2–6]; an idea being exploited by start-up company Quantum Silicon Incorporated [1]. This is due to the applications made possible by dangling bonds (DBs) which serve as atomic silicon quantum dots.

These dangling bonds can be fabricated with a STM or stationary AFM tip by careful positioning above a hydrogen capped silicon atom on the surface, followed by a voltage pulse. A pulse of +2.3 V for a few ms of time will break the bond between the silicon atom and hydrogen cap, creating a unsatisfied valence as shown in Fig.

1.4. With a very sharp tip, diverse, complex, and atomically precise patterns can be created, with one such special pattern being the quantum dot cellular automata (QCA) cell
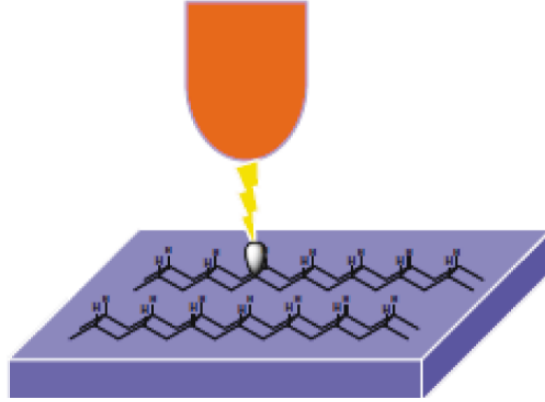
Figure 1.4: Individual hydrogen caps on H:Si(100) can be removed with atom precision using a sharp tip, and a voltage pulse. This voltage pulse removes the hydrogen, leaving a dangling bond behind that can act as a silicon quantum dot.

Quantum Dot Cellular Automata

Quantum dot cellular automata cells were a concept introduced by Lent and co-workers in 1993 [37,38]. These QCA cells can achieve classical binary logic functions using geometric arrangements of polarized cells.

Fig. 1.5 (a) shows an atomic scale QCA cell created by removal of H atoms from H-terminated silicon. Two electrons are symmetrically shared between all four dangling bonds in the QCA cell, and these electrons are free to tunnel between all cell DBs [2, 3]. This symmetric distribution can be disturbed by the addition of nearby control charge as shown in Fig. 1.5 (b) from work done by Haider et al. [15]. Polarization of the electron density along a specific diagonal is assigned to be either a binary 0 or 1. Multiple cells can be aligned in a row to create a binary wire as shown in Fig. 1.6.

The individual cells are far enough (≈ 8 Å) away from each other to not quantum tunnel couple, but close enough to exert electrostatic interactions. Therefore, when
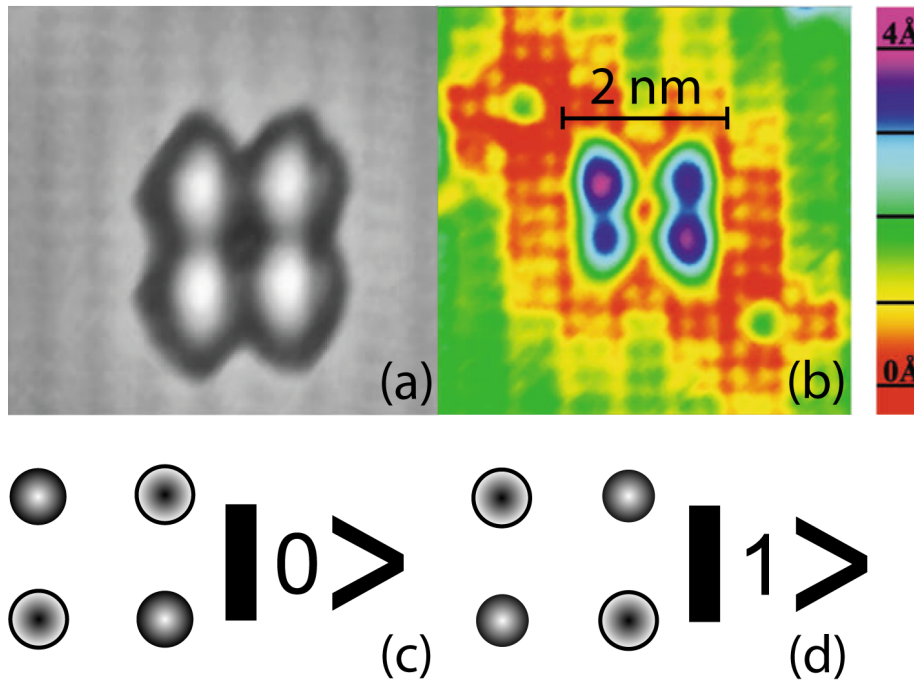
Figure 1.5: (a) Symmetrical QCA cell made of an assembly of 4 dangling bonds on H:Si(100). Electrons are shared uniformly. (b) A QCA cell polarized by the addition of two perturbing DBs on the diagonal [15]. Perturbing DBs are far enough away to only exert electrostatic interaction on the QCA cell, pushing electron density into the darker blue DBs. Reprinted with permission from APS. (c) and (d) are the two possible assigned binary states of a QCA cell. If polarized with electron density in the upper left and lower right, it represents a computational 0. Conversely, a computational 1 can be transmitted.
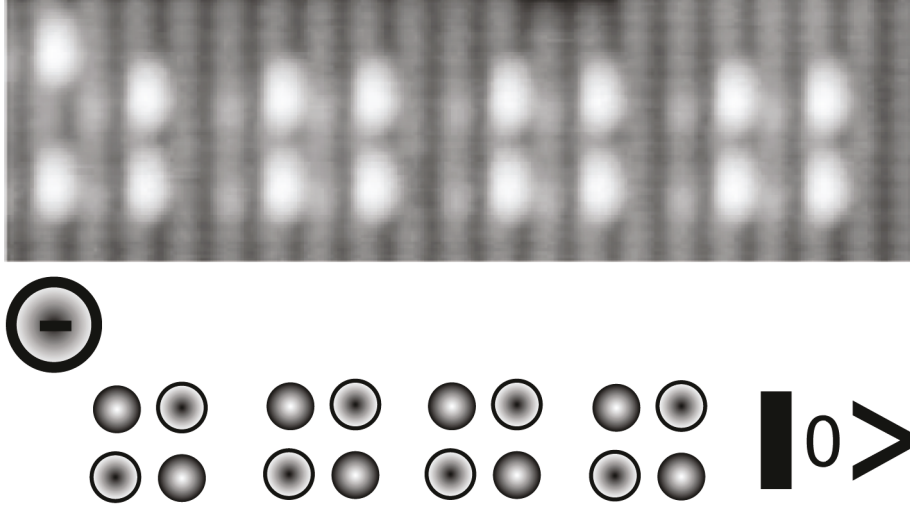
Figure 1.6: A line of QCA cells without perturbing charge (Top). This chain of QCA cells can be polarized all the way down the line by a theoretical control charge at one end as depicted below (Bottom). The control charge shifts the electron density in the first cell, which then shifts it likewise in the second cell, etc.

an input cell is forced by a perturbing charge or input electrode to be in one binary configuration, adjacent cells copy that pattern to transfer the input state to the other terminus. Clever geometrical shaping of these binary wires can be used to make inverters, majority gates, and other necessary modules for computation [1]. These QCA circuits made of DBs on H:Si(100) have the advantages of being ultra fast and ultra-low power [3]. An AFM study of H:Si(100) and DBs will give further insight into these applications, as AFM can probe information inaccessible to STM.

As mentioned earlier, STM probes through a tunneling current after a bias is applied between a conductive tip and sample, and is perturbative if trying to extract information about the surface such as the charge distribution. Conversely, AFM doesn't disturb the native distribution of surface forces and can image without bias. It probes several kinds of surface information ranging from electrostatic forces to chemical bonds. Information about these force's uniformity and strength in a non-perturbing manner will be a valuable asset to further research on DB based QCA structures.

Also, H:Si(100) is considered a difficult to image surface for AFM due to its inert nature. Achieving reliable atomic resolution on it with NC-AFM in our system is proof of our technique and sensitivity, opening the door for many future AFM projects as detailed in section 5.1.

Chapter 2

Experimental Techniques

2.1 LT-STM/AFM setup

All experiments were carried out using a commercial system Omicron [39] operating at low temperature (LT) and ultra high vacuum (UHV). The system allows performance of both STM experiments with a regular tip, or dual STM/AFM with a qPlus AFM sensor described in 2.4.1. This commercial machine was complemented with home-built sample and tip storage, tip processing, and sample processing chambers, which are the preparation (Prep), field ion microscopy (FIM), and hydrogen termination (H-Term) chambers respectively.

Due to the sensitive nature of experiments where picometer level precision is needed for measurements, the system is well isolated from building vibrations. As pictured in Fig. 2.1, the machine is on its own separate floor pad in a quiet basement lab. A solid steel slab supports the chambers, which is in turn supported by 4 pneumatic legs that act to minimize any vibrational coupling between the slab and floor. Cables running to power supplies and other instrumentation are insulated using suspended long rubber tubing for vibration damping. These measures attenuate vibration noise by a factor of approximately 100 in the 2-100 Hz range as measured by an accelerometer. As to the function of each sub-chamber, the system consists of 4 separate areas overall, each with a specific purpose.
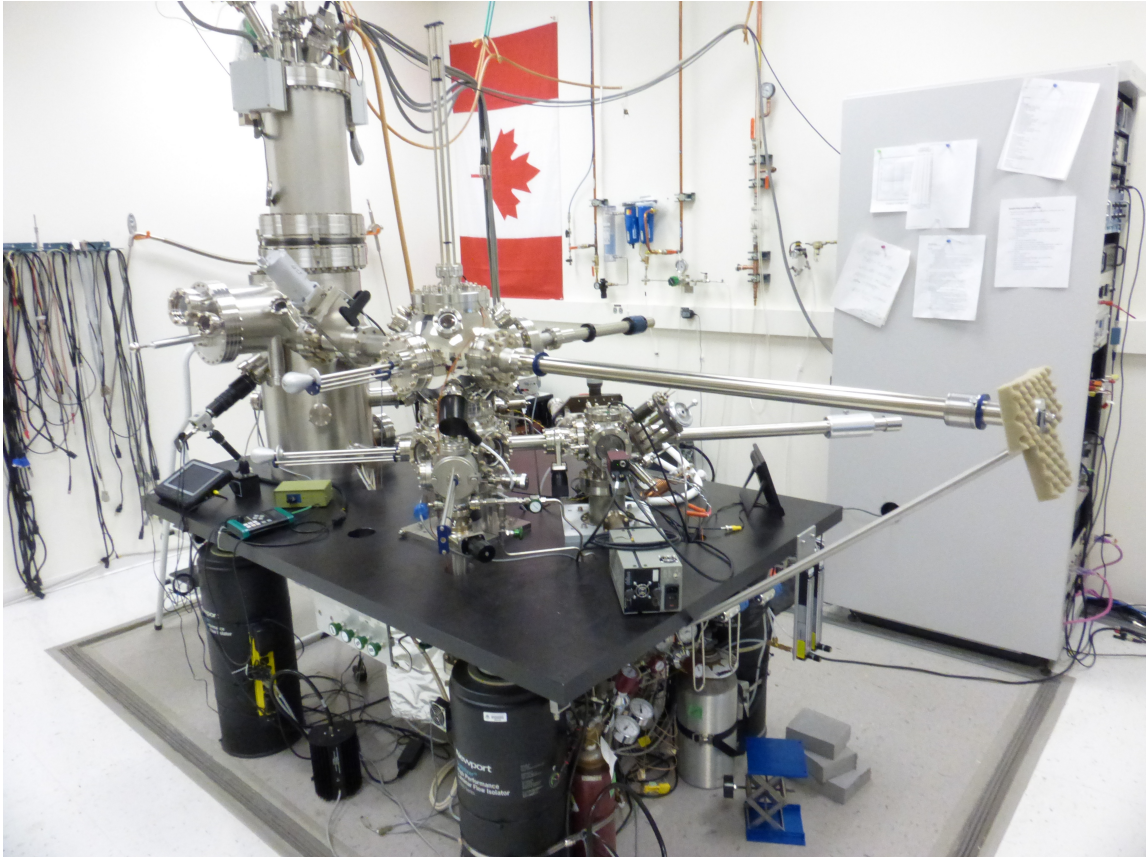
Figure 2.1: Omicron STM/AFM

2.1.1 The Preparation Chamber and Load Lock
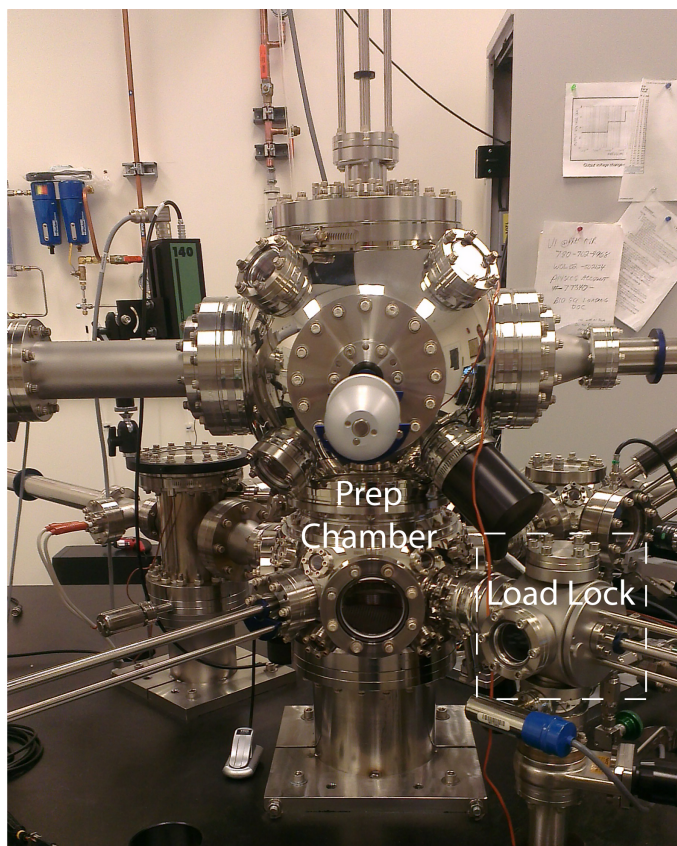
Figure 2.2: Home-built Preparation chamber with attached Load-Lock for inserting and removing samples or tips.

The preparation chamber as seen in Fig. 2.2 has pressures in the 10^{-10} Torr range and acts as a central hub, storage area, and loading center for tips and samples. The scanning, FIM, and H-termination chambers are all satellite to it, with UHV vacuum gates separating the chambers.

There is a storage carousel centered inside the preparation chamber as seen in Fig. 2.3 with slots for up to 6 tips or samples. Transfers of tips and samples to other chambers from Prep are accomplished through a system of "wobble sticks" as seen in Fig. 2.4 and sliding transfer arms as seen in Fig. 2.1. However, before storage

Figure 2.3: Tips and Samples are stored in this carousel by sliding them in to holding tabs.

or processing, tips and samples must be loaded into UHV which is accomplished through the attached load-lock as highlighted in Fig. 2.2.
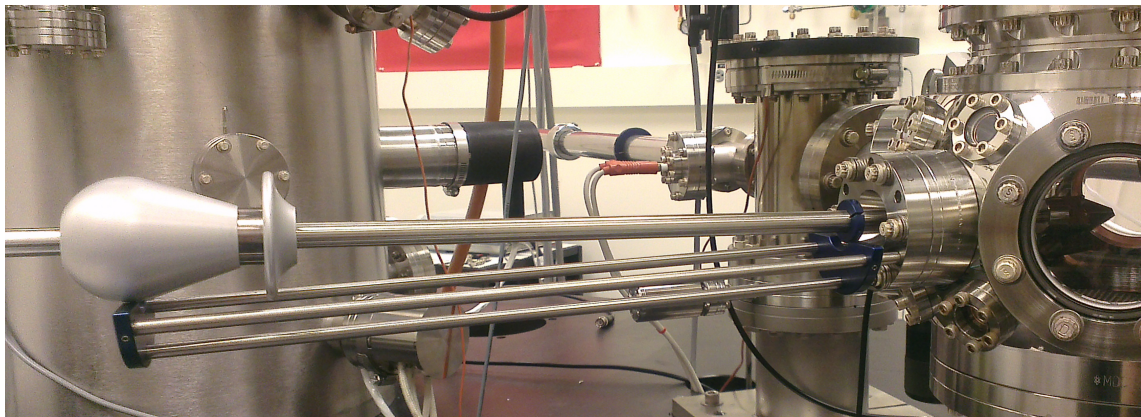
Figure 2.4: Wobblesticks can be used to pick up and place samples or tips for transfer to the various processing and scanning chambers.

Sample/Tip Loading

Samples or tips are not directly introduced into the Prep chamber for two reasons. First, having a separate chamber that can be pumped out avoids having to break vacuum every time something is loaded. Secondly, many contaminants are difficult to remove once introduced; having a load-lock prevents most contamination entering the UHV system.

The load-lock chamber has a hinged door with a sliding transfer arm centered in it. Tips or samples are loaded by clean tweezers into slots on the sliding arm, and the hinged door is closed and sealed. A roughing pump is used to bring the load-lock chamber down from atmospheric pressure to $\approx 10^{-3}$ Torr. With the chamber pressure sufficiently low, a turbo pump is then run for 40 minutes to further reduce the Load-Lock pressure to $\approx 10^{-9}$ Torr; a value low enough to then open the Prep chamber gate valve without introducing undue contamination or breaking vacuum. Once loaded, tips or samples are stored in the Prep chamber or moved to the appropriate processing chamber.

2.1.2   The Field Ion Microscopy Chamber
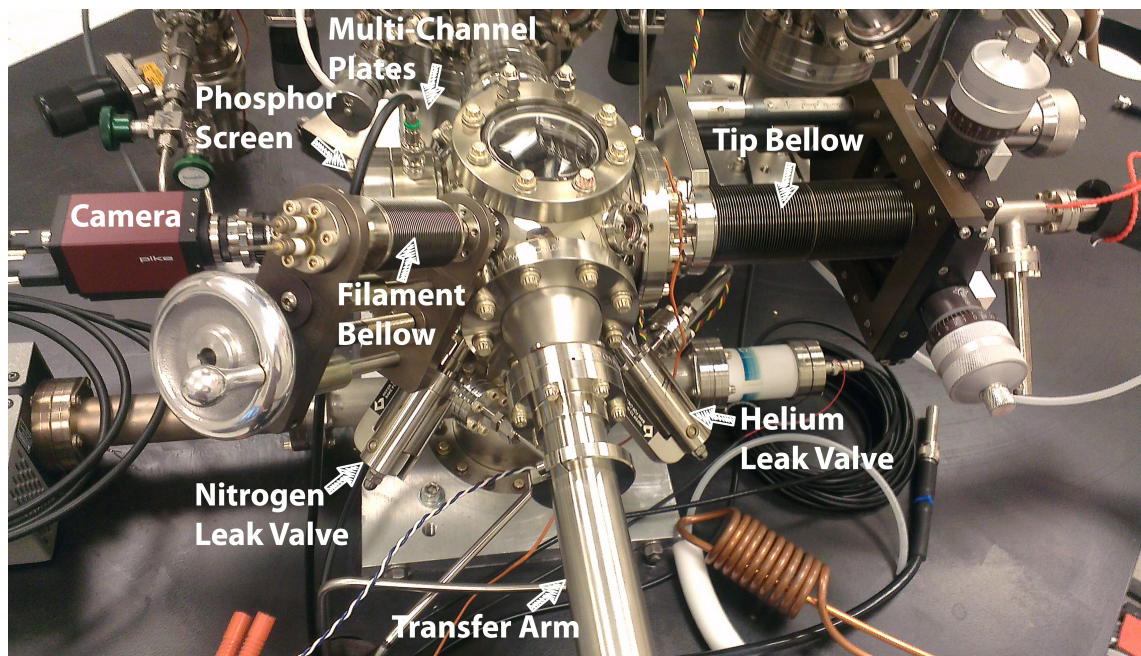
Figure 2.5: Field Ion Microscopy Chamber set-up.

The field ion microscopy chamber is used entirely for tip preparation and serves 3 important functions: tip cleaning, tip imaging, and tip etching; with the specifics for all talked about in section 2.4.

For tip cleaning, the main instrumentation to be aware of in Fig. 2.5 are the filament and tip bellow. Applied bias and currents on each through appropriate wiring allow for the critical cleaning by means of field emission and electron beam processing from section 2.4.4.

Imaging the tip structure is accomplished through the combination of the phosphor screen, multi-channel plate, and camera, allowing capture of a clear macroscopic view of the changing atomic structure of the tip with field ion microscopy explained in section 2.4.5.

For in-situ tip etching, nitrogen and helium are necessary gases leaked in to a precise pressure using the labeled leak valves. Etching allows the creation of sharp

tips with methodology outlined in section 2.4.6 [40].

2.1.3 The Hydrogen Termination Chamber

The surface of interest for all experiments is the hydrogen terminated silicon (100) surface also known as H:Si(100). Samples loaded into UHV though the load-lock are bare Silicon(100) covered in a protective oxide layer that must be removed and replaced by hydrogen. This is all accomplished in the hydrogen termination chamber which has pressures in the 10^{-11} Torr range.

Similar to the FIM chamber, the H-termination chamber also has a tungsten filament. This filament pictured in Fig. 2.6 is used for cracking diatomic H_2 into H atoms which terminate the silicon surface. The filament is degassed before bringing the oxide covered sample into the chamber by running 1.7 A of current through it until it no longer degases and raises the overall pressure in the chamber. With a clean filament, the sample is brought in and slid into the holder pictured in Fig. 2.6. Conductive fingers rest on top of the molybdenum plates that clamp down over the thin strip of sample, an important arrangement for degassing the sample through resistive heating as part of the termination process detailed in section 2.3.

Also similar to the prep chamber, the hydrogen leak valve allows precise introduction of hydrogen gas into the sealed chamber during the hydrogen termination process.

2.1.4 The Scanning Chamber

After proessing, tips and samples are loaded into the scanner in the scanning chamber where all AFM and STM experiments are conducted. The scanner is also the only part of the system which operates at liquid helium temperatures, with an average operation temperature of ≈ 4.5 K.

For successful high-resolution scanning probe microscopy, a vibration decoupling system is employed on the nestled scanner in the scan chamber. The scanning stage seen in the bottom right of Fig. 2.7 is suspended by three soft springs when scanning, with an inherent resonance of 2 Hz. The machine has a natural frequency much
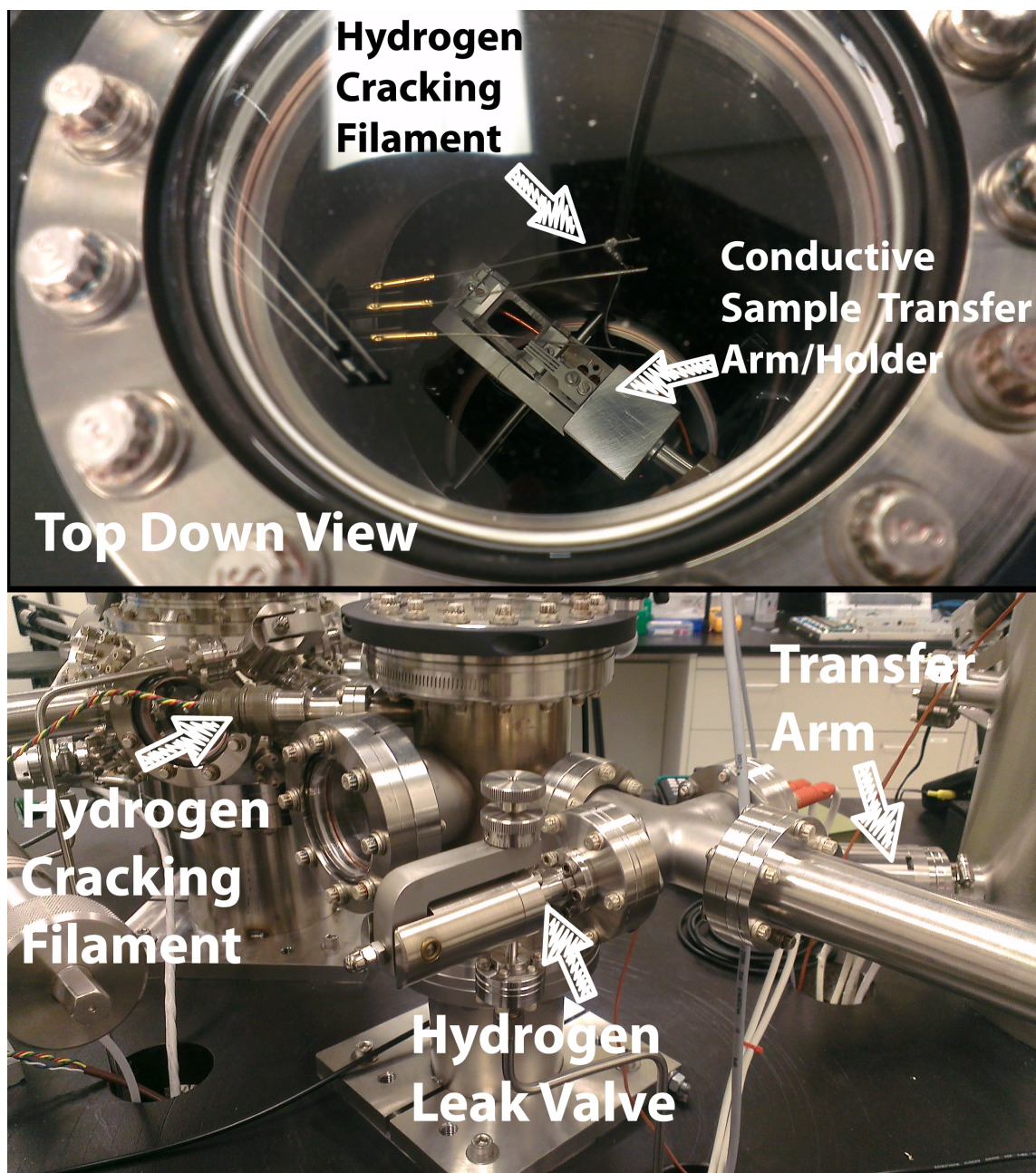
Figure 2.6: Hydrogen Termination Chamber set-up.
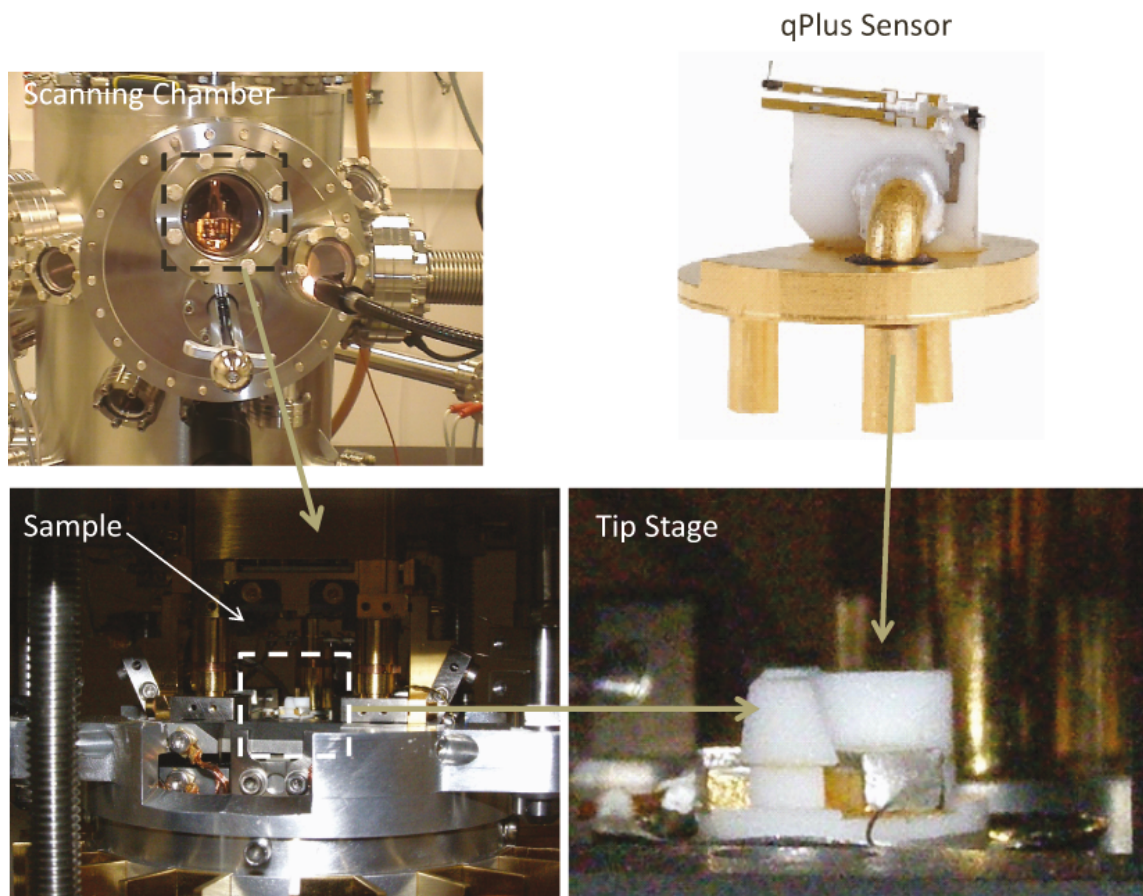
Figure 2.7: Scanning Chamber set-up with outside view (top left), inside view(bottom left), tip stage (bottom right), and a qPlus tip (top right).

higher than 2 Hz usually on the order of kHz. This difference in suspension resonance versus machine resonance means a very small transfer function to the scanning unit for intermediary frequencies.

Lateral vibrations of the tri-spring suspended scanning stage are mediated by a eddy current damping mechanism. This mechanism works by having copper spokes mounted to the scan stage pass between permanent magnets fixed to the copper container at the bottom of the LHe cryostat that the scanning stage sits in. The spokes and scanning assembly are shown in Fig. 2.8.
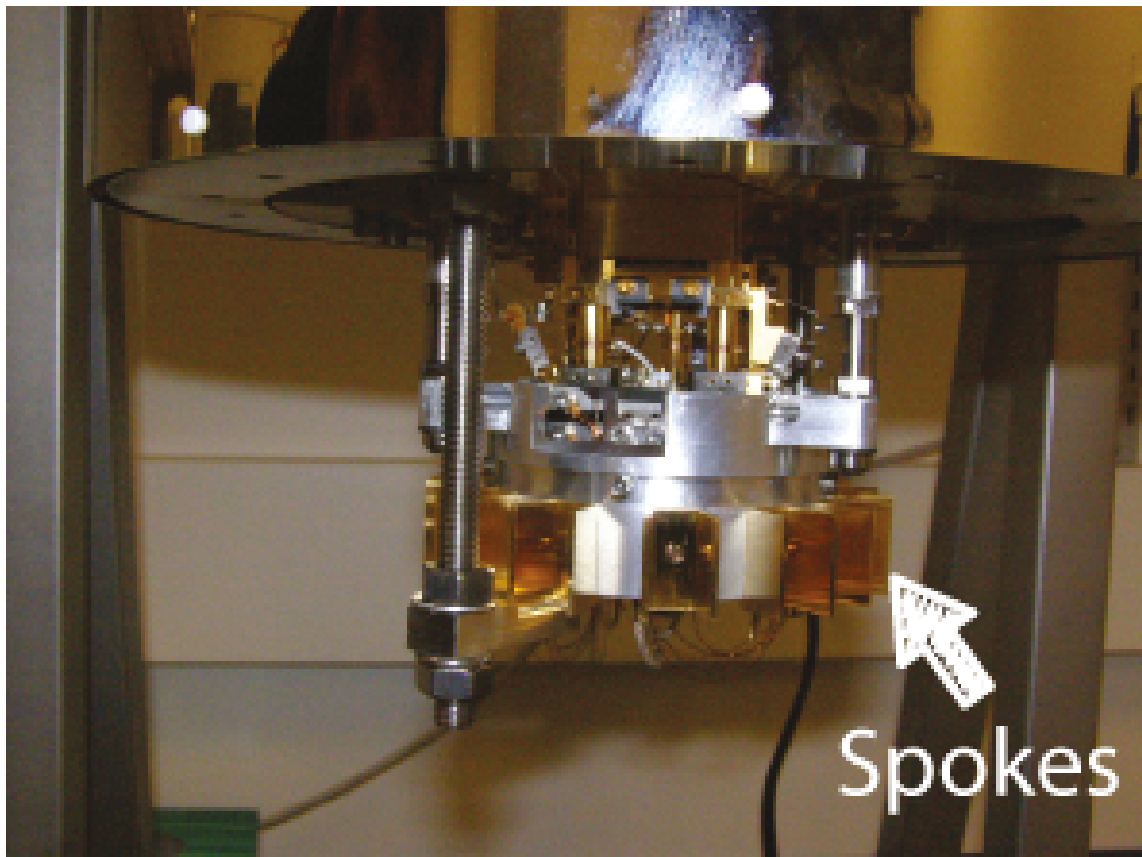
Figure 2.8: View of the scanning chamber out of vacuum with highlighted gold plated lateral motion damping spokes.

The scanner sits in two cryostats which keep it at 4.5 K, with a more detailed discussion of cryogenics explained in section 2.2.

The tip sits on a piezoelectric stage as pictured in the lower right of Fig. 2.7, which allows fine movement in all 3 axial directions. The stage also has conductive pads to apply bias and read currents from the "legs" of the tip holder, which are coated in gold to enhance conductivity for these signals or readings.

The hydrogen terminated sample slides into a slot directly above the tip pictured in the lower left in Fig. 2.7. The tip is approached toward the stationary sample using a coarse linear motor to start, followed by a fine approach using the piezos.

2.2   Cryogenics

Low temperature has many benefits for AFM and STM. Most importantly, it allows for stable scanning for long periods of time with minimal thermal drift. Thermal drift is caused by temperature fluctuations affecting different materials in the scanner uniquely. Each material has its own coefficient of thermal expansion which will react differently to these fluctuations, undesirably moving the tip, smearing acquired images, and adding noise. Having stable low temperatures eliminates this thermal noise providing crisp images and keeping the tip exactly where placed on the sample. With an average AFM scan taking 20 minutes for a 5×5 nm frame, and dozens of scans being required over single features at precisely set heights, this is a very important benefit.

A second advantage to LT is it allows continued use of even reactive samples like un-terminated Si for weeks at a time. LT keeps pressures for contaminants low, keeping samples clean.

Third, LT has implications for AFM sensor minimum force gradient detection. Lower temperatures increase the Quality factor of cantilevers, which affect the sensitivity as $1/\sqrt{Q}$. Temperature itself also factors in as its own variable as $\sqrt{T}$ [26]. A detailed analysis of these considerations is given in section 3.3.1. To achieve low temperatures in the system, the scanner is housed in two concentric bath style cryostats. The outer cryostat is filled with liquid nitrogen (LN_2) and serves as a cost effective shielding cryostat. LN_2 by itself is able to bring internal scanner temperatures down to 77 K. The second cryostat is liquid helium (LHe) and reduces the temperature

further to 4.5 K. LHe has a temperature of 4.2 K, but the small temperature gradient across the instrument places the average operating temperature at 4.5 K. Protected by the outer cryostat, helium is lost at a much lower rate, saving cost in the long run.

The spring suspension and eddy current damping system mentioned in 2.1.4 are directly mounted to the LHe cryostat, cooling to 4.5 K by conduction. The entire Scanning Chamber rests in a copper cup also connected to the LHe bath, ensuring the SPM is surrounded by cold surfaces allowing it to stay in thermal equilibrium.

Radiative heat transfer for an object changes according to the Stefan-Boltzmann Law with q being the heat transfer in Watts, σ being the Stefan-Boltzmann Constant, T the absolute temperature in K, and A the area of the emitting body in m^2:

$$q = \sigma T^4 A \tag{2.1}$$

Keeping the surrounding temperature for the scanner at 4.5 Kelvin reduces the heat load on the scanning chamber drastically, keeping undesirable effects such as thermal drift to a minimum.

As a final measure to ensuring stable LT operation, both cryostats are shielded by gold coated IR doors conductively cooled to LN_2 temperatures. These doors can be opened for placement of samples or tips, and are closed while scanning.

2.3   Surface Preparation

H:Si(100) samples were all highly doped with arsenic to a concentration of $10^{19}\frac{atom}{cm^3}$ and a resistivity of 0.003-0.004 Ωcm. Samples must be mounted onto a special carrier plate before being loaded in UHV as pictured in Fig. 2.9.

To fit on the plate, some out of vacuum processing is first done on a sample wafer. Samples must be cleaved to an appropriate size which is done in a laminar flow dust free hood using a sapphire scribe, glass microscope slides to guide the scribe, ceramic tweezers to move and place the sample, and a molybdenum wrench to tighten the holder screws. Sapphire and ceramic are used instead of metal based
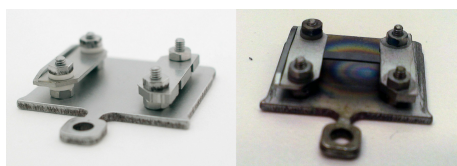
Figure 2.9: UHV compatible molybdenum clamped sample holder (left) and mounted cleaved silicon sample (right).

tools to prevent surface contamination. Stainless steel has nickel in it which shows up as row defects during the reconstruction and termination process [41]. The holder itself is also constructed of molybdenum for the parts in contact with the sample as molybdenum atoms are less mobile and do not lead to surface contamination.

Samples are cut to a length of 11 mm, and a width of between 1.5-3 mm. Thinner samples are preferred as they give a more uniform temperature gradient over the sample area when resistively heated, an important component to ensure the desired 2×1 reconstruction occurs everywhere on the wafer during termination.

Once mounted and clamped in to the carrier plate, samples are loaded into UHV through the Load-Lock as per section 2.1.1, and moved to the H-term chamber. Pressure in the H-term chamber is ensured to be in the middle 10^{-11} Torr at most.

The sample is slid into the slot shown in Fig. 2.6 so the conductive fingers touch the flat metal molybdenum plate on the top. A DC power supply is used to supply current through the fingers for heating, and an optical pyrometer calibrated for the emissivity of silicon is used to measure sample temperature. Current is increased until the pyrometer registers a sample temperature of 570 $°C$, and the sample is left to degas overnight. This temperature is chosen because any lower and the sample will not adequately degass, and any higher and the protective oxide can start being removed [42].

Once degassed, the oxide layer protecting the silicon wafer is removed through a series of high temperature flashes. Current is increased on the power supply quickly to raise the temperature of the sample to 1250 $°C$, a value higher than the oxide removal threshold for silicon of 900 $°C$ [42]. The threshold is surpassed as flashes at 1250 $°C$ also serve to remove other types of contamination like carbide from

the surface [43]. Care must be taken to not overdo flashing, as that can have the undesirable effect of reducing the doping concentration as reported by Pitters et al. [44].

Next, the DC current necessary to attain 570 K is found and recorded as the 2×1 reconstruction of H:Si(100) occurs optimally at this value [45] [46]. It is important to be at this temperature during termination as lower temperatures at 400 K and 300 K produce the 3×1 and 1×1 reconstructions respectively [47] [48],and higher temperatures will increase DBs and other surface defects as thermal desorption begins to compete with H adsorption [49].

With the 2×1 reconstruction temperature found, diatomic H_2 gas is added to the chamber until a pressure of 10^{-6} Torr is reached using the leak valve, and the cracking filament is turned on with a current of 1.7 A. The hot cracking filament splits the leaked in diatomic H_2 into H atoms which are free to make a bond with the surface.

A final flash of the surface is done at 1250 $°C$, and then immediately dropped to the 2×1 reconstruction temperature of 330 $°C$. The termination is allowed to continue for 2 minutes, after which the resistive heating is shut down and the H_2 leak valve is closed. UHV pressure is allowed to recover in the chamber after termination, and the sample is rapidly transferred to the scanner to prevent contamination.

In the 2×1 reconstruction, every surface silicon is able to make a total of 4 bonds; 3 with other silicon atoms, and one with the desired hydrogen cap during the termination process above. Two hydrogen capped silicon atoms bonded together are called a dimer as shown in Fig. 2.11, which are arranged into dimer rows. A large area STM scan of of the H:Si(100) surface after termination is shown in Fig. 2.10, and a more highly magnified view of a terminated area is shown in Fig. 2.11.
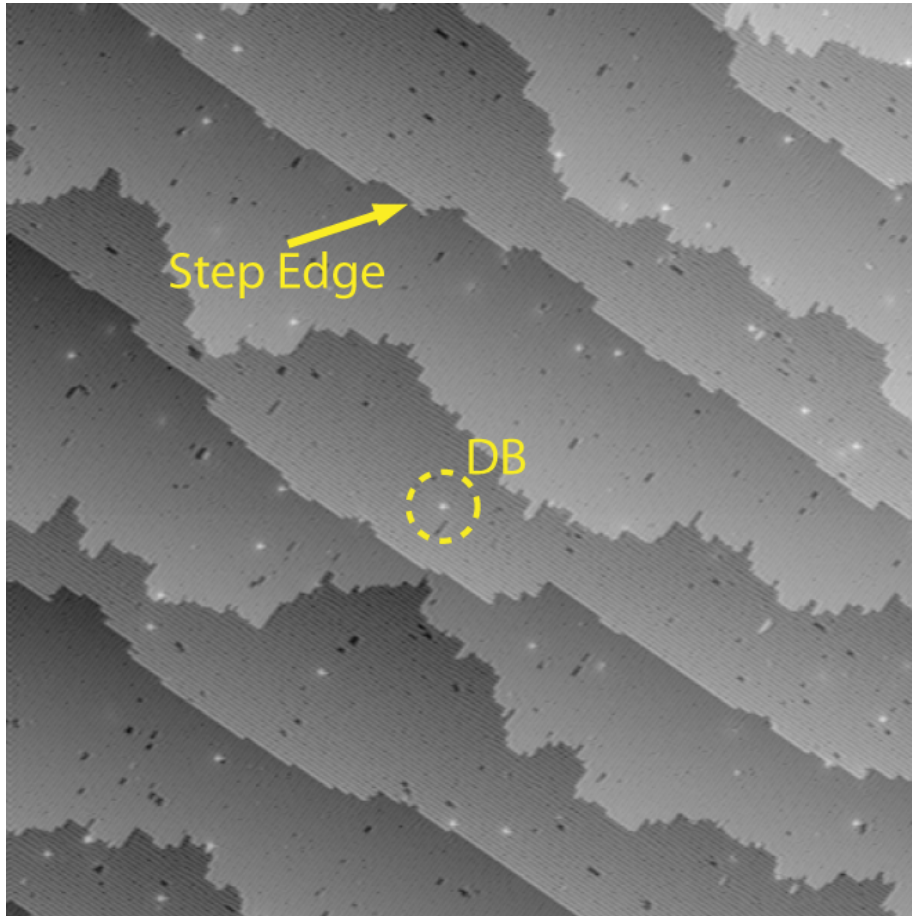
Figure 2.10: A large area 160nmx160nm STM image of the H:Si(100) surface showing step edges and defects from the termination process V=-2 V I=30 pA.
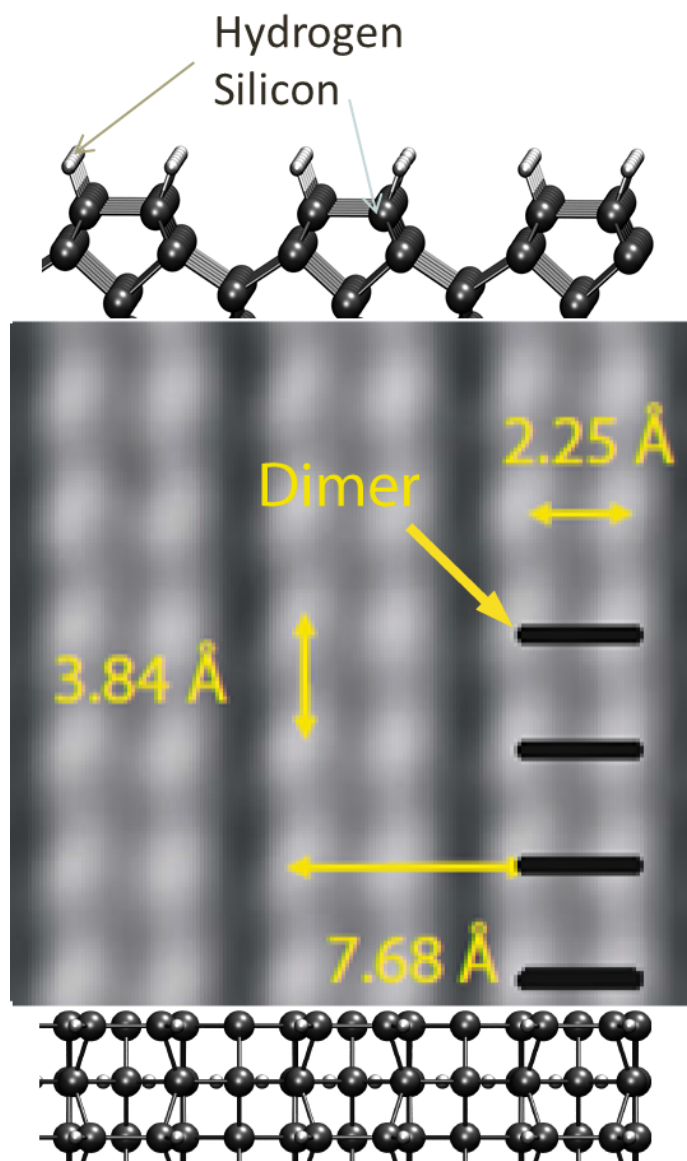
Figure 2.11: (Top) A ball and stick model cross-section of H:Si(100). (Middle)Magnified STM image of the H:Si(100) 2×1 reconstruction of dimers and rows with listed topographic spacing. (Bottom) Top down ball and stick view of H:Si(100).

2.4 Tip Preparation

2.4.1 qPlus Sensors

Many different kinds of sensors exist for AFM applications. The first AFM sensor was hand fabricated from gold foil with a diamond tip [22]. Shortly thereafter, micro-fabrication of tips from SiO_2 and Si_3N_4 became popular [50]. Now, many different types of sensors are used from silicon to metallic, all fabricated in a multitude of ways.

Figure 2.12: A commercially ordered qPlus sensor. The quartz tuning fork has one prong glued to a ceramic stage, while the other has a conductive metal tip glued to the conductive gold patterning on the side.

The sensor used for all experiments presented herein is the qPlus sensor as pictured in Fig. 2.12. This sensor was pioneered by F.J Giessibl in 1998 [51] and consists of a quartz tuning fork with one prong rigidly glued to a ceramic stage, making it more of a quartz cantilever in practice. The quartz tuning fork itself is actually a remnant of the watch manufacturing industry where they are used as a frequency standard.

This design has 5 particular unique properties that make it especially suitable for NC-AFM which are its thermal stability, piezoelectric nature, high stiffness, high

Quality factor, and high resonance frequency f_0. These forks are rugged under just about any temperature, preserving their inherent mechanical properties such as resonance frequency f_0 down to even LT temperatures with only small variations [52]. Their stability under temperature fluctuations makes for an excellent resistance to thermal noise, as the cantilever is less sensitive to small excitations caused by thermal fluctuations in the scanner. It also makes modeling of the sensors easier as the parameters of the sensor can be treated as constant under UHV LT scanning conditions.

Next, their self-sensing nature due to the piezoelectricity of quartz makes interpretation of data convenient. Oscillations on the fork induced by shaking the z-piezoelectric element which the sensor is mounted on generates a periodic voltage across the electrodes patterned on the sides of the fork. This voltage is then processed by a charge amplifier, and perturbations in the voltage from surface interactions are correlated to a measured frequency shift. This is an improvement over older detection designs such as the very common optical beam detection system.

Beam detection works by laser light being reflected off the cantilever and detected by a position sensitive detector [53]. These systems are often hard to calibrate accurately for amplitude, as well as difficult to implement in a UHV LT environment.

qPlus sensors also have the advantage of being very stiff with a spring constant k=1800 N/m. As touched on in section 1.1.2, jump-to-contact is a problem for all other sensors. If the surface can exert a larger potential than the cantilever is capable of overcoming, the cantilever will be pulled into the surface and ruined. 1800 N/m when combined with even small amplitudes is stiff enough to overcome most surface potentials [32], while at the same time not being too stiff so as to make unmeasurably small deflections.

Finally, qPlus sensors have exceptional quality factors and resonance frequencies, two attributes that play heavily into its force sensitivity as explained in section 3.3.1. Atomic resolution is easier for these sensors due to these attributes playing into the minimum detectable force gradient.

2.4.2 Tip Structure

Tip structure is of large importance in the imaging quality of AFM. As explained in section 3.1.1,some interaction forces in AFM operate over a large distance, acting far up the tip. Having sharp tip character is important to reduce the contribution of long range and neighboring atom forces and thereby give higher resolution images.

Tip material is another important aspect of tip structure, and can affect the primary imaging mechanism. In AFM with a silicon tip, contrast is dominated by the formation of covalent bonds with the surface [54] [55]. CO functionalized tips, pioneered by researchers at IBM Zurich [14], are a more non-reactive variation where use of the Pauli repulsion dominated regime has given exceptional resolution [56]. Finally, metal tips are generally non-reactive, but can have large induced dipoles [57] [58] as a result of the Smoluchowski effect [59].

With these considerations in mind and knowing that a method of producing narrow single atom tips from tungsten was introduced by Rezeq et al. in 2006 [60] [61], Tungsten (W (100)) tips were chosen for all experiments. This process which reduces atoms from the tip to produce a sharp tip character is discussed in section 2.4.6.

W also is a conductive medium, which was an important property as it opens the field for simultaneous AFM and STM scanning, assists with tip processing in STM mode to achieve good imaging, and also could be important for future quantum dot charging experiments as done by Leo Gross and Stomp [62] [63]. Before sharpening through our group's single atom process, tips must be loaded into UHV first.

2.4.3 Mounting and Chemical Etching

qPlus sensors can be purchased with or without a mounted tip. Purchased with-tip qPlus sensors showed a wide variation in the quality of sharpness of the tip, often being dull with a large radius of curvature. Therefore, a method to mount and etch tungsten qPlus tips was developed.

First, small sections of W (100) wire are cut as short as possible to still be able to be handled by a pair of narrow tweezers, but long enough to be dipped into epoxy

and mounted. These small sections average about 2-3 mm in length, with a diameter of 0.1 mm. When cut, they are ready for mounting.

Mounting

Conductive epoxy is used to mount the tips to the gold patterning on the side of the qPlus sensor seen in Fig. 2.12. Once the epoxy is mixed, it stays malleable until cured which is done after the mounting process. There are two routes that can be used to mount the tip: (1) by hand, or (2) by using a sensitive multi-axial placement device.

To mount by hand, tips are picked up using clean narrow tweezers, lightly dipped in the epoxy, and gently placed on the tuning fork. The epoxy has enough adhesiveness that the extra light tip remains where placed. Care is taken not to add too much epoxy during placement, as the extra mass load introduced can drastically reduce the resonance frequency of the sensor in turn decreasing force sensitivity as discussed in section 3.3.1 with a $\sqrt{f_0}$ dependence. Tips are then cured in the oven at a temperature of 120 $°C$ for 15 minutes. This is a fast efficient way to make large batches of tips.

To mount by placement device, first the small section of tip is inserted into a hollow needle holder pictured in Fig. 2.13. The multi-axial set-up has full fine x, y, and z motor motion for both the epoxy needle and qPlus sensor holder. A secondary needle coated in wet epoxy is carefully brought next to the held tip, and dipped in using the fine motor control to coat it in epoxy. Next, the bare tuning fork sensor is inserted into a special magnetic holder also pictured in Fig. 2.13, and the sensor is maneuvered so the epoxy coated tip contacts the conductive gold patterning on the side. The whole positioning section is easily removed from the multi-axial placement device as a singled module, and inserted into the oven for curing at 80 $°C$ for 1.5 hours as shown in Fig. 2.14. Low temperatures and long curing times are used to prevent de-magnetization of the detachable tip holder module during the curing process.

When compared to hand mounting tips, this process is more time consuming
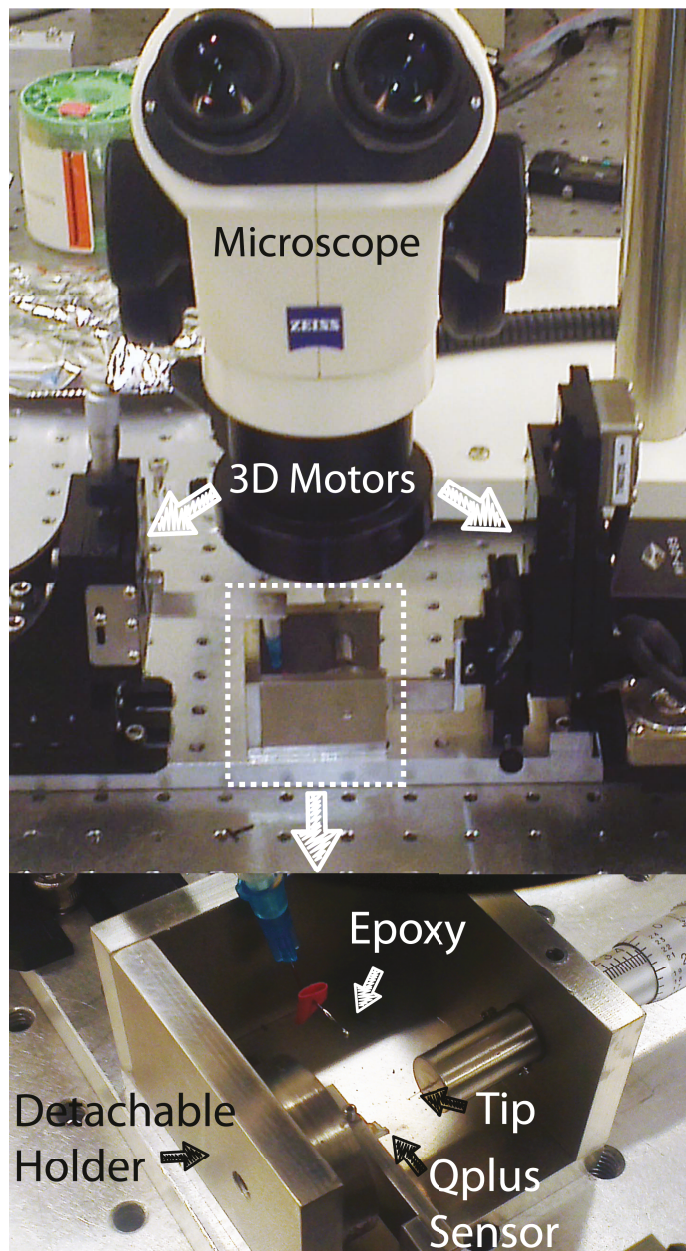
Figure 2.13: Multi-axial tip placement device.
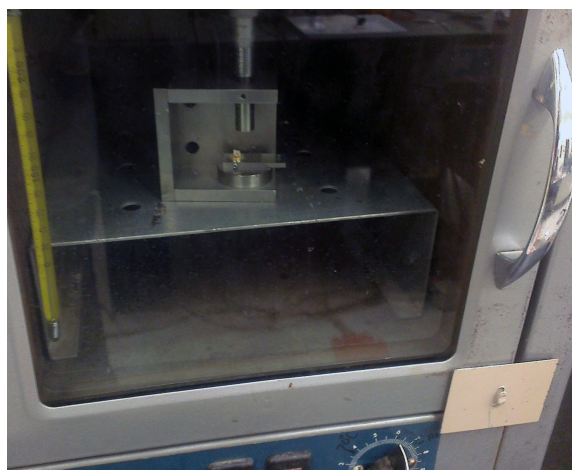
Figure 2.14: Detachable tip placement device with epoxied tip curing in the oven.

with only one tip made at a time. However, the advantages of using less epoxy resulting in better force sensitivity and having excellent manufacturing consistency outweigh the time commitment. Therefore hand mounting was used during early AFM experimentation as many tips were crashed while learning the AFM technique. Now, with careful use an AFM tip can last many weeks, so the multi-axial placement device is primarily used.

Chemical Etching

To achieve an exceptional AFM tip, the eventual goal is to in-situ image and sharpen it in the field ion microscopy chamber. To image the tip using field ion microscopy (FIM), the tip must be somewhat sharp to start with so that strong electric fields, a key element of FIM, can be applied to the tip apex at reasonable voltages. Therefore, tips are first electrochemically sharpened in a NaOH solution [64] [65].

The W tip serves as an anode and a W wire in the solution acts as the cathode. The experimental set-up is shown in Fig. 2.15 and a schematic of the tip etching is shown in Fig. 2.16. The tip is dipped in the solution and a voltage is applied. This etches any submerged part of the tip, with sharpening coming in at the air-solution interface where etching preferentially occurs. The lower part of the wire will

33
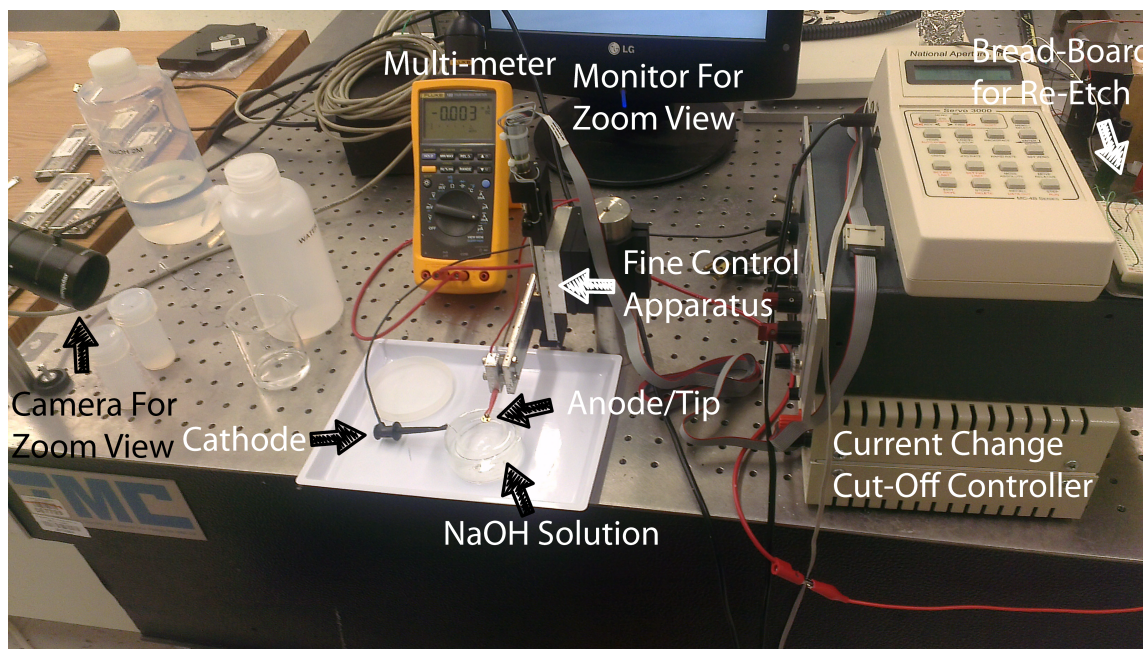
Figure 2.15: Tip etching experimental set-up.
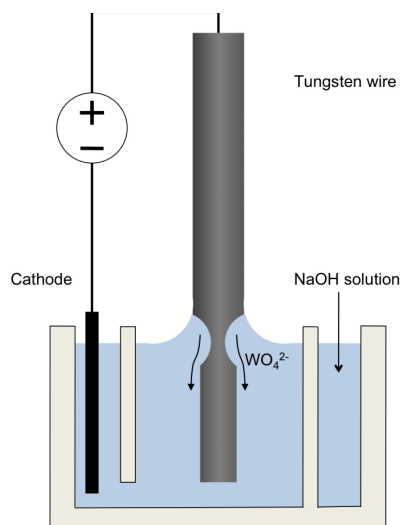
Figure 2.16: Schematic of the tip etching process for producing sharp tungsten tips [16]

eventually break off when the shank becomes very thin, producing a large change in current between the cathode and anode. The etching circuit is designed to look for a particular large ΔI, after which it stops the reaction. This etching process leaves behind a very sharp tip with a radius of curvature of $\approx$ 10-20nm [60].

Figure 2.17: qPlus sensor mounted in the fine control motor above the NaOH etching solution

To etch a mounted qPlus tip, the sensor is first attached to a fine control motor used to precisely immerse the tip as seen in Fig. 2.17. Next, a cleaning etch is done on the shank of the tip to remove any amorphous contaminants that may have resulted from handling or curing. This is done by fully immersing the tip, starting the etch reaction, and slowly drawing it out of the solution. Once clean, the tip is ready for the sharpening etch.

The tip is inserted into the etch solution maximally to ensure as much of the mounted mass is removed as possible for a high resonance f_0. The etch is started and allowed to continue until the current change from the drop of the bottom portion occurs. Once completed, the etched mounted tip is removed and dipped in water to remove any remaining NaOH. The quality of the etch is evaluated under an optical microscope at 50x magnification to check for any obvious defects. If none are observed under an optical microscope, it is ready to be loaded into UHV as per section 2.1.1 and in-situ etched further to a single atom as detailed in section 2.4.6.

With commercially purchased with-tip qPlus sensors, these are ready to be used in UHV right out of the box provided they are good, but for defective ones, one experimental adaptation was made.

qPlus Re-etch

Purchased tips that are of low quality, or used tips damaged from scanning can be re-etched to sharpen them again. The procedure is reminiscent of the regular etching procedure described in the above section, but requires one special adaptation.

Figure 2.18: The bread-board circuit used to extend the current cut off abilities of the etching set-up.

Commercially produced tips use very thin diameter tungsten. While great for the weight saving implications, the etch electronics have trouble measuring the small cur-

rent between cathode and anode. To remedy this, a special home-made breadboard circuit was used as pictured in Fig. 2.18.

This breadboard extends the current change detection capabilities of the system to detect the very small ΔI generated by a thin tip dropping off. Trying to etch thin tips without this extra circuit results in the etch reaction proceeding too far and rounding of the tips.

2.4.4   Field Emission and Electron Bombardment

With a tip loaded into the Field Ion Microscopy chamber detailed in section 2.1.2, the tip is ready to be cleaned, viewed, and further sharpened.

First, sharpness of the tip is checked by testing field emission. Field emission is a way to check the quality of the electrochemical etch through ejection of electrons from the tip. A voltage is applied to the tip, generating an electric field at the apex. If this field is large enough, electrons can tunnel through the confining barrier of the tip and eject into the vacuum. Sharp tips will require less of an applied voltage to reach the critical electric field for electron ejection than a dull one [66] [67] [68]. The procedure for testing field emission is as follows.

The tip is positioned very close to the degassed filament shown in Fig. 2.5 which is connected to an oscilloscope. A DC power supply applies voltage to the tip until the critical electric field for electron ejection is reached. Some ejected electrons are collected by the filament, which are amplified by a current to voltage amplifier and then registered as a current value on the oscilloscope. The applied voltage is adjusted until 10 nA of current is observed, which for sharp tips will be sub 500 V. Field emission also has the effect of cleaning the tip through Ohmic heating of the narrow cross section near the tip apex.

The tip is next heated by electron bombardment. The filament is connected to a DC power supply, and a +500 V bias is applied to the tip. The filament current is increased until a desired response current, ≈ 5 mA, is observed on the tip. This is left for 5-30 seconds to allow electrons from the filament to bombard the tip, which have the primary function of heating the tip to remove oxide and other contaminants.

Care must be taken to not heat the tip past the failing point of the epoxy holding the tip on. After bombardment, the field emission threshold is again checked. A lower threshold and a more steady current trace indicate a sharper and cleaner tip. This cycle of alternating field emission and electron bombardment is repeated several times until the field emission voltage of the tip no longer decreases and the emission current appears stable when viewed on the oscilloscope. This indicates the tip is no longer getting sharper and cleaner. When this happens, the tip is ready to be examined in FIM.

2.4.5   Field Ion Microscopy

Field Ion Microscopy (FIM) was pioneered by Muller and Bahadur in 1955 [69]. It is an UHV analytical technique used to image the atoms on the apex of a sharp tip and was the first technique to allow individual atoms to be spatially resolved [70].

FIM places large stresses on the tip with kV of applied voltage, requiring the use of materials suitable to this condition. In addition, the material must field ionize less easily than the imaging gas used.

First, FIM requires a sharp tip to allow reasonable positive voltages to be used to generate a strong enough electric field at the tip, somewhat like field emission. However, the difference is the field for FIM is reversed in direction and $\approx 10\times$ larger as it must ionize the imaging gas. A suitable gas for W(100) is helium. The FIM chamber is filled to approximately 10^{-6} Torr with this imaging gas, which when it gets near the strong electric field of the apex, ionizes to form a positively charged ion. This positive ion accelerates away from the positive tip perpendicular to its position on the tip apex. These ions are collected by a multichannel plate and phosphor screen and are converted into photons that can be imaged by a camera. This results in a approximately million times magnification of the fine atomic structure of the tip [70].

To image a tip in our home-built FIM chamber, the tip is first approached to the multi-channel plate (MCP) pictured in Fig. 2.5 until it is ≈ 3 cm away. 2500 V is applied to the phosphorous screen seen in Fig. 2.5, and the MCP is set with a

38

voltage of -1700 V. The imaging gas used is Helium, which is dosed in to a pressure of 10^{-6} Torr.

With the qPlus tip cooled to LN_2 temperatures, voltage can be applied to the W tip to start imaging. The tip voltage required to image is usually on the order of 10-20 kV, and is slowly increased until an image appears. As helium comes near the strong field of the tip it is ionized and accelerated from the positively biased tip, toward the negatively biased MCP which is an array of electron multipliers. The secondary electrons exiting the MCP are then accelerated toward the phosphorous plate where they produce photons that are captured by a camera. Once seen, the tip can be etched as per section 2.4.6, or field evaporated until clean for immediate use.

Field evaporation is another cleaning technique where voltage is increased enough to directly evaporate W atoms from the tip with a high electric field. The large electric field reduces the binding energy of atoms near the surface, especially on irregular protrusions where there is a high radius of curvature.

2.4.6 Single Atom Etching

Single atom etching is a technique pioneered on W(100), and completed during the FIM process after the first image of the tip is visible on screen. Sharp tips are important for reducing long range force contributions as explained in section 2.4.2. There is some reason to think that tips do not stay single atom once sharpening crashes during scanning are done as discussed in section 3.4.1, but single atom etching was still completed on almost all tips with plans to explore its effects on AFM in the future.

Gaseous nitrogen is used to etch the tips as per the method pioneered by our group et al. [40, 60, 61] and is introduced into the chamber using the leak valve to a pressure of 10^{-6} Torr. The introduction of nitrogen gas causes a bright ring around the 2D projected image of the tip apex as imaged with FIM. This brightness indicates where the nitrogen is able to "attack" and etch.

The nitrogen etch is spatially specific. At the highest field point, the tip apex, N_2 is ionized and ejected away just as is the helium imaging gas. At the periphery of the

tip apex, where the field is lower, N_2 can chemically adsorb and dissociate to form strong W-N bonds. That reaction cause atomic asperities to form. Such protrusions become high field points which are subject to field evaporation, causing local etching. The circular etching zone eventually constricts to remove all but the central apex tungsten atom, leaving all other surface atoms terminated with a tungsten nitride monolayer.

To facilitate the tip etch stages seen in Fig. 2.19 for a W (111) STM tip, it is required that the voltage on the tip be lowered periodically to allow the nitrogen to attack farther up the shank. Fig. 2.19 (a) is the initial image of the tip corresponding to the finely dashed line in Fig. 2.19 (g). Reduction in voltage allows the bright attack ring to move up and become narrower as it etches away atoms closer to the apex. Therefore, the voltage is periodically reduced by increments of 300-500 V to allow more atoms to evaporate from the shank and perimeter of the apex. Key stages are shown in Fig. 2.19 (b)-(e), ending in a single atom tip in Fig. 2.19 (f).

When a single atom is observed, the nitrogen gas leak valve is shut off, the voltage on the tip is reduced to prevent field evaporation of the single atom, and the helium leak valve is closed. The chamber is allowed to pump out for several minutes until the pressure returns to UHV levels. The tip voltage is then shut off altogether, and the tip moved into the scanning chamber.
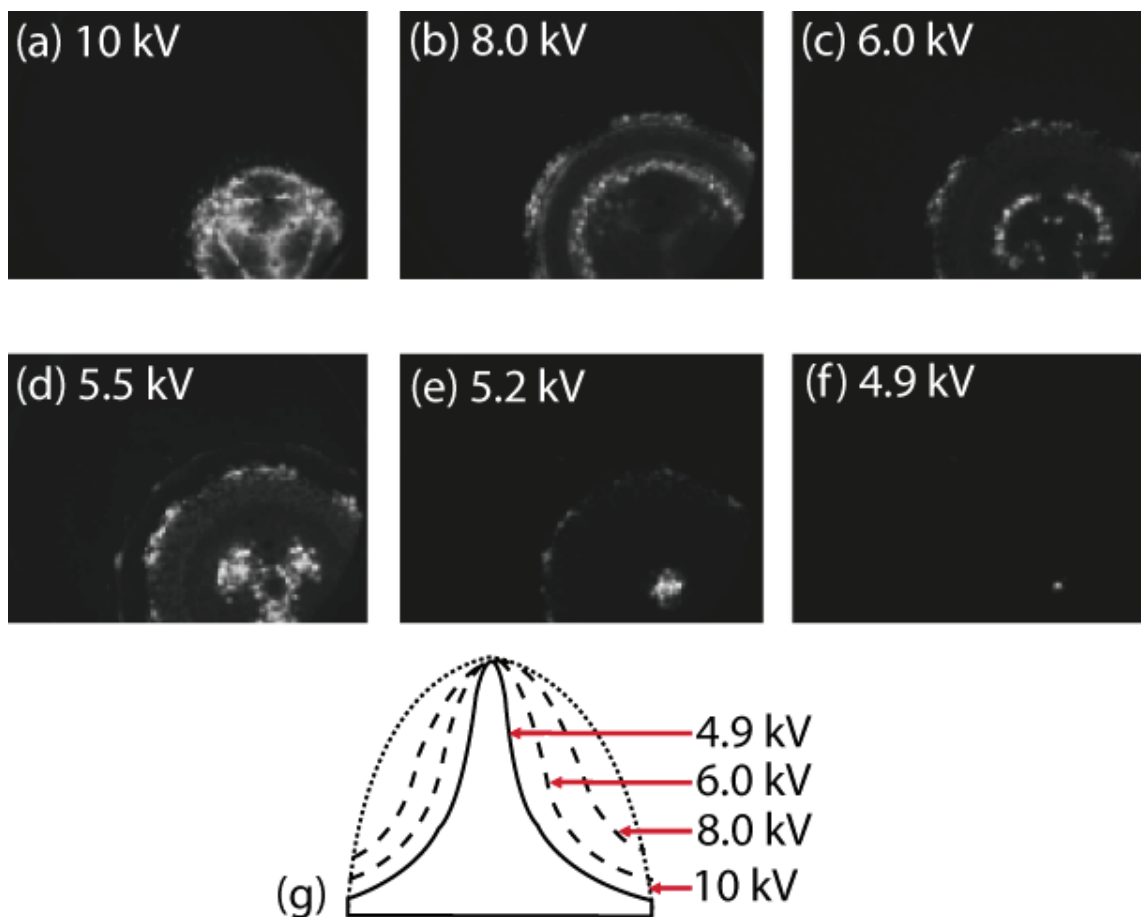
Figure 2.19: FIM etching sequence for a W(111) tip down to a single atom (a)-(f). Tip voltages are listed below each figure [16] and correlated to the visualization model in (g).

Chapter 3

NC-AFM Operations with a qPlus Sensor

Multiple parameters must be set for the electronics and calibrations done on the sensor before any scanning can begin with the loaded H:Si(100) sample and sharp qPlus sensor. To set and justify these values, some background on the modeling of non-contact AFM is necessary.

3.1   AFM Theory

Typical potential and force curves for a modeled apex and surface atom are shown in Fig. 3.1 (c) [17], along with an experimental Δf vs. distance curve Fig. 3.1 (b) for Si(111) 7×7 in NC-AFM [18].

The model in Fig. 3.1 (c) assumes a typical two atom interaction where Pauli repulsion and van der Waals forces are factored in to the approach of the two atoms as a typical potential energy curve. Comparing the shape of these simple theoretical plots to the experimental curve in Fig. 3.1 (b), it can be seen that the general shape of the interaction is similar, suggesting that similar forces are at work in real data [17].

To mathematically describe this interaction, we start with the idea that the tip-
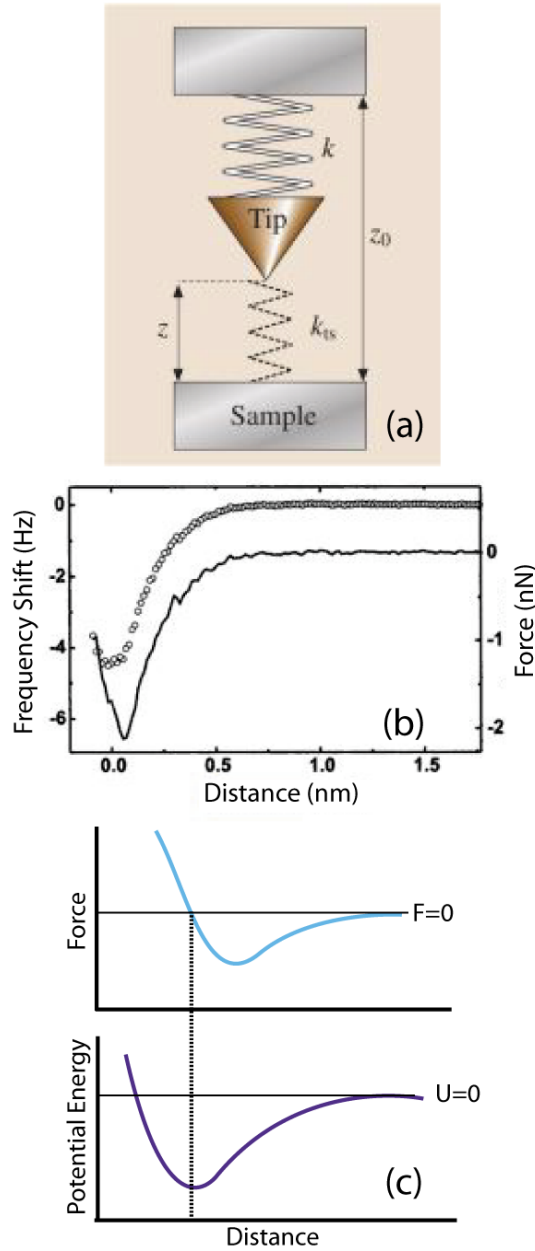
Figure 3.1: (a) The tip and sample interaction can be modeled as a mass with two competing springs k and k_{ts} which are the cantilever spring constant and the tip-sample spring constant. Reprinted from [17] with kind permission from Springer Science and Business Media. (b) A Δf vs. Distance curve and overlayed force vs. distance curve for a Si(111) 7×7 surface approached with a Si cantilever from [18] with kind permission from Springer Science and Business Media. (c) Potential energy and force relationship for a surface atom interacting with a tip atom.

sample interaction can be modeled as a mass with two competing springs as shown in Fig. 3.1 (a) from [17]. The force from a single spring can be expressed by:

$$F = kx \tag{3.1}$$

Two spring are chosen because the tuning fork has its own spring constant k, but the surface also has an inherent competing spring constant, also referred to as the tip-sample force gradient, designated k_{ts}. k for the cantilever remains constant as it is a property of the sensor overall. However, the tip-sample spring constant k_{ts} is not. Looking at force Fig. 3.1 (c) and knowing from equation 3.1 the relationship between force and displacement, we see that the relationship is not linear and k_{ts} changes:

$$k_{ts} = \frac{-\partial F_{ts}}{\partial x} \tag{3.2}$$

A plot of k_{ts} from a simulated potential curve modeled by Welker et al. is shown below in Fig. 3.2, which has the same general shape of the potential and force. This is a problem for modeling.

If k_{ts} was constant, then the tip sample interaction k_{total} would simply be the sum of the two spring constants.

$$k_{total} = k + k_{ts} \tag{3.3}$$

This total could be substituted into the general equation for the eigen frequency f_0 for a cantilever of known spring constant k and mass m:

$$f_0 = \frac{1}{2\pi}\sqrt{\frac{k}{m}} \tag{3.4}$$

So that f_0 becomes:

$$f_0 = \frac{1}{2\pi}\sqrt{\frac{k + k_{ts}}{m}} \tag{3.5}$$

However, this cannot be the case due to the nature of interaction between particles

44

where k_{ts} varies with distance. A way to account for the changing k_{ts} is needed.

This is accomplished through application of Hamilton-Jacobi first order perturbation theory to the two spring model, a solution originally presented by Giessibl et al. [71]. The force between tip and sample is modeled as a perturbed Hamiltonian for the system. With $p = \frac{m^* dq'(t)}{dt}$, $q'(t) = -A\cos(2\pi f_0 t)$ which is the unperturbed motion of a cantilever, q the closest approach of the cantilever to the sample, m* the effective mass, and V_{ts} the perturbation.

$$H = \frac{p^2}{2m^*} + \frac{kq'(t)^2}{2} + V_{ts}(q) \tag{3.6}$$

Giessibl assumes a generic inverse power law interaction between tip and sample for the perturbation.

$$F_{ts}(q) = -Cq^{-n} \tag{3.7}$$

C is a force constant. This expression can be integrated to solve for V_{ts}.

$$V_{ts}(q) = \begin{cases} -\frac{C}{(n-1)q^{(n-1)}} & \text{for n} > 1 \\ -C\ln(q) & \text{for n=1} \end{cases} \tag{3.8}$$

Inserting this into the Hamiltonian, using $\Delta f = f - f_0$, and solving using the Hamiltonian formalism, frequency shift becomes:

$$\Delta f = -\frac{f_0}{kA^2} < F_{ts}q'(t) > \tag{3.9}$$

$< F_{ts}q'(t) >$ is the average over a full oscillation cycle. Therefore, equation 3.9 expressed as an integral over the full period can be written as:

$$\Delta f(z_b) = \frac{f_0^2}{kA} \int_0^{\frac{1}{f_0}} F_{ts}(z_b + A\cos(2\pi f_0 t))\cos(2\pi f_0 t)) \, dt \tag{3.10}$$

Where z_b is the position of the apex of the tip in relation to the midpoint of the cantilever oscillation, A is the amplitude, and t is time. For a more simplified form, $q'(t)$ is substituted back in and the amplitude is integrated to obtain:

$$\Delta f(z_b) = \frac{f_0}{2k} \frac{2}{\pi A^2} \int_{-A}^{A} \frac{F_{ts}(z_b - q')q'}{\sqrt{A^2 - q'^2}} \, \mathrm{d}q' \qquad (3.11)$$

This in turn can be integrated by parts resulting in:

$$\Delta f(z_{zb}) = \frac{f_0}{2k} \frac{2}{\pi A^2} \int_{-A}^{A} F_{ts}(z_{zb} + A - q') \frac{q'}{\sqrt{A^2 - q'^2}} \, \mathrm{d}q' \qquad (3.12)$$

F_{ts} and k_{ts} are related by equation 3.2 allowing an alternate expression as:

$$\Delta f(z_{zb}) = \frac{f_0}{2k} \frac{2}{\pi A^2} \int_{-A}^{A} k_{ts}(z_{zb} - q') \sqrt{A^2 - q'^2} \, \mathrm{d}q' \qquad (3.13)$$
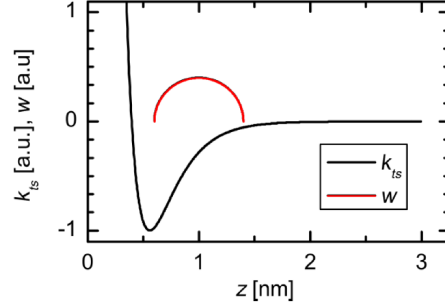
Figure 3.2: As k_{ts} is not a constant value, it can instead be accounted for by applying a semi-spherical weight function with a radius dependent on amplitude A [19].

Equation 3.12 is a more intuitive way of looking at the frequency shift and force relationship, and equation 3.13 shows how the force gradient k_{ts} is adjusted to make it "constant". Essentially, equation 3.13 is k_{ts} weighted with a semi-spherical amplitude dependent weight function with a radius A. A potential curve taken with a large amplitude will have k_{ts} averaged over a wider range as the limits of integration are increasing, registering as a larger radius in the function. This can be pictorially viewed in Fig. 3.2 [19].

Equation 3.12 can be used to evaluate the expected frequency shifts for a given

force law by substituting one in for F_{ts}. Examples of force laws would be the Morse Potential or Lennard-Jones Potential. Conversely, if given a set of Δf values, the equation can be inverted to solve for F_{ts} to obtain force values. Discussion of two widely used techniques for this inversion are discussed in section 3.5.

This perturbation approach is only valid if two circumstances are met. The first is that the perturbation is sufficiently small as required by a Hamiltonian perturbation so that motion of the cantilever remains approximately harmonic. With stored cantilever energy on the order of hundreds of eV assuming typical hundred picometer amplitudes and the perturbation on the order of eV, the perturbation does not introduce any anharmonicity into the system and inclusion of first order terms approximates data well [17] [72]. Large perturbations would cause significant deviations in data using the perturbation approach requiring the inclusion of higher order terms in the solution. The second assumption is that small amplitudes on the order of the smallest force interaction range for scanning are used. This is approximately around several hundred picometers. If amplitudes are many times greater than this range, a "correction factor" needs to be implemented.

Normalized Frequency Shift

When amplitudes are large compared to the range of tip-sample forces, the frequency shift decays with an additional amplitude dependence. Examining equation 3.13, it can be seen that as long as k_{ts} remains constant as the tip oscillates through its full sweep, Δf too remains constant. Once the amplitude reaches the decay length of tip-sample forces, Δf gains an additional amplitude dependence and changes as $\Delta f \propto A^{-1.5}$. Knowing this relationship, a "correction factor" for large amplitudes called the normalized frequency shift can be introduced [73]:

$$\gamma(z, A) = \frac{kA^{3/2}}{f_0}\Delta f(z, A) \tag{3.14}$$

If one allows the amplitude to theoretically approach infinity, the limit as $\lim_{A \to +\infty} \gamma(z, A) = \gamma_{lA}(z)$ which can be calculated using:

$$\gamma_{lA}(z) = \frac{1}{\sqrt{2\pi}} \int_0^{\inf} \frac{F_{ts}(z + z')}{\sqrt{z'}} dz' \tag{3.15}$$

This normalized shift helps by providing a common reference point. It is simply a measure of the intrinsic F_{ts} between tip and sample, independent of other variables like amplitude. Therefore, scans at different amplitudes can be referenced back to this common normalized curve to subtract amplitude dependent decay on Δf.

Holscher et al. did experiments using a silicon cantilever at a range of amplitudes from small to large, finding all of them matched precisely when scaled by the normalized frequency shift [74].

This scaling isn't necessary for experiments run in this work as all measurements were taken using small amplitude AFM; much less than the tip-sample interaction force range. However, the normalized frequency shift does have useful application in regard to amplitude calibration discussed in section 3.4.2.

3.1.1 Small Amplitude Scanning

Small amplitude scanning is desirable for UHV LT AFM experiments for reasons beyond making the modeling simpler. Its primary application in this work is that it allows the isolation of different kinds of surface forces on the H:Si(100) surface.

As discussed in section 1.1, forces of various sign and origin act on the AFM tip at any given position. These are a combination of short range forces like Pauli repulsion and long range ones like electrostatic and van der Waals. It is of interest to be able to probe only one type of these forces predominately at any given time, which is possible through small amplitude AFM and a modulation of tip-sample height.

To illustrate how this works, an example can be considered where both a fictional short range force with a magnitude of 1 nN and a range of 100 pm, and a long range force of magnitude 1 nN spread over 1000 pm are acting on an approached tip. If using an AFM tip with oscillation amplitude of 80 pm, the position of the tip in relation to the sample will determine what force dominates. If < 100 pm from the surface, the force gradient k_{ts} contribution from the short range force will be approximately an order of magnitude greater than what is contributed to k_{ts} by the

48

long range one. Conversely, the opposite is true if the AFM tip is positioned far from the surface where the short range force has decayed. This can be further illustrated through looking at an experimental curve.

Fig. 3.3 shows a measured Δf vs. z curve with theoretical model above. The amplitude used for the qPlus sensor for this Δf vs. z spectroscopic measurement was 80 pm. Attractive and repulsive regimes are labeled on the response curve in the model. Using an amplitude of 80 pm, the sensor could be placed in any force regime without large overlap into a different one. For example, if placed at z=-300 pm the tip is oscillating from z=-220 pm to z=-380 pm probing the weakly attractive forces. Similarly, the tip could be placed at other tip-sample distances to probe other regimes.

The experimental curve in Fig. 3.3 does have an unusual non-monotonic depression at -375 pm. This feature and its origin is discussed in more detail in section 4.3.

3.2 Electronics

Signals from oscillations as modified by surface interactions are very small, requiring careful design of the system electronics.

Signals from the qPlus sensor during scanning are first processed by an in-vacuum qPlus pre-amplifier mounted directly to the sample stage. This module is the first amplification stage for the deflection signal, taking the delicate piezoelectrically generated current from the sensor and amplifying it to be sent out of vacuum.

The internal pre-amplifier is fitted on the sample stage to reduce noise in the signal. The piezoelectric qPlus sensor generates charge during operation [75] which is sent to the internal pre-amplifier via a coaxial cable. The capacitance of the coaxial cable is dependent upon length, meaning that if too long most of the charge generated by the sensor in operation is being used to fill the cable capacitance instead of being brought to the pre-amplifier. Therefore, the pre-amplifier is placed close to the scanning stage so that small signals are not sent over long high-capacitance cables. Once processed into a more robust signal at the pre-amplifier, it is sent to
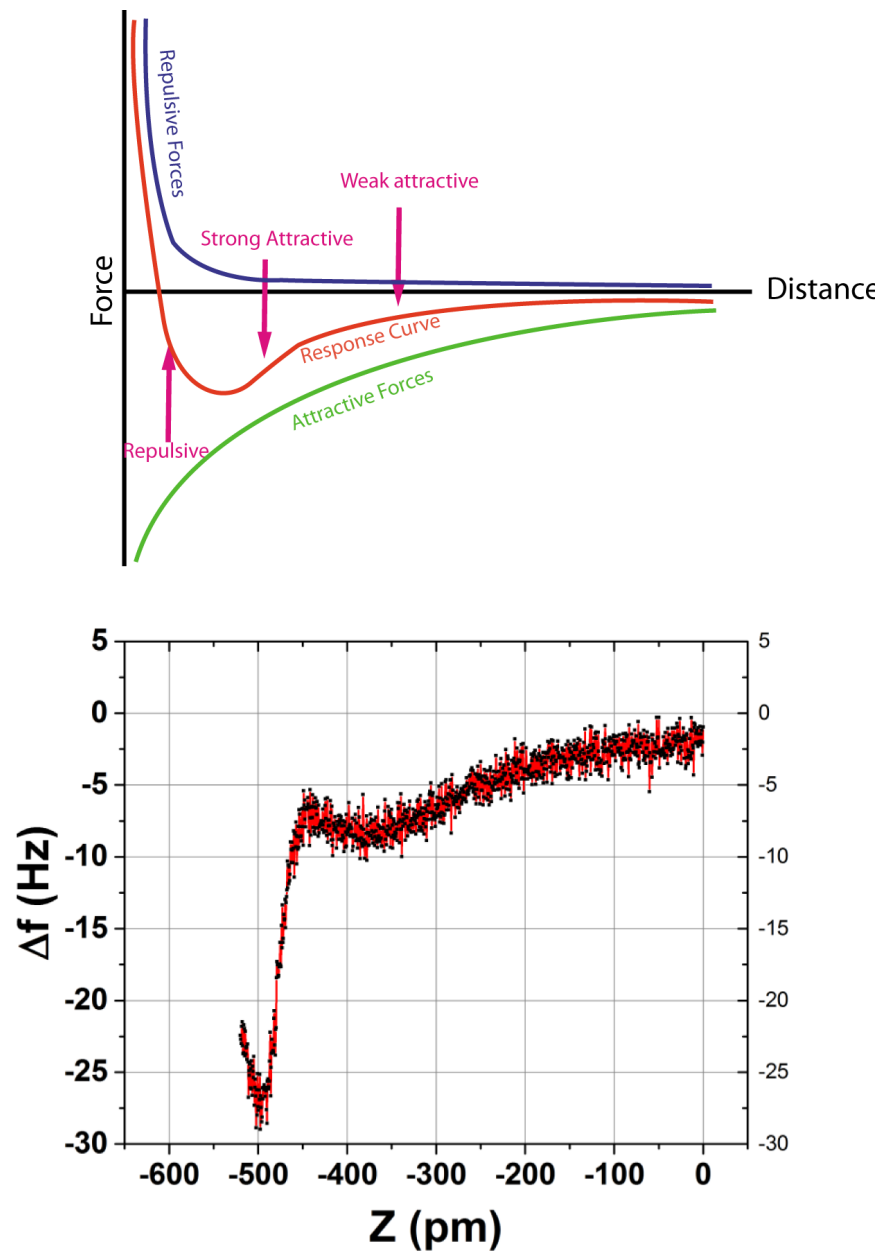
Figure 3.3: Model representation of a typical tip-sample Δf vs. z curve (Top). This is juxtaposed with an unprocessed Δf vs. z curve taken over H:Si(100) using a qPlus sensor V=0, A=80 pm. Z(pm) is in reference to the chosen starting point of the scan where a small Δf began to be observed, and moving left reduces sensor and sample distance (Bottom).

a secondary out-of-vacuum pre-amplifier where signals are directed to the control software.

The control software used for all experiments was the Nanonis SPM package. This package has full utility for both STM and AFM control. It is fully digital, with all analog signals being converted into digital ones for easy processing and use. Parameters and operations are easily set using the Nanonis graphical interface.

AFM is specifically controlled by the Oscillation Controller (OC4) which has a digitally integrated phase lock loop for AFM. Imaging modes include options for constant height and constant frequency shift AFM. The electronics themselves add negligible noise, with the primary noise contribution to AFM scans being thermal and detector noise from the qPlus discussed in section 3.3.1.

Before any scanning begins in AFM, settings for the many feedback loops governing non-contact AFM must be calibrated.

3.3   qPlus Calibration

Stable scanning with qPlus using the Nanonis software package requires careful settings for many scanning parameters. As mentioned in section 1.1 surface forces are non-monotonic in nature. This posed many problems for early AFM development, and even now with the advent of dynamic AFM requires careful feedback regulation with strictly set parameters.

Feedback regulation for non-contact scanning is accomplished through the use of either 2 or 3 feedback loops running simultaneously, depending on the type of AFM scanning desired. As explained in section 1.1.2, there are two methods of AFM: constant frequency shift and constant height.

Height maps are generated when scanning in constant frequency shift mode. The three feedback loops being regulated by Proportional/Integral gain (PI) controllers to obtain such images are for amplitude, phase, and frequency shift. A Proportional/Integral/Derivative (PID) controller could be used for feedback regulation instead, but the derivative action on such a controller can be sensitive to measurement noise. Therefore, the default Nanonis control package PI controllers were used.

If in constant height mode, Δf maps are generated. Amplitude and phase are kept constant by PI controllers, and z height is set to a fixed value with drift negated by anti-drift compensation explained in section 4.2. In either scanning mode case, each PI loop requires precisely set values for atomic resolution.

Two of the oscillation controllers for AFM are shown in Fig. 3.4, and a third acts to regulate Δf when in constant height mode. Orchestrating all three PI controllers to work together can be complicated. Amplitude and phase settings have four free feedback parameters, and Δf has two.

Fig. 3.5 shows the basic principal of the 3 feedback loop AFM scheme for constant frequency shift scanning. Amplitude, phase, and Δf are given constant set-points regulated with their own PI controllers. Amplitude regulation ensures a larger oscillation drive signal is delivered if any damping occurs. The piezoelectrically generated signal from the qPlus sensor after preamplification is compared to the Δf setpoint defined by the user. If it deviates, the z-height is adjusted by the z-regulator to re-match the two values. The z signal is plotted as a topographic map.

Due to the difficulty in setting all the free parameters, the Nanonis package includes a program that sets the proportional and integral settings for the PI controllers based upon the sensitivity of the qPlus though an automated program called "Perfect Phase Lock Loop" (Perfect PLL). The PLL itself is capable of supporting extremely small amplitudes at a detection bandwidth of 4 KHz to 3 MHz. It also supports a flexible demodulation bandwidth for both phase and amplitude, allowing the adjustment of output signal frequency noise. The demodulation bandwidth was set to 10 Hz for all experiments.

The first step in using Perfect PLL is to record a precise resonance curve for the sensor as shown in Fig. 3.6. This is accomplished by sweeping a sinusoidal drive signal through a range of frequencies known to include the sensor resonance. The drive signal causes a piezoelectric element beneath the tuning fork sensor to oscillate. Electrodes on the quartz sensor allow a piezoelectric voltage, and hence the frequency, phase and amplitude of oscillation to be detected.

A highly responsive qPlus sensor has a large quality factor with a highly sloped phase which, as discussed later in section 3.3.1, relates to the minimum detectable
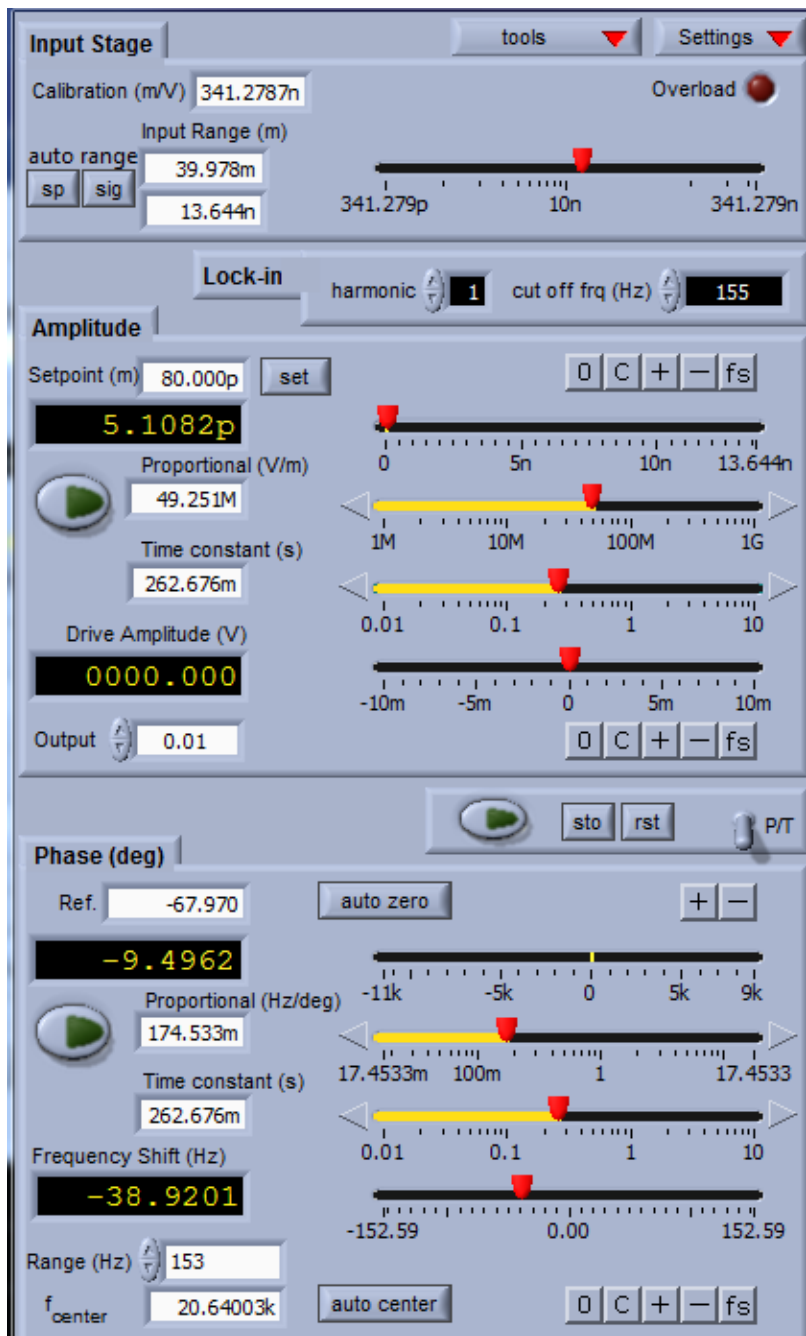
Figure 3.4: Oscillation controllers for the amplitude and phase feedback loops. Each loop has 4 individual settings crucial to proper operation of the AFM tuning fork that must be carefully set.
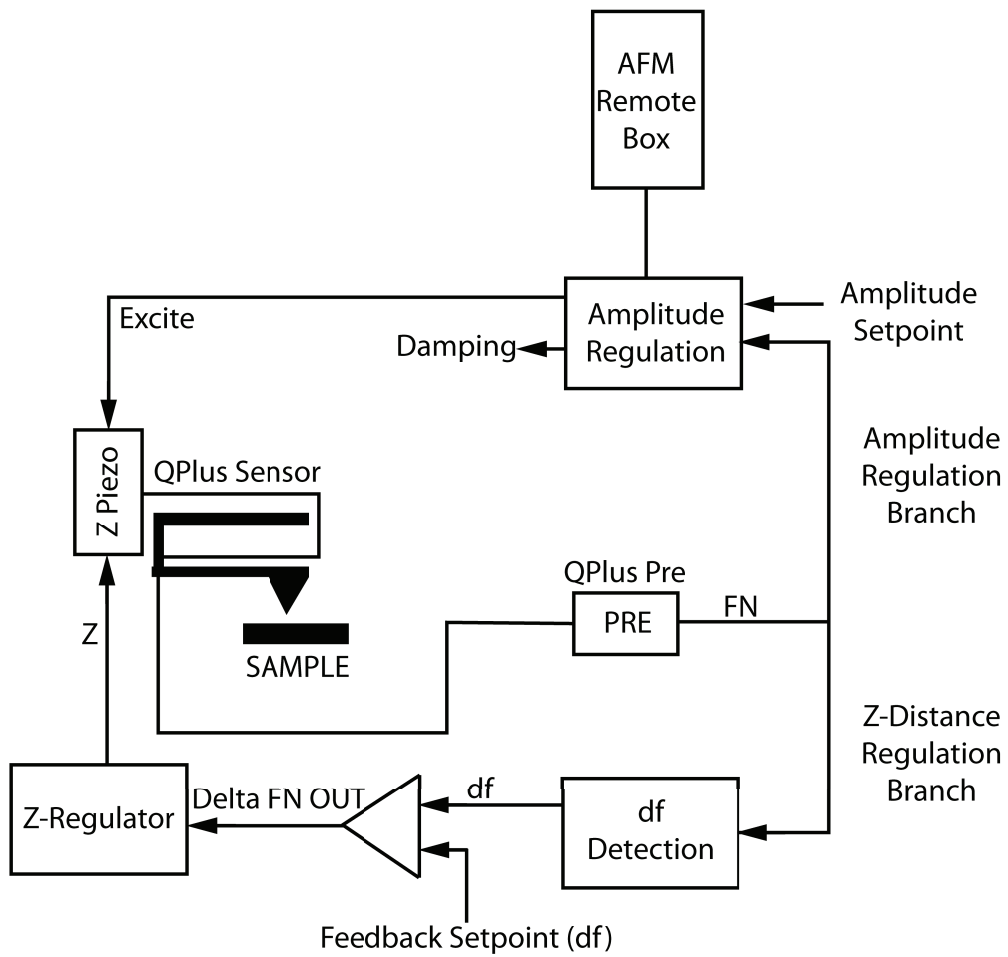
Figure 3.5: Schematic of the PI controller set up for constant Δf scanning reproduced from [20]
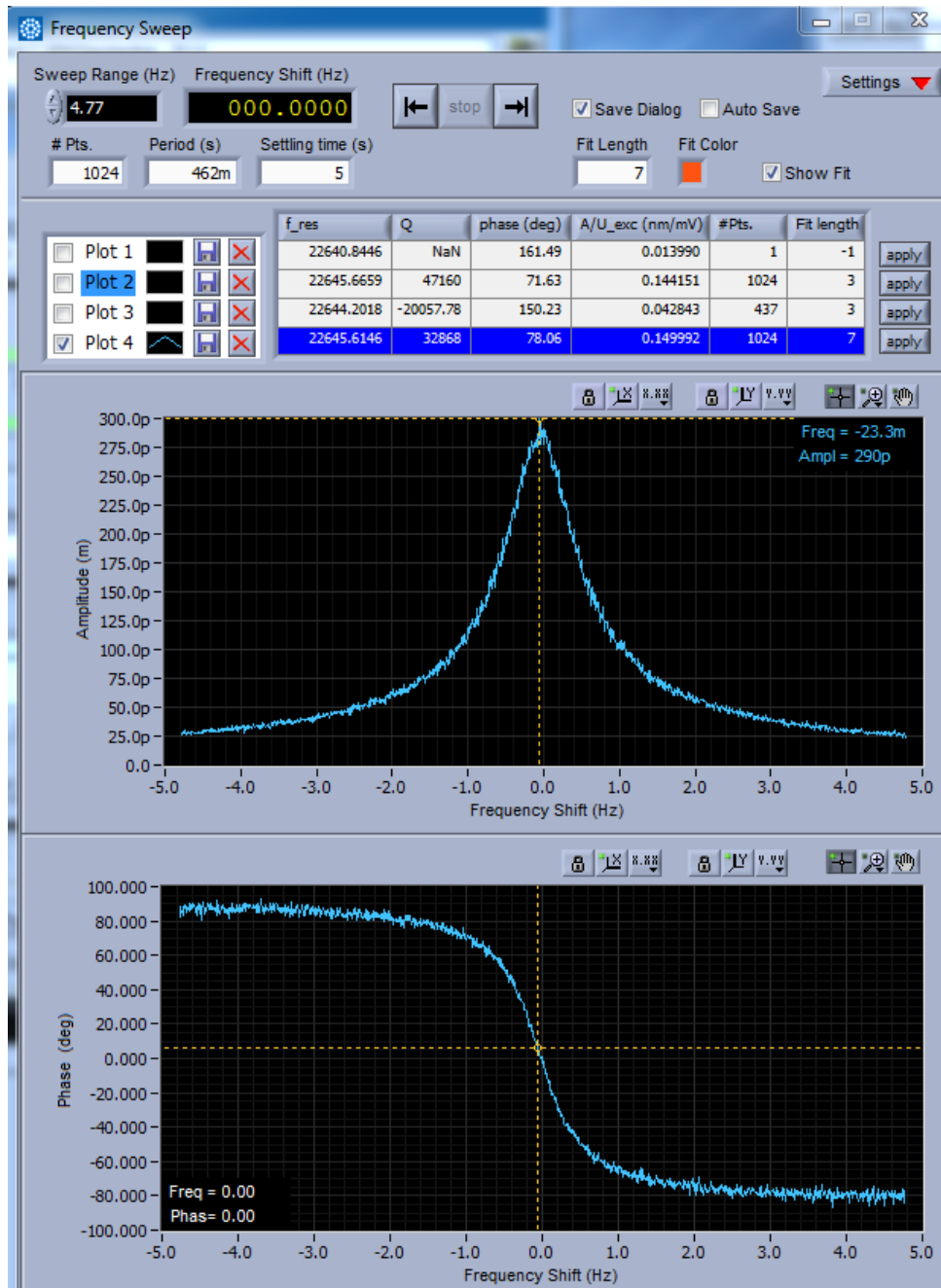
Figure 3.6: A taken frequency sweep for an average qPlus sensor. Excitation voltage=0.8 mV, f_0=22645 Hz, Points taken=1024, Settling period per point=462 ms, Q=32868.

frequency shift. A sensor that is very sensitive to tip-surface interactions requires different time constant parameters for its PI controllers than a sensor that is less responsive.

Examining the top and bottom figures in the resonance curve taken in Fig. 3.5, it is evident that small frequency shifts for a sensor with exceptional Q will change the phase substantially since it is highly sloped. This is desirable as it provides a higher signal to noise ratio and is detected more easily by the Phase Lock Loop. However, this large change necessitates the need for a large correction factor from the PI controllers as large deviations from their respective amplitude and phase set-points are occurring. Both the proportional and integral constants for the PI controllers will be set to higher values to correct faster for the exceptional response of the tuning fork.

With the demodulation bandwidths selected and resonance curves run, all the feedback loops are set with optimal values using the automated Perfect PLL program. As mentioned earlier, negligible noise is introduced by the software electronics. Most noise on the sensor can be attributed to two factors.

3.3.1 Noise Considerations

Noise in the qPlus frequency measurement can be attributed to two main factors: thermal noise and detection noise.

$$\delta f = \sqrt{\delta f_{thermal}^2 + \delta f_{detector}^2} \tag{3.16}$$

Thermal noise of a cantilever was formalized by Albrecht et al. in 1991 [26] using the thermal energy of a cantilever ($k_b T$) combined with the total mechanical energy stored in it ($\frac{1}{2}kA^2$), divided by its quality factor and the detection bandwidth. This generates the following ratio:

$$\delta f_{thermal} = f_0 \sqrt{\frac{k_B T B}{\pi k A^2 f_0 Q}} \tag{3.17}$$

The noise is inversely proportional to the resonance frequency, quality factor,

and amplitude of the oscillator, and proportional to the temperature and bandwidth. qPlus's quality factors on the order of 10^4 and resonances in the 25,000 Hz range make it well suited to providing a low noise threshold. Combined with the $\approx$ 4.5 K operating temperature and 10 Hz bandwidth, thermal noise averages around 0.004 Hz assuming general parameters of A= 80 pm, Q= 30,000, B= 10 Hz, and resonance= 25,000 Hz. Large amplitudes would also decrease frequency noise, but are not advantageous in other respects as described in section 3.1.1.

Detection noise is calculated through the following relationship derived by Dürig et al. [31, 76]:

$$\delta f_{detector} = \frac{n_{q'}}{\pi A} B_{FM}^{3/2} \qquad (3.18)$$

Where $n_{q'}$ is the deflection noise density quoted to be 100 fm/$\sqrt{Hz}$ as by manufacturer [20, 75], and B_{FM} is the bandwidth. Using the same values for parameters as for the thermal noise, an approximate $\delta f_{detector}$= 0.01 Hz.

Using equation 3.16, cantilever detection noise is $\approx$ 0.01 Hz. This value is not representative of overall system noise as other factors like floor noise contribute as well. However, this does provide a minimum detectable force gradient value, and was instructive on optomizing parameters through adjustments such as lowering the bandwidth B_{FM}. With detection noise optimized, and an understanding of force theory for AFM, the tip is ready to be approached.

3.4 Approach and Scanning

The tip was always approached in STM scanning mode. This is a practical matter as feedback settings are faster, speeding up the approach. Before starting the approach, a bias is applied so tunneling current can flow between tip and sample.

Coarse motors are used to bring the tip to within $\approx$ 3 mm of the sample in the scanning chamber, after which an automated fine motion piezoelectric motor routine takes over to approach the tip the last bit through the z-piezoelectric stage. The tip approaches until it sees the set-point for tunneling current is reached which is usually

around 30 pA at a tip-sample bias of -2 V. An approach could also be done on an insulating sample or with zero bias in constant frequency shift AFM mode where it would approach until a constant Δf set-point was detected. This was tested but not used as it takes longer than a STM approach.

Once approached in STM mode, the tip is raster scanned over the surface to check for sharpness of the tip. Even with single atom etching, the tip can sometimes be "double" or "multi" where ghost images of surface features will appear from unwanted extra protrusions. If this is the case, the tip must be sharpened to a single atom using in-situ methods.

3.4.1 In-Situ Tip Sharpening

A perfect tip is critical to good AFM data. Additional apex atoms will result in 2D images having double or multi features not representative of the actual sample surface, and force vs. distance curves having phantom features and blunted profiles [77]. There are two methods of sharpening a tip in-situ, with the first method being controlled "crashes" into the surface.

A small patch of H:Si(100) will be selected with an area of $\approx$ 5×5 nm. The tunneling current will be raised to I=200 pA, and the bias between tip and sample to 4.0 V; values sufficiently energetic enough to break H-Si bonds. Raster scanning the 5×5 nm area at a moderate speed under these parameters desorbs any H atoms from the silicon, resulting in an area of bare silicon. Fig. 3.7 shows a desorbed area.

The tip is gently crashed into this patch between 300-1000 pm and then tested by again acquiring an image in a fresh area. The process is repeated until individual atoms and features are resolved with no artifacts due to a multi-atom apex.

While seeming counter-intuitive as crashes are usually associated with flattening and ruining a tip, this technique does the opposite. When crashed, atoms from the surface stick to the tip often creating a sharper apex [78] [79]. Controlled crashing is a technique commonly used by prominent AFM groups such as the IBM Zurich researchers [80] [81].

The second technique for tip sharpening is voltage pulses on the tip. The tip
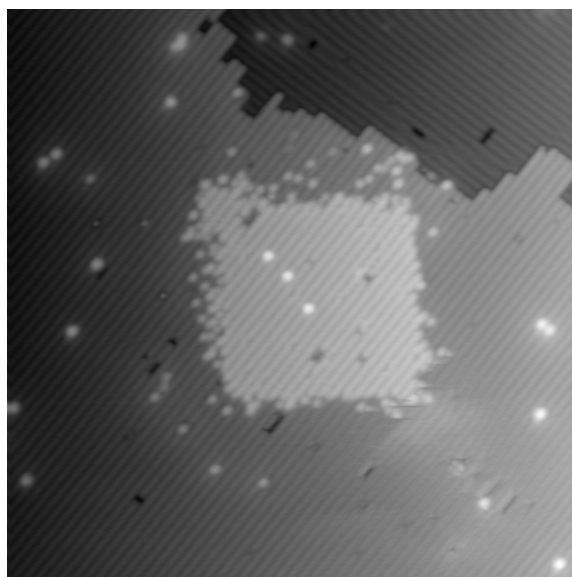
Figure 3.7: STM image (V= -1.8, I=30 pA, Area= 40×40 nm) showing a bare silicon square created after tip induced desorption of hydrogen atoms.

will have a pulse between ± 3-8 V applied to it for 100 ms. This changes the apex structure through ejection of atoms on the tip. This technique was used sparingly, as the nature of the tip change is hard to predict unlike controlled crashes.

When a single atom tip is achieved, the sensor can be switched to AFM mode and the amplitude calibrated.

3.4.2   Switching to AFM Mode and Amplitude Calibration

Amplitude calibration is done on every qPlus sensor as the voltage needed to excite each one to the same amplitude will vary due to the uniqueness of each sensor. Calibration is important as it factors in to the quantitative measurements of force discussed in section 3.5.

Amplitude is calibrated in AFM scanning mode, requiring a switch out of STM mode. To switch to AFM mode, the tip is retracted from the surface by 2 nm, bias settings are chosen, and tip oscillation at the desired amplitude is started.

Oscillations are controlled by the "Oscillation Controller" menu which has the PI

feedback loops for amplitude and phase as shown in Fig. 3.4. Both of these feedback loops are switched on with their optimized settings from running Perfect PLL.

Amplitude calibration is done in constant frequency shift AFM mode, therefore the Δf PI is also switched on. A moderate set-point for Δf is selected in the range of several Hz, and the tip is allowed to approach until this deflection setpoint is observed.

Once there, the Nanonis package also has a program that runs a calibration procedure several times and averages the results. This calibration method is based on work by Guggisberg [82]. A screen of the software is shown in Fig. 3.8. The general theory for how the calibration is done is as follows.

Amplitude Calibration Theory

The calibration procedure is based on knowledge of the normalized frequency shift from section 3.1. Going back to equation 3.14 from that section, it can be rearranged as:

$$\Delta f = \frac{f_0 \gamma(z, A)}{A^{3/2} k} \tag{3.19}$$

Substituting the infinite amplitude integral in equation 3.15 for $\gamma(z, A)$, the expression becomes:

$$\Delta f = \frac{f_0}{\sqrt{2\pi} A^{3/2} k} \int_z^\infty \frac{F(x)}{\sqrt{x-z}} dx \tag{3.20}$$

$\gamma(z, A)$ for infinite amplitude describes the shape of the force vs. distance curve independent of the fixed parameters like amplitude A, spring constant k, or resonance f_0. It will always be the same for a given tip and sample with the pre-factor constants scaling it. Therefore, starting with two amplitudes and frequency shifts:

$$\Delta f_1 = \frac{f_0}{\sqrt{2} A_1^{3/2} \gamma(z)} \tag{3.21}$$

And

$$\Delta f_2 = \frac{f_0}{\sqrt{2}A_2^{3/2}\gamma(z)} \tag{3.22}$$

Eq. 3.22 can be solved for $\gamma(z)$ and substituted into Eq. 3.21 to relate two frequency shifts at different amplitudes:

$$\Delta f_2 = \Delta f_1 [\frac{A_1}{A_2}]^{-3/2} \tag{3.23}$$

This gives an easily exploitable relationship for calibration. To illustrate, a calibration can be started with an amplitude of A_1=150 pm, Δf_1=-30 Hz, excitation V=10 mV, and z-piezo relative position= -160.000 nm. The excitation V is the amount of voltage necessary to drive the cantilever consistently at the desired amplitude and given position.

Then, the amplitude is increased to $A_2$200 pm which requires a larger excitation V=20 mV. Z is not changed at this point. From the relation in Eq. 3.23, Δf_2 is now ≈ -46.18 Hz.

To go to a point of "equal interaction", or a point where the cantilever is seeing the same frequency shift using the increased amplitude, it requires that z must now be changed to reduce Δf_2, so it matches the original $\Delta f_1 = -30$ Hz. For this illustration, suppose this new z-relative position is = -159.000 nm.

Therefore, for a ΔV of 10 mV, z is changed by 1 nm to maintain an equivalent frequency shift for the two differing amplitudes, giving a calibration value of 100 nm/V. Or, a 1 V excitation on the z-piezo inducing oscillations on tip will produce a 100 nm amplitude change. The calibration function of the Nanonis software does this procedure several times and averages the results as shown in Fig. 3.8.

3.5   Force Spectroscopy

As shown in images such as Fig. 3.1 and Fig. 3.3, Δf vs. distance curves are a commonly used experimental AFM technique to gain information about surface forces. However, Δf vs. distance curves must be converted from Δf to quantitative
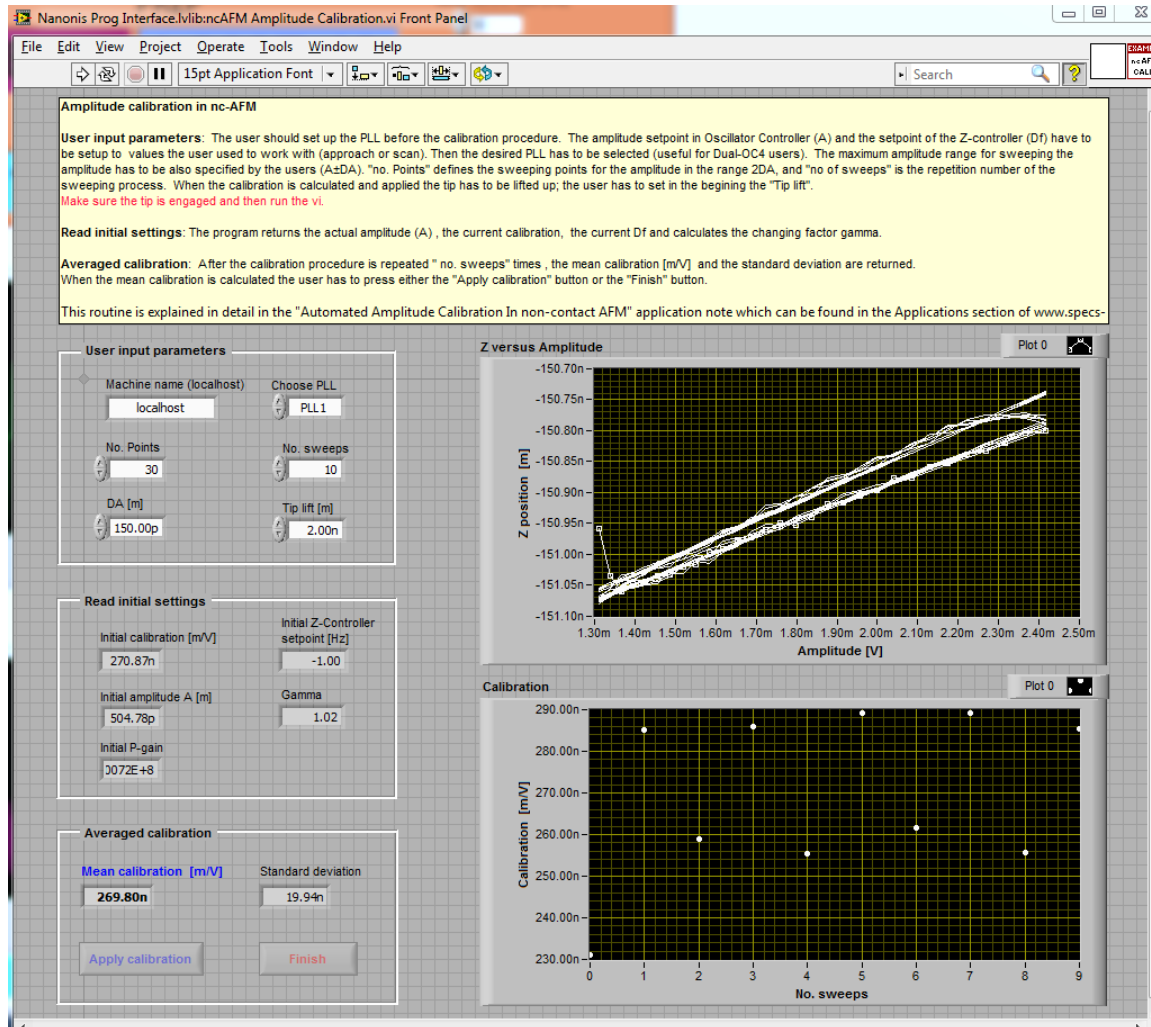
Figure 3.8: Amplitude calibration of a qPlus tuning fork using the automated Nanonis calibration software. 10 runs were taken by sweeping 150 pm above and below the initial amplitude set-point. Calibration results are plotted in nm/V and an averaged value for the 10 runs is calculated and given as 269.80 nm/V.

force values. This is done using theory explained in section 3.1.

Equation 3.12 established the relationship between Δf and force. This equation can be inverted to get force from frequency shift, but this inversion is not entirely straightforward. There are two accepted ways to solve this equation for a given set of discrete Δf values; the Giessibl Matrix Method [71], and the Sader-Jarvis method [83].

3.5.1   Giessibl Matrix Method

Data taken from Δf vs. distance curves is discrete in nature. This required an adaptation to equation 3.12, which can instead be expressed as a sum with equidistant Δf values and an appropriate weight function applied to each. Expressing equation 3.12 as a sum results in:

$$\Delta f_i = \sum_{j=1}^{N} W_{ij} F_{ts,j} \tag{3.24}$$

Where W_{ij} is the amplitude dependent weight function in matrix form defined as:

$$W_{ij} = \begin{cases} \frac{f_0}{2k} \frac{2}{\pi A} \int_l^u \frac{\tau}{\sqrt{1-\tau^2}} \mathrm{d}\tau & \text{if } 0 \le i - j \le= 2\alpha \\ 0 & \text{else,} \end{cases} \tag{3.25}$$

α is the ratio of the amplitude A and the step width d, $\frac{A}{d}$, rounded to the nearest integer value. Upper and lower integration boundaries are defined as:

$$u = \frac{1 - 2(i - j)}{2\alpha + 1} \tag{3.26}$$

$$l = \frac{1 - 2(i - j + 1)}{2\alpha + 1} \tag{3.27}$$

Once the elements of W_{ij} are defined, equation 3.24 can be solved for F_{ts} by multiplying both sides by the inverse of matrix W_{ij} referred to as M_{ij}:

$$\Delta F_{ts,j} = \sum_{i=1}^{N} M_{ji}\Delta f_i \tag{3.28}$$

Calculation of the inverse matrix M_{ji} can be done using software. A python script was written to achieve this conversion, but was abandoned in favor of the more effective Δf conversion method called the Sader-Jarvis method.

3.5.2 Sader-Jarvis Method

Sader and Jarvis proposed an alternate method of Δf conversion in 2004 [83], nearly 3 years after Giessibl proposed his original matrix method.

With the Sader Jarvis method, the tip sample force from equation 3.11 F_{ts} is first expressed as a Laplace transformation:

$$F_{ts}(z_{ltp}) = \int_0^\infty A(\lambda)T(\lambda a)exp(-\lambda z_{ltp})\mathrm{d}\lambda \tag{3.29}$$

Where $A(\lambda)$ is the inverse Laplace transformation of F_{ts} and z_{ltp} is the tip-sample distance. This equation is substituted back into 3.12 and solved to obtain:

$$F_{ts}(z_{ltp}) = \frac{2k}{f_0}\int_{z_{ltp}}^\infty \left[\left(1 + \frac{\sqrt{A}}{8\sqrt{\pi(t-z_{ltp})}}\right)\Delta f(t) - \frac{A^{3/2}}{\sqrt{2(t-z_{ltp})}}\frac{\mathrm{d}\Delta f(t)}{\mathrm{d}t}\right]\mathrm{d}t \tag{3.30}$$

Derivation of this expression is done by replacing it with the difference quotient, an expression to calculate the slope for two points, and integration is done using the trapezoidal rule, a technique to approximate integration:

$$F_j = \frac{2k}{f_0}\left[C_j + \sum_{i=j+1}^{N-2}(z_{i+1} - z_i)\frac{g_{i+1} + g_i}{2}\right] \tag{3.31}$$

With C_j being the correction term for the divergence of 3.30 at t=z_{ltp}:

$$C_j = \Delta f_j(z_{j+1} - z_j) + 2\frac{\sqrt{A}}{8\sqrt{\pi}}\Delta f_j\sqrt{z_{j+1} - z_j} - 2\frac{A^{3/2}}{\sqrt{2}}\frac{\Delta f_{j+1} - \Delta f_j}{z_{j+1} - z_j}\sqrt{z_{j+1} - z_j} \quad (3.32)$$

And the numerical integration is conducted over the discretized integrand:

$$g_k = \left(1 + \frac{\sqrt{A}}{8\sqrt{\pi(z_k - z_j)}}\right)\Delta f_k - \frac{A^{3/2}}{\sqrt{2(z_k - z_j)}}\frac{\Delta f_{k+1} - \Delta f_k}{z_{k+1} - z_k} \quad (3.33)$$

Using this method to evaluate equation 3.31, accurate force spectroscopy on a surface of interest can be obtained. Python code written for the Sader-Jarvis inversion used to evaluate all force spectroscopy curves in this thesis is included in the appendix 5.1. This code allows the quantitative site specific grid force spectroscopy probing of different surface sites on H:Si(100) as presented in section 4.3.

Chapter 4

NC-AFM Study of H:Si(100)

H:Si(100) 2×1 is examined due to its attractive potential for nano-electronic applications. Si(100) is currently the surface on which all integrated circuits are built, and has already been extensively investigated as a surface of interest for computing applications through exploitation of DBs as QCA cells [1] [2] [3], wires [4] [5], and logic gates [6]. H:Si(100) also provides a promising surface for examining adsorbed atoms, physisorbed molecules [7] [8] [9], and chemisorbed molecular structures with potential molecular electronics applications [10].

Despite its many applications, only a few studies of H:Si(100) surface have been undertaken with AFM [11] [84], and never at low temperature, in constant height mode, or with the advantages of a qPlus sensor.

As AFM gives access to many additional kinds of information on the surface not obtained through other means such as chemical forces [85] [86], charge distributions [9, 62], and chemical bonds [56], as well as allows zero bias non-perturbative measurements, a study of the H:Si(100) surface with low temperature NC-AFM was undertaken.

4.1 Constant Frequency Shift AFM

As detailed in section 1.1.2 there are two different scanning modes of AFM possible: constant frequency shift and constant height.

The first scanning mode explored in our AFM was constant frequency shift imaging. This mode attempts to plotting z-topography while maintaining a constant amplitude, phase, and Δf deflection on the cantilever. Initial scan settings were chosen using recommended parameters in the literature and from the Omicron user manual [20]. The first atom resolved AFM image obtained of the hydrogen terminated silicon (100) (H:Si(100)) surface with the 2×1 reconstruction in our system is shown in Fig. 4.1.
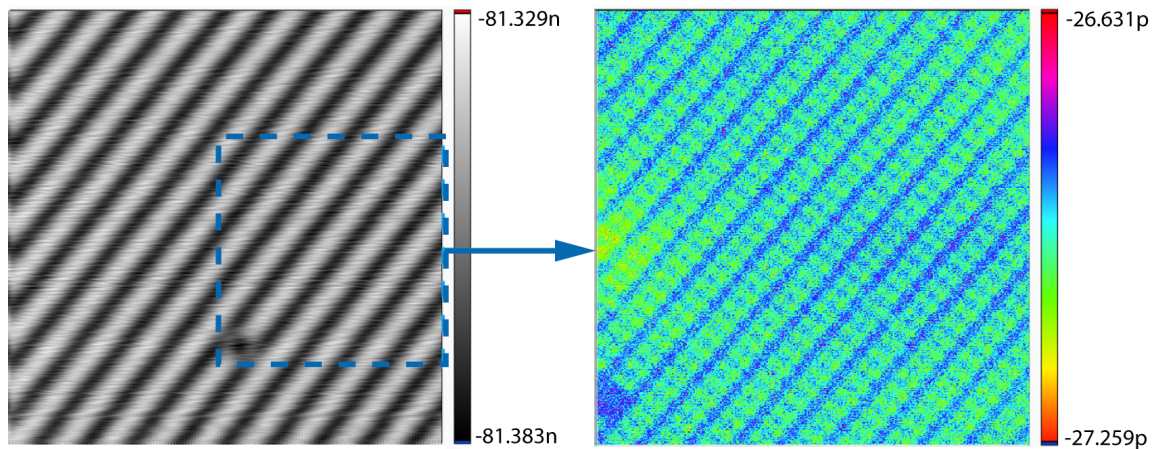
Figure 4.1: (a) STM scan of H:Si(100) V=-2V I=30pA. (b) First constant frequency shift NC-AFM image obtained with A=350pm, Δf= -2.0, Area=10x10nm, V=-0.2V.

Atomic resolution only lasted for a few scans and was un-recoverable after a tip crash. The image was acquired without using optimized PI feedback loop settings or amplitude calibration. Re-acquiring atomic resolution, even after re-sharpening the tip, proved difficult. Therefore, we opted to switch to the Si(111) 7×7 surface which displays larger, easier to visualize corrugations, to refine our AFM techniques.

Si(111) 7×7 is a well documented surface for NC-AFM [13, 87] [88]. Using these published works, optimal settings were obtained before switching back to the

relatively inert and more difficult to image H:Si(100). During this time, settings for the feedback loops were optimized by taking precise resonance curves and use of the PerfectPLL module explained in section 3.3. Calibration for correct amplitudes was also implemented from section 3.4.2, enabling better tunings to be found by PerfectPLL. These adaptions dramatically increased the stability and likelihood of achieving atomic resolution on the surface, giving detailed images of the Si(111) 7×7 structure as seen in Fig. 4.2. At this time, we switched back to H:Si(100) with the improved AFM techniques.
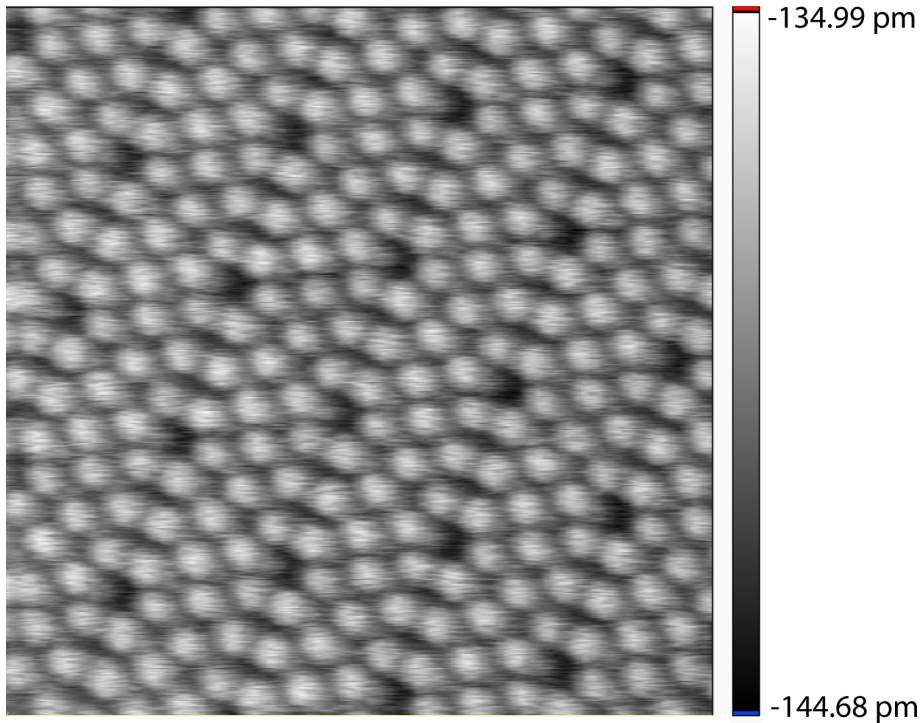
Figure 4.2: Optimized constant Δf image of Si(111) 7×7 with A=500 pm, Δf=-12.0 Hz, Area=10 $\times$ 10 nm, V=0, Scan Speed= 800 ms/per-line.

Atomic resolution was routinely obtained on H:Si(100) using the new optimized parameters. Fig. 4.3 shows a constant Δf image of a defect free portion of H:Si(100). This image shows good resolution when compared to the only other published AFM image also recorded in constant Δf taken by Yokoyama [11]. However, defects or

features proved difficult to image.
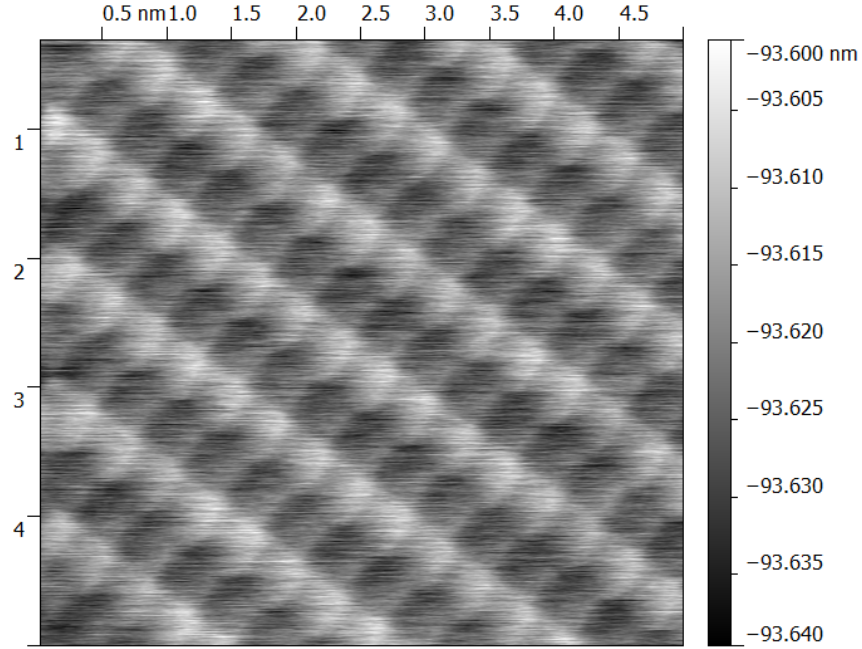
Figure 4.3: Constant Δf image of H:Si(100) 2×1 with A=800 pm, Δf=-2.5 Hz, Area=5 × 5 nm area, and V=0.

H:Si(100) would cause frequency shifts on the order of -2 to -15 Hz with a noise level of ≈ 0.7 Hz. However, a dangling bond or other surface feature could prompt shifts on the order of -90 Hz. This dramatic change from a few Hz to -90 Hz could not be compensated for fast enough with the feedback loops when scanning at even a moderate speed. A sudden Δf change would cause an overcompensation from the feedback loops, causing a tip crash which prevents further atomic resolution imaging. This could be partially improved by slower scan speeds at smaller amplitudes, but was ultimately found to be ineffective. Instead, constant height AFM was used as it was found to be a more robust technique.

4.2 Constant Height AFM

Constant height imaging involves setting a fixed height for the sensor above the sample, and raster scanning through a plane parallel to the surface while recording Δf change. Constant height offers the advantages over constant frequency shift of being robust and able to probe different force regimes on the surface by modulating z-height. This method only uses two feedback loops compared to constant Δf's three. Amplitude and phase shift are keep constant through PI loops, but z is assumed to remain constant once set in a plane. The liquid helium temperature of our machine means there is very little thermal drift, so once the sensor is set in a z plane it changes very minimally (≈ 10 fm/s). Early constant height experiments relied on this stability, but for later data z-drift compensation was used as an additional correction.

Z-drift compensation is determined in STM mode with an applied bias between tip and sample. The STM feedback loop that maintains a constant current is activated, and the z position of the sensor in time is tracked. Any adjustments the feedback loop makes to maintain the constant current is a compensation for z drift. A trend can be extracted from this data and compensated for in the software before switching to AFM mode. A typical z-drift value would be ≈ 10 fm/s. X and Y drift correction was also used, and is performed by an automated atom tracking program built into the Nanonis software. Alternatively, 2 constant current STM images taken at different times can be compared, and the difference in the relative position (X and Y coordinates) of a specific feature on the image between the two gives an indication of the drift. These drift corrections were not used for all constant height measurements. Images where these compensations were not used are marked in the captions.

Piezoelectric "creep" is a secondary issue and is minimized by letting the tip stabilize in the desired scanning location for a period of time. Small changes in polarization on the piezoelectric ceramics with changes in applied field during tip movement cause creep. The changing polarization causes the probe to keep moving a minute amount over time, or "creep" position. This activated process is almost,

but not entirely, eliminated at 4 K, and what little there is can be remedied by letting the probe sit before scanning as creep decreases logarithmically with time [20]. Once stabilized, the target area is scanned with special care being taken to only move the probe small distances at a time to not re-introduce creep. The slow scan speeds for AFM images also serve to reduce creep.
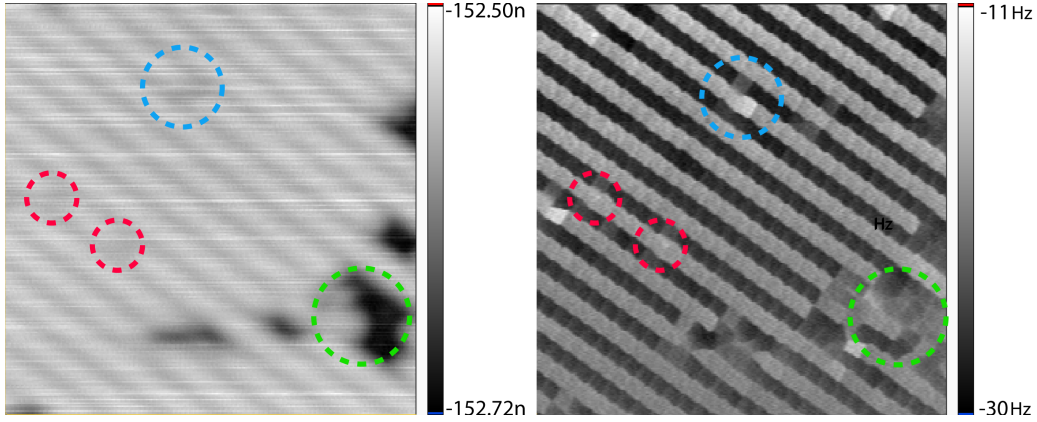
Figure 4.4: Z-topography STM of H:Si(100) V=-2.0, I=30 pA, Area=10×10 nm (left) and corresponding constant height AFM V=600 mV, Amp=600 pm, Area=10 × 10 nm (right). Constant height topography tracks the Hz frequency deflection. Defects are highlighted in the color matched circles. No drift compensation was used.

Fig. 4.4 (left) shows a STM image acquired before switching to AFM mode to image the same area (right). The STM tip is clearly not a perfect single atom tip, showing rows but not individual dimers in those rows. However, the AFM image shows atomic resolution with surface defects which have been highlighted in both figures. Evidently, the different mechanisms underlying STM and AFM can cause very different images with the same tip.

Further experimentation proved constant height AFM to be a very robust technique, allowing the imaging of all defects and features. With reliable AFM in hand our goal shifted to acquiring images of H:Si(100) with near perfect settings and tip.

Fig. 4.5 (top) shows an STM image of H:Si(100) with excellent resolution indicating a near perfect tip. The tip was switched to AFM mode and z-spectroscopy, also known as Δf vs. z or force vs. z curves, were taken by approaching the oscillating

tip to sample and measuring Δf response. This was done at the red dot marked in the STM image, and the result is shown directly below with frequency shift in units of Hertz. A SavitzkyGolay smoothing filter, which works by fitting successive data points with a low-degree polynomial using linear least squares, was applied to the z-spectroscopy data to increase the signal to noise ratio before plotting. For comparison, Fig. 3.3 from section 3.1.1 showed a z-spectroscopy curve without filter. The smoothed data was then deconvoluted using the Sader-Jarvis method from section 3.5.2 with code given in appendix 5.1. Force is given in units of nN and plotted at the bottom.

The z-spectroscopy is taken above a hydrogen atom in a dimer. The interaction potential in Fig. 4.5 doesn't look quite like a classical response curve, with a second minima occurring at -325 pm, the origin of which is discussed in section 4.3. The peak attractive interaction causes a maximum frequency deflection of -15 Hz off sensor resonance at -470 pm, correlating to a maximum attractive force of -0.64 nN between surface and tip after force conversion.

These Δf vs. z curves are valuable before starting any NC-AFM for two reasons: to study how close to the surface scans can be performed before reaching a tip damaging interaction range, and to reveal what z height corresponds to what regime of interaction force. Referring back to the model response curve in Fig. 3.3 (top), the tip through modulation of z can be correlated with the "weakly" attractive, "strongly" attractive, or repulsive regimes. Each regime has a distinct mixture of surface forces with different strengths. Z-spectroscopy associates a numerical z value with a given regime, helping with extraction of force information. This has application in the next analytic NC-AFM technique applied on H:Si(100), which is height differing images on H:Si(100).

Gross et al. pioneered the idea of forces on a molecule or adatom being extracted through multiple constant height images taken at regular intervals approaching the surface. In 2009 Gross et al. charged Au atoms with voltage pulses. Constant height AFM images showed a difference in interaction force of a few pN, that was correlated with the difference in charge state of the Au atoms [14]. Also in 2009, he extracted the type and strength of forces from a pentacene molecule using constant
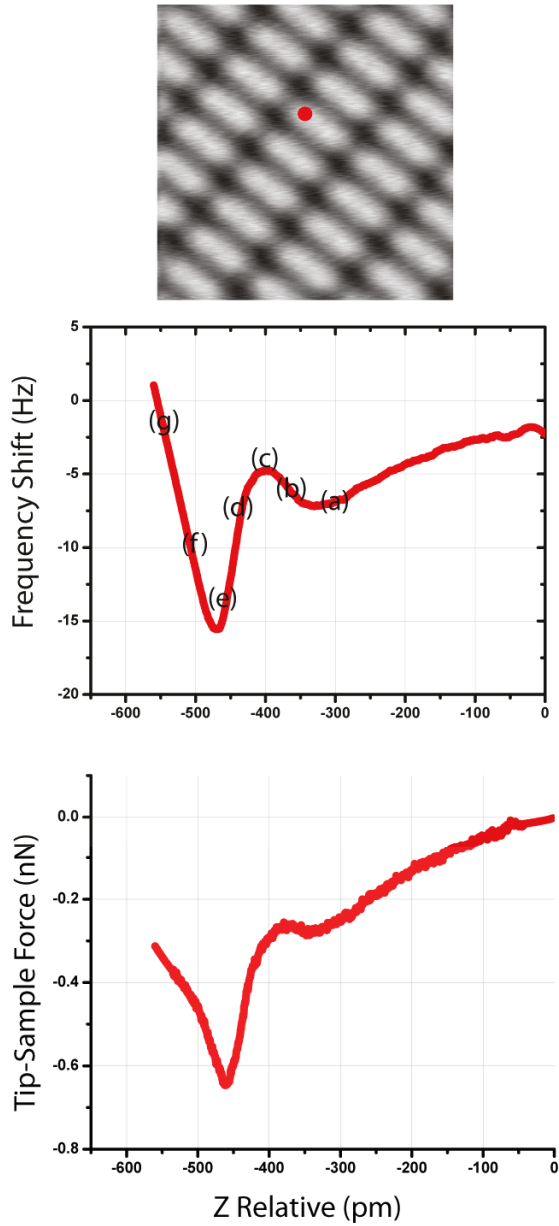
Figure 4.5: (Top) STM z-topography of a 3×3 nm area demonstrating sharpness of the tip. (Middle) Z-spectroscopy measuring Δ f as a function of z height into the surface as the sensor is approached at the location marked by the red dot in the STM image above. f_0=22645 Hz, Q=26911, A=80 pm, V=0. (Bottom) Converted force curve for the same z-spectroscopy.

73

height AFM matched with modeling [89]. It was decided an analogous study would be conducted on H:Si(100), to see if similar information could be obtained.

Select AFM images from a 20 interval sequence using the same sensor and ideal tip as Fig. 4.5 are shown in Fig. 4.6. Each image took 20 min to acquire, and corresponding positions of the images are marked on the z-spectroscopy curve in Fig. 4.5 (middle).

It is interesting to note is the evolution of the shape of the features seen from farthest tip-sample distance in (a) to closest approach in (h). In the weakly attractive part of the potential curve from (a)-(c), AFM shows the hydrogen atoms visible as dots much like STM. However, as the tip is brought closer to the sample, the AFM image evolves to preferentially display the chemical bonds in (h), with atomic structure of the atoms only somewhat visible. Intermediary steps from (d) to (g) show the gradual transition from atoms to bonds.

This data can be compared to the previously mentioned work done by Gross et al. extracting the forces over pentacene [89]. Gross found that far from the pentacene molecule, they only observed diffuse attractive frequency shifts. With decreased tip-sample separation, features slowly evolved with increasing Δf. At closest approach, Δf even became positive on parts of the image. Pentacene force curves were compared to DFT calculations with van der Waals, electrostatic, and Pauli repulsive forces accounted for. Comparing model and data, the force contribution to the images farthest from the surface were shown to be van der Waals dominant, with a small 10% electrostatic contribution and negligible repulsive forces. Fixed height images taken closer to the surface were dominated by Pauli repulsion, with van der Waals and electrostatic negligible. However, Gross concluded in the paper that images taken far from the surface in the attractive regime show little lateral corrugation on the atomic scale, and that atomic resolution on molecules in NC-AFM could only be achieved in the repulsive regime of forces. This is not the case for data shown in Fig. 4.6.

Atomic resolution was achieved on H:Si(100) in both the clearly attractive regime shown in Fig. 4.6 (a), as well as the repulsive regime in Fig. 4.6 (h). However, compared to Gross's work, separated atoms on the H:Si(100) surface are large with
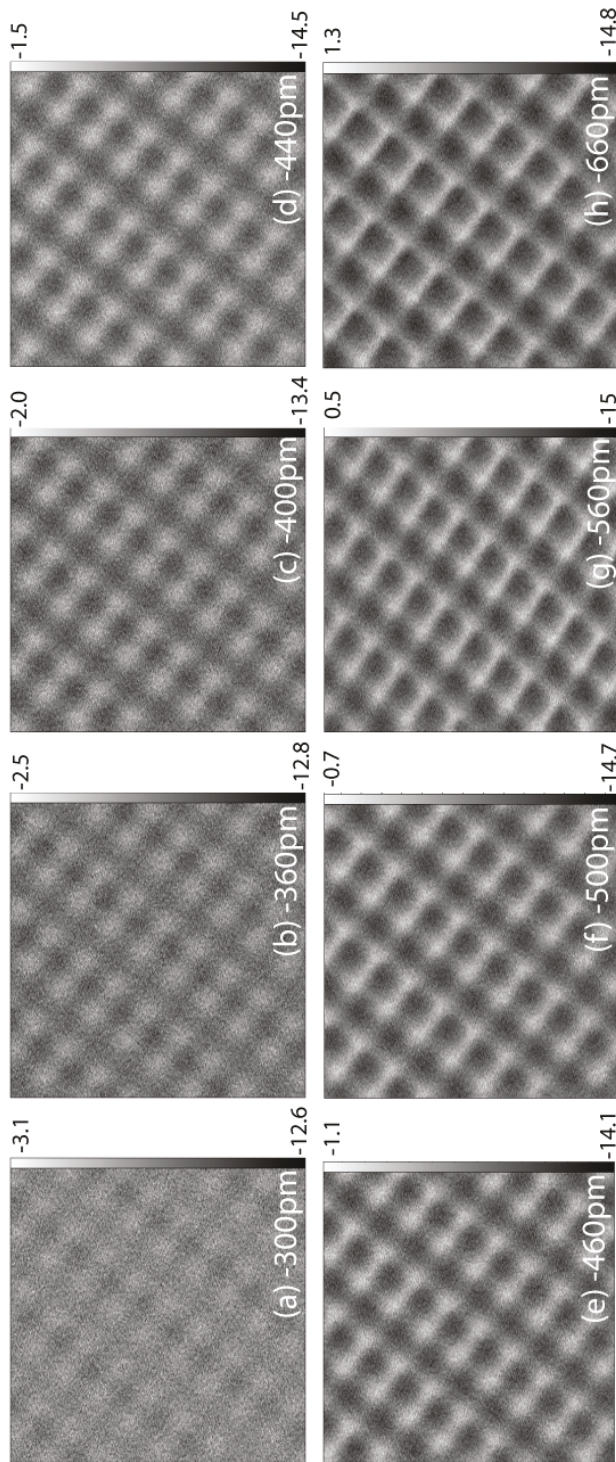
Figure 4.6: Constant height AFM images taken of the surface progressively closer to the sample. Locations of the images are marked on the z-spectroscopy in Fig. 4.5. f_0=22645 Hz, Q=26911, A=80 pm, Bias=0 V

≈ 2.3 Å spacing. Gross et al. were seeking to resolve 1-1.5 Å separated atoms.

Comparing further with Gross's work and examining the marked locations on z-spectroscopy in Fig. 4.5, images taken far from the surface on H:Si(100) are probing predominately the van der Waals force yielding an attractive potential. It is known that forces are attractive when frequency shifts are negative values. The closer the oscillating tip is brought to the surface, the more sensitive it becomes to short range chemical bond forces which include Pauli repulsion on the left side of the frequency shift minima from Fig. 4.5. The straight lined nature of the dimer rows in images obtained earlier was originally a puzzling feature, but is explained by the frequency shift being dominated near the surface by chemical bond forces. Referencing the ball-and-stick model again from Fig. 2.11 (bottom), imaging just the bonds from the top would look straight-edged. Atoms only slightly show up in (h), as chemical bond forces are considerably stronger at this distance than vdW and electrostatic. Scale bars in (g) and (h) also have positive frequency shift values, a clear sign of repulsive forces in regions of high electron density overlap. Closer approach to the surface provides the highest contrast in features, evidenced by the increasing clarity of images and scale bar ranges in Fig. 4.6.

How close the tip can be approached to the surface is limited by when a tip change occurs. If approached too close to the surface, interaction forces become sufficient to alter the tip apex decreasing or eliminating resolution altogether. The sequence in Fig. 4.6 was taken until this occurred with (h) being the last image before loss of resolution.

Measurements of this sort, differentiating regimes of forces, would not be possible with regular Si AFM cantilevers due to their low k values usually <100 N/m and high oscillation amplitudes.

This evolution of different dominant imaging force regimes for the H:Si(100) surface has never been demonstrated before and is a novel result.

4.3 Site-Specific Force Spectroscopy

With excellent atomic resolution, characterization of different locations on the surface was examined with the intent to identify localized variations in force. Force spectroscopy was also compared to theory.

Fig. 4.5 showed one example of force spectroscopy of the surface above a hydrogen atom. Location is specified on the surface as experiments revealed characteristic variation in force spectroscopy dependent on surface location; an observation also corroborated by other AFM groups on different surfaces [90] [91] [92]. Therefore, a catalog of these site-specific variations was completed with Fig. 4.7 (b) marking the examined locations. Spectroscopy shows no hysteresis, indicating no non-conservative forces at play. Additionally, both forward and backward sweeps were identical and taken for each curve, but only forward sweeps were plotted for clarity.

Four distinct profiles were found on H:Si(100) shown in Fig. 4.7. Over the hydrogen atoms in Fig. 4.7 (red curve), the force spectroscopy shows two force minimums: a deep well at z= -425 pm with F= -0.4 nN and a shallower secondary at z= -300 pm with F= -0.12 nN. Z-spectroscopy taken between dimer rows and centered in Fig. 4.7 (green curve) reveal a force profile that is more rounded in shape with a smaller absolute force value at z= -480 pm with F= -0.33 nN. Between rows where back bonds would be located on the surface, the profile is similarly gradual, but exhibits a deep negative tip sample force minimum F= -0.5 nN (blue) at z= -560 pm. Finally, between dimers in different rows Fig. 4.7 (purple), the profile is more sloped than the blue or green curves, with the force minimum F= -0.5 nN at z= -520 pm. Each location shows a characteristic force value occurring at a specific relative z location allowing differentiation of position on the surface. All results were reproducible in different locations, on different atoms and rows, and with different sharp tips. Comments can be made on the nature of the forces affecting these different locations as well.

Fig. 4.8 marks the locations of the spectroscopy on the 3D ball and stick models from Fig. 2.11. Examining the paths in Fig. 4.8 for the "Between Dimers in Different Rows" (purple) and "Out of Row" (green) locations, both occur in the valley between
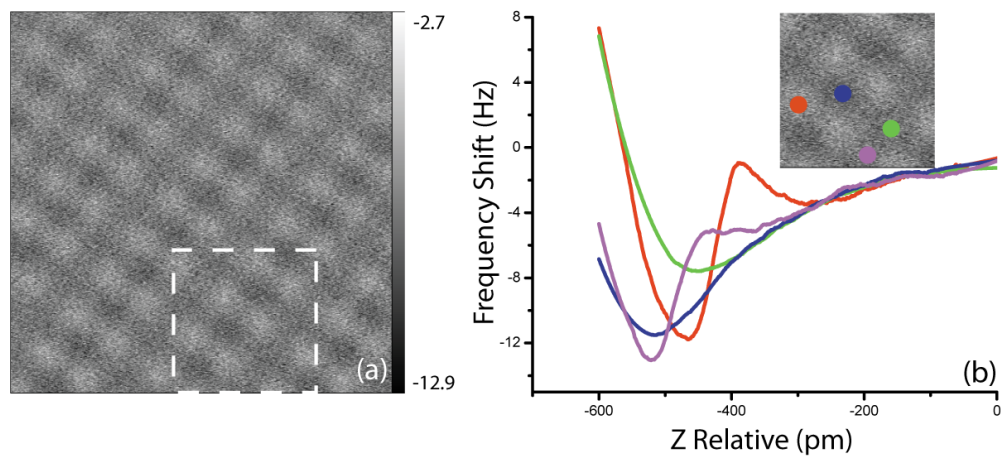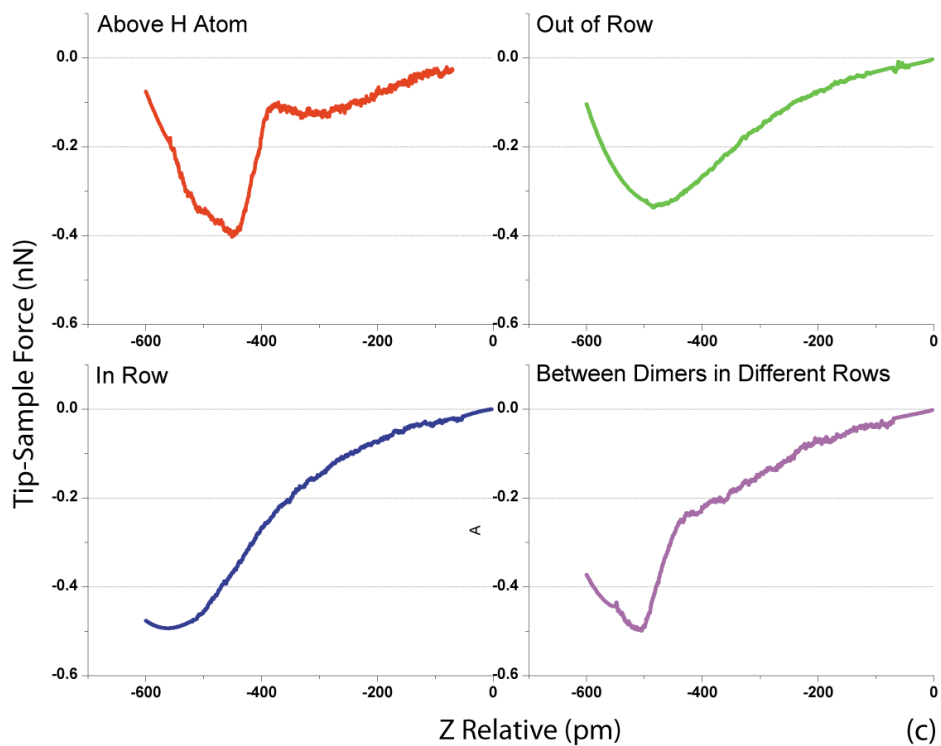
Figure 4.7: Site specific force spectroscopy on H:Si(100). (a) Constant height AFM of the surface taken with A=80 pm,V=0, f_0=22645 Hz. Spectroscopy locations are color coded and marked in (b). Frequency shift data in (b) was deconvoluted using the Sader-Jarvis code to obtain the force plots in (c) which each show unique profiles.
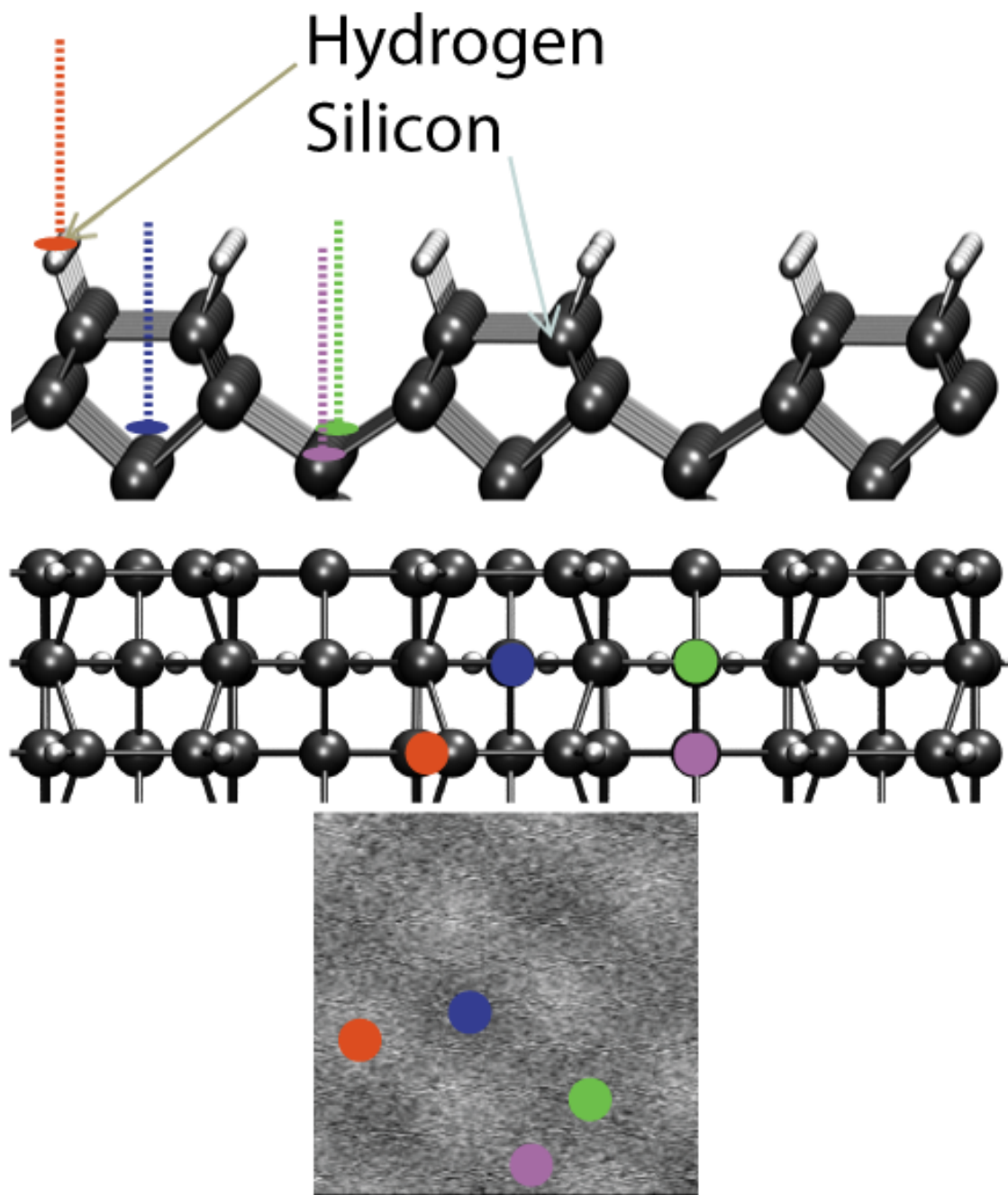
Figure 4.8: Site specific force spectroscopy locations marked on the ball and stick models for H:Si(100).

dimer rows suggesting the two might have similar force minimum values. This is not the case with force values being different at F= -0.05 nN (purple) and F= -0.33 nN (green). However, the force minimum for "In Row" (blue) does agree well with "Between Dimers in Different Rows" (purple) where F= -0.05. The fact that "In Row" (blue) is taken in a dimer row with dimer bonds around its z-spectroscopy path does not seem to affect its force minimum when compared to an unobstructed z-spectroscopy like "Between Dimers in Different Rows" (purple). However, each of the 4 cataloged locations can be seen to be uniquely placed on the surface structure.

Z-spectroscopy in Fig. 4.7 "Above the Hydrogen Atom" (red) is unique compared to the other three curves with the double well minima occurring. This is a feature never seen before in other published force spectroscopy results on other surfaces, and only shows up in experimental data above the atom. The fact that it does not occur in the other spectroscopy locations seems to exclude the idea that it is a tip geometry artifact. The source of this double well is currently under investigation.

One theory is that it could be due to the summation of two different interaction potentials. As seen in the top image in Fig. 3.3, the response curve (red) is a combination of the attractive forces (green) and repulsive forces (blue). However, above the H atom there may be a combination of two potentials: one from the hydrogen atom and one from the underlying surface silicon below as shown in Fig. 4.8. The hydrogen atoms stick out at a slight angle above the surface with a H to Si bond length of 1.50 Å and a height difference of 1.41 Å between a surface silicon and the H atom. As the tip is approached to the H:Si(100) surface over the H atom, the qPlus probes the hydrogen atom first. The smaller potential well from 0 to -375 pm in the red curve from Fig. 4.7 (c) could be the tip's reaction to the hydrogen, including an onset of Pauli repulsion for a brief time. As approached more, a threshold is reached where the hydrogen atom is pushed to the side and the onset of a tip-Si interaction begins at -375 pm. This then shows a strong attraction much like Fig. 4.7 "Between Dimers in Different Rows" (purple) until reaching the force minimum at -430 pm, after which a secondary silicon Pauli repulsion is observed. The force minimum depth of the silicon is substantially less than if the tip was approached to clean silicon, a detail that could be explained by the H atom restricting the tip-silicon

interaction be weaker.

A second theory similar to the first is a surface relaxation event; relaxation referring to small changes in the position of atoms relative to their equilibrium state. Work done by Hofer et al. [93] studied the relaxation position changes of atoms in an approached W STM tip and Au sample under zero bias. Force interactions between surface and tip caused small displacements of apex and surface atoms as brought closer, where atoms from each "reached" towards each other. These displacements were modeled to be ≈ 10 pm. Something similar could be happening with H:Si(100), where as tip and sample are approached the H atom "reaches" out to the tungsten tip causing the second potential well.

A final third theory is motivated by work done by Gross et al. in 2012 [56]. While attempting to measure bond lengths on hydrocarbons using NC-AFM, they noticed some tilting of the CO molecule they used for apex termination. Tip silicon atoms on our W tips could be exhibiting a similar tilting effect, changing the observed frequency shift. Tilting is more highly constrained for a 4-coordinate silicon atom than it would be for a CO molecule as used by Giessibl, but is still being considered as exact tip composition on the apex after in-situ sharpening is still in debate.

DFT modeling, discussed more in section 5.1, is also currently being conducted in collaboration with a theorist that should help with revealing more about the site-specific force spectroscopy. The modeling will use a relaxed slab and tip consideration for calculations, with atom tilting and different tip material combinations factored in to the simulations.

Additional experiments could also be run to test the double well. Coating the tip in an alternate material or functionalizing it with a molecule like CO as done by other groups [81] [94] and repeating the grid spectroscopy could verify if this is a tip material effect. Or, keeping a W tip but imaging a different terminated surface to attempt to replicate the phenomena and prove if specific to H:Si(100).

The uniqueness of site-specific force spectroscopy does offer immediate benefits though. With H:Si(100) being an attractive surface to deposit and examine electrically decoupled adatoms and molecules on, having these quantifiable forces has utility in background subtraction.

Background subtraction is a common method where force spectroscopy is taken both on and off the adatom or molecule of interest [62] [95]. Knowing the magnitude of background forces allows them to be subtracted from the profile of the physisorbed target of interest, giving an unbiased look. Having these values for H:Si(100) allows similar subtraction for future experiments.

How do these experimentally obtained force profiles compare to earlier theoretical works from the literature though?

4.3.1   Comparison with Literature Modeling

There is only one published modeling result available for force spectroscopy on H:Si(100). Masago et al. published a theoretical calculation paper in 2009 [21] detailing a density functional theory based tight binding (DFTB) analysis of the hydrogen terminated Si(100) surface. Fig. 4.9 shows the results from Masago for force spectroscopy taken above an H-atom in a dimer row. No other force spectroscopy locations were reported by Masago.

Comparing Masago's results in Fig. 4.9 to experimental results above the H atom in a dimer row from Fig. 4.7, the minima are comparable: Masago reports a minima of -0.5 nN of force, and experimental data shows a similar value of -0.4 nN.

However, one difference between experimental results and Masago's is the z-distance over which the chemical interaction force is apparent. Fig. 4.9 shows the first force becoming apparent at around 3.25 Å away from the surface, and spanning another 1.25 Å in before returning to a zero force from repulsive effects; a 125 pm span overall. Experimental data comparatively starts showing force effects at $\approx$ -200 pm and going until -600 pm, a span almost 4 times as large as the modeled data. However, both this comparison and the force minima values one must be tentatively treated.

The discrepancies in both can be attributed to a few factors. Masago assumes a silicon tip for DFTB modeling, whereas the experimentally used tip in Fig. 4.7 is tungsten with a coating of silicon from the in-situ tip sharpening. Modeling by Masago also made the assumption of a tip amplitude A= 16 000 pm with a spring
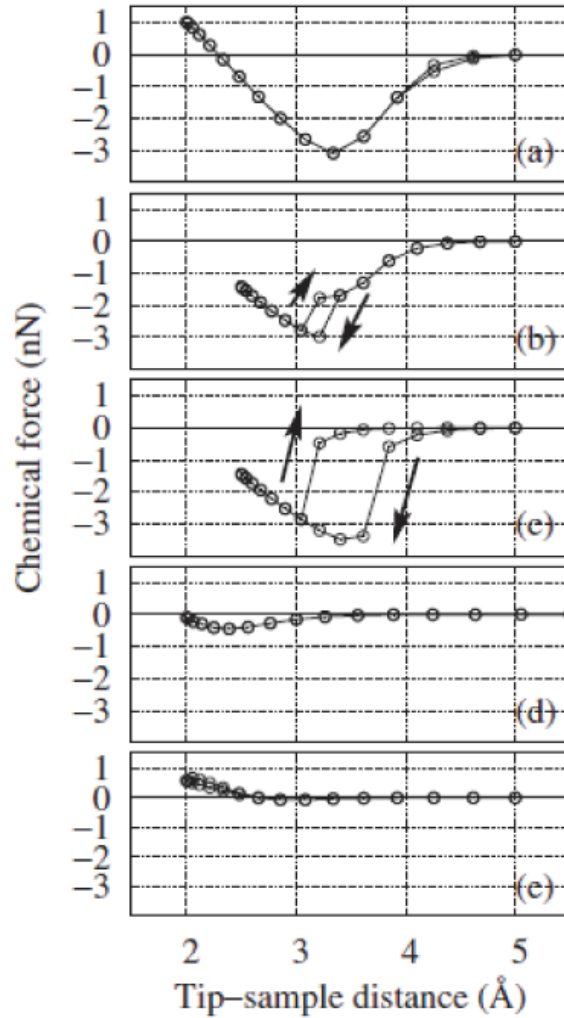
Figure 4.9: DFTB z-spectroscopy results for H:Si(100) taken from [21]. (d) is the expected force spectroscopy curve assumed to be taken above the dimer row atom. The force has a minimum of approximately -0.5 nN, with the whole well spanning from ≈ 2-3.25 Å. Curves (a),(b), (c) and (e) in the above image were for surfaces other than H:Si(100). Copyright 2009 The Japan Society of Applied Physics.

constant k=4.1 N/m for the cantilever, which may be adding in contributions from long range forces. Another difference could be in tip geometry which plays a role in the forces seen as discussed in section 2.4. Masago assumes a conical silicon tip with an apex angle of 120 ° and a 100 nm height. The tip shape for experimental data is not known.

These modeling assumptions make comparison to experimental data somewhat subject, and also provoke the need for more accurate DFT modeling with system parameters factored in. Forthcoming DFT efforts will also use more current modeling methods and better computational capabilities than those that were available to Masago in 2009.

Chapter 5

Conclusion

Non-contact atomic force microscopy has shown itself to be a powerful tool for surface characterization. Unlike STM, it allows the imaging of atoms with high resolution without the need for an applied tip sample bias. As such, it was chosen as a complementary tool to STM for analyzing H:Si(100).

As part of this analysis, AFM capabilities first had to be developed in our low-temperature ultra-high-vacuum system, and were optimized over many months of research, trial, and error. Our experimental design is suited to excellent AFM of H:Si(100) due to the stability offered by LT 4.5 K operation, the use of extra stiff piezoelectric qPlus sensors, and UHV nature, combined with our leading expertise in silicon surface physics.

With low noise imaging established, both constant height and constant frequency shift AFM images were taken on the H:Si(100) surface. The constant frequency shift image showed good resolution when compared to the only other H:Si(100) AFM image [11] also taken in constant frequency shift mode.

Constant height imaging was next explored with images taken at multiple tip-sample z-distances showing, for the first time, beautiful detailed resolution of the evolution from attractive to repulsive forces on H:Si(100). Comparison to other work revealed attractive forces to be dominantly van der Waals. Past the force minimum, Pauli repulsion dominated imaging, giving the first look at the chemical bonds on H:Si(100). These reported images were also the first ever constant height

AFM images reported on the H:Si(100) surface, showcasing our machine's ability in force probing on what is generally considered an inert and difficult to image surface, and opening the door for many future experiments.

Site-specific force spectroscopy was then examined as another surface characterization, with 4 unique profiles being cataloged on H:Si(100). Z-spectroscopy results suggest subtle variations in the cumulative interaction forces, localized to different surface sites. These have immediate application in background subtraction for unbiased examination of deposited electrically decoupled atoms or molecules.

Z-spectroscopy over the H atom on H:Si(100) was compared with a literature theoretical model [21]. Measured and modeled profiles showed good quantitative agreement in the expected force minimum which was -0.5 nN theoretically and -0.4 nN experimentally. Differentiated force measurements for different locations on the surface also suggest a high sensitivity and low noise threshold for our NC-AFM.

5.1 Future Work

AFM analysis of H:Si(100) proved to be highly detailed and revealing, but also raised further questions.

Single atom etching was done on all tips used in the presented AFM data, but no analysis was done on the affects this has on imaging quality or resolution. A study correlating AFM data to tip structure would be of interest.

Site-specific force spectroscopy above the H atom showed a unique double well. Speculation is that this extra well could be due to the summation of potential wells for the hydrogen atom and surface silicon, surface or tip relaxation, or bending of the apex atom on the tip. More experiments and modeling are needed to investigate this.

DFT modeling is currently being collaboratively investigated to provide insight into this unresolved phenomena and to better understand variations in the other site-specific z-spectroscopy locations. The more advanced DFT modeling techniques being explored currently, along with access to powerful computational resources, should provide a detailed look at the proportions of the force contributions.

The z-spectroscopy can, in the future, be extended to create large scale 3D force mapping of the surface to enable application of H:Si(100) as an electrically decoupled examination platform. This thesis has already demonstrated the ability to differentiate locations on the surface using site-specific z-spectroscopy. This concept could be extended to large scale grid analysis of the H:Si(100) surface with a generated 3D force map for precise plane subtraction from a target atom or molecule. Experiments and adaptions to the Sader-Jarvis force deconvolution code are currently underway for this.

H:Si(100) also offers up another unique ability as discussed earlier in section 1.2 which is its potential for ultra-low-power and fast electronics using DB based QCA cells. AFM can hopefully be used to examine polarization of fabricated QCA cells on the surface.

Overall, AFM has been developed a long way in our system providing revealing images of challenging features and surfaces. Continuing on in this work and extending it to DBs and DB structures on H:Si(100) will be the primary focus of my continued work, and hopefully the basis of my PhD.

Bibliography

[1] R. Wolkow, L. Livadaru, J. Pitters, M. Taucer, P. Piva, M. Salomons,
M. Cloutier, and B. Martins, "Silicon Atomic Quantum Dots Enable
Beyond-CMOS Electronics," in *Field-Coupled Nanocomputing*, N. G. Anderson
and S. Bhanja, eds., Lecture Notes in Computer Science, pp. 33–58. Springer
Berlin Heidelberg, 2014.
http://dx.doi.org/10.1007/978-3-662-43722-3_3.

[2] J. L. Pitters, L. Livadaru, M. B. Haider, and R. A. Wolkow, "Tunnel coupled
dangling bond structures on hydrogen terminated silicon surfaces," *The
Journal of chemical physics* **134** (2011) 064712.

[3] L. Livadaru, P. Xue, Z. Shaterzadeh-Yazdi, G. A. DiLabio, J. Mutus, J. L.
Pitters, B. C. Sanders, and R. A. Wolkow, "Dangling-bond charge qubit on a
silicon surface," *New Journal of Physics* **12** (2010) 083018.

[4] H. Raza, "Theoretical study of isolated dangling bonds, dangling bond wires,
and dangling bond clusters on a H: Si (001)-(2× 1) surface," *Physical Review
B* **76** (2007) 045308.

[5] M. Kepenekian, F. D. Novaes, R. Robles, S. Monturet, H. Kawai, C. Joachim,
and N. Lorente, "Electron transport through dangling-bond silicon wires on
H-passivated Si (100)," *Journal of Physics: Condensed Matter* **25** (2013)
025503.

[6] H. Kawai, F. Ample, Q. Wang, Y. K. Yeo, M. Saeys, and C. Joachim, "Dangling-bond logic gates on a Si (100)-(2× 1)–H surface," *Journal of Physics: Condensed Matter* **24** (2012) 095011.

[7] A. Bellec, F. Ample, D. Riedel, G. Dujardin, and C. Joachim, "Imaging molecular orbitals by scanning tunneling microscopy on a passivated semiconductor," *Nano letters* **9** (2008) 144–147.

[8] L. Zazzera, J. Evans, M. Deruelle, M. Tirrell, C. Kessel, and P. McKeown, "Bonding Organic Molecules to Hydrogen-Terminated Silicon Wafers," *Journal of The Electrochemical Society* **144** (1997) 2184–2189.

[9] F. Mohn, L. Gross, N. Moll, and G. Meyer, "Imaging the charge distribution within a single molecule," *Nature nanotechnology* **7** (2012) 227–231.

[10] G. A. DiLabio, E. R. Johnson, and J. Pitters, "Pentacene binds strongly to hydrogen-terminated silicon surfaces via dispersion interactions," *The Journal of Physical Chemistry C* **113** (2009) 9969–9973.

[11] K. Yokoyama, T. Ochi, A. Yoshimoto, Y. Sugawara, and S. Morita, "Atomic resolution imaging on Si (100) 2× 1 and Si (100) 2× 1: H surfaces with noncontact atomic force microscopy," *Japanese Journal of Applied Physics* **39** (2000) L113.

[12] F. Ohnesorge and G. Binnig, "True Atomic Resolution by Atomic Force Microscopy Through Repulsive and Attractive Forces," *Science* **260** (1993) 1451–1456,
http://www.sciencemag.org/content/260/5113/1451.full.pdf.
http://www.sciencemag.org/content/260/5113/1451.abstract.

[13] F. J. Giessibl, "Atomic Resolution of the Silicon (111)-(7x7) Surface by Atomic Force Microscopy," *Science* **267** (1995) 68–71,
http://www.sciencemag.org/content/267/5194/68.full.pdf.
http://www.sciencemag.org/content/267/5194/68.abstract.

[14] L. Gross, F. Mohn, N. Moll, P. Liljeroth, and G. Meyer, "The Chemical Structure of a Molecule Resolved by Atomic Force Microscopy," *Science* **325** (2009) 1110–1114, http://www.sciencemag.org/content/325/5944/1110.full.pdf. http://www.sciencemag.org/content/325/5944/1110.abstract.

[15] M. B. Haider, J. L. Pitters, G. A. DiLabio, L. Livadaru, J. Y. Mutus, and R. A. Wolkow, "Controlled Coupling and Occupation of Silicon Atomic Quantum Dots at Room Temperature," *Phys. Rev. Lett.* **102** (Jan, 2009) 046805. http://link.aps.org/doi/10.1103/PhysRevLett.102.046805.

[16] A. P. Legg, *Characterization of Point Projection Microscope for In-line Holography*. PhD thesis, University of Alberta, 2013.

[17] B. Bhushan, *Springer Handbook of Nanotechnology*. Gale virtual reference library. Springer, 2007. http://books.google.ca/books?id=MOrlqX_5fakC.

[18] E. Meyer, H. Hug, and R. Bennewitz, *Scanning Probe Microscopy: The Lab on a Tip*. Advanced Texts in Physics. Springer, 2004. http://books.google.ca/books?id=v2oy14gjzwUC.

[19] J. Welker, E. Illek, and F. J. Giessibl, "Analysis of force-deconvolution methods in frequency-modulation atomic force microscopy," *Beilstein Journal of Nanotechnology* **3** (2012) 238–248.

[20] Omicron, "Omicron Nanotechnology The LT STM User's Guide (including LT STM-Qplus AFM),".

[21] A. Masago, S. Watanabe, K. Tagami, and M. Tsukada, "Simulation of Noncontact Atomic Force Microscopy of Hydrogen- and Methyl-Terminated Si(001) Surfaces," *Japanese Journal of Applied Physics* **48** (2009) 025506. http://stacks.iop.org/1347-4065/48/i=2R/a=025506.

[22] G. Binnig, C. F. Quate, and C. Gerber, "Atomic Force Microscope," *Phys. Rev. Lett.* **56** (Mar, 1986) 930–933. http://link.aps.org/doi/10.1103/PhysRevLett.56.930.

[23] J. Tersoff and D. R. Hamann, "Theory of the scanning tunneling microscope," *Phys. Rev. B* **31** (Jan, 1985) 805–813. http://link.aps.org/doi/10.1103/PhysRevB.31.805.

[24] G. Meyer and N. M. Amer, "Optical beam deflection atomic force microscopy: The NaCl(001) surface," *Applied Physics Letters* **56** (1990) .

[25] E. Meyer, H. Heinzelmann, H. Rudin, and H.-J. Güntherodt, "Atomic resolution on LiF (001) by atomic force microscopy," *Zeitschrift fÃijr Physik B Condensed Matter* **79** (1990) 3–4. http://dx.doi.org/10.1007/BF01387818.

[26] T. R. Albrecht, P. Grütter, D. Horne, and D. Rugar, "Frequency modulation detection using high Q cantilevers for enhanced force microscope sensitivity," *Journal of Applied Physics* **69** (1991) .

[27] S. Morita, R. Wiesendanger, and E. Meyer, *Noncontact atomic force microscopy*, vol. 1. Springer, 2002.

[28] S. Kalinin and A. Gruverman, "Introduction," in *Scanning Probe Microscopy*, S. Kalinin and A. Gruverman, eds., pp. 1–8. Springer New York, 2007. http://dx.doi.org/10.1007/978-0-387-28668-6_1.

[29] R. García and R. Pérez, "Dynamic atomic force microscopy methods," *Surface Science Reports* **47** (2002) 197 − 301. http://www.sciencedirect.com/science/article/pii/S0167572902000778.

[30] W. A. Hofer, A. S. Foster, and A. L. Shluger, "Theories of scanning probe microscopes at the atomic scale," *Rev. Mod. Phys.* **75** (Oct, 2003) 1287–1331. http://link.aps.org/doi/10.1103/RevModPhys.75.1287.

[31] F. J. Giessibl, "Advances in atomic force microscopy," *Rev. Mod. Phys.* **75** (Jul, 2003) 949–983. http://link.aps.org/doi/10.1103/RevModPhys.75.949.

[32] F. Giessibl, "Principles and Applications of the qPlus Sensor," in *Noncontact Atomic Force Microscopy*, S. Morita, F. J. Giessibl, and R. Wiesendanger, eds., NanoScience and Technology, pp. 121–142. Springer Berlin Heidelberg, 2009. http://dx.doi.org/10.1007/978-3-642-01495-6_6.

[33] M. Ternes, C. P. Lutz, C. F. Hirjibehedin, F. J. Giessibl, and A. J. Heinrich, "The force needed to move an atom on a surface," *Science* **319** (2008) 1066–1069.

[34] Y. Sugimoto, P. Pou, M. Abe, P. Jelinek, R. Pérez, S. Morita, and O. Custance, "Chemical identification of individual surface atoms by atomic force microscopy," *Nature* **446** (2007) 64–67.

[35] H. Hûlscher, S. M. Langkat, A. Schwarz, and R. Wiesendanger, "Measurement of three-dimensional force fields with atomic resolution using dynamic force spectroscopy," *Applied Physics Letters* **81** (2002) .

[36] B. J. Albers, T. C. Schwendemann, M. Z. Baykara, N. Pilet, M. Liebmann, E. I. Altman, and U. D. Schwarz, "Data acquisition and analysis procedures for high-resolution atomic force microscopy in three dimensions," *Nanotechnology* **20** (2009) 264002. http://stacks.iop.org/0957-4484/20/i=26/a=264002.

[37] C. S. Lent, P. D. Tougaw, W. Porod, and G. H. Bernstein, "Quantum cellular automata," *Nanotechnology* **4** (1993) 49. http://stacks.iop.org/0957-4484/4/i=1/a=004.

[38] C. S. Lent and P. D. Tougaw, "A device architecture for computing with quantum dots," *Proceedings of the IEEE* **85** (1997) 541–557.

[39] O. Instruments, "Low Temperature UHV STM and AFM Technology," 2014.
http://www.omicron.de/en/products/low-temperature-spm/
instrument-concept.

[40] M. Rezeq, J. Pitters, and R. Wolkow, "Tungsten nanotip fabrication by
spatially controlled field-assisted reaction with nitrogen," *The Journal of
Chemical Physics* **124** (2006) –. http://scitation.aip.org/content/aip/
journal/jcp/124/20/10.1063/1.2198536.

[41] V. Ukraintsev and J. T. Y. Jr., "The role of nickel in Si(001) roughening,"
Surface Science **346** (1996) 31 – 39.
http://www.sciencedirect.com/science/article/pii/0039602895007792.

[42] A. Sherman, "Insitu removal of native oxide from silicon wafers," *Journal of
Vacuum Science and Technology B* **8** (1990) .

[43] K. Hata, T. Kimura, S. Ozawa, and H. Shigekawa, "How to fabricate a defect
free Si (001) surface," *Journal of Vacuum Science & Technology A* **18** (2000)
1933–1936.

[44] J. L. Pitters, P. G. Piva, and R. A. Wolkow, "Dopant depletion in the near
surface region of thermally prepared silicon (100) in UHV," *Journal of
Vacuum Science and Technology B* **30** (2012) –. http://scitation.aip.org/
content/avs/journal/jvstb/30/2/10.1116/1.3694010.

[45] H. Bender, S. Verhaverbeke, M. Caymax, O. Vatel, and M. Heyns, "Surface
reconstruction of hydrogen annealed (100) silicon," *Journal of Applied Physics*
75 (Jan, 1994) 1207–1209.

[46] G. Cerofolini, C. Galati, S. Reina, L. Renna, N. Spinella, D. Jones, and
V. Palermo, "Formation of terraced, nearly flat, hydrogen-terminated,(100) Si
surfaces after high-temperature treatment in H 2 of single-crystalline silicon,"
Physical Review B **72** (2005) 125431.

[47] Y. J. Chabal and K. Raghavachari, "New Ordered Structure for the H-Saturated Si(100) Surface: The," *Phys. Rev. Lett.* **54** (Mar, 1985) 1055–1058. http://link.aps.org/doi/10.1103/PhysRevLett.54.1055.

[48] C. C. Cheng and J. T. Yates, "H-induced surface restructuring on Si(100): Formation of higher hydrides," *Phys. Rev. B* **43** (Feb, 1991) 4041–4045. http://link.aps.org/doi/10.1103/PhysRevB.43.4041.

[49] J. J. Boland, "Scanning tunnelling microscopy of the interaction of hydrogen with silicon surfaces," *Advances in Physics* **42** (1993) 129–171.

[50] T. R. Albrecht, S. Akamine, T. E. Carver, and C. F. Quate, "Microfabrication of cantilever styli for the atomic force microscope," *Journal of Vacuum Science and Technology A* **8** (1990) 3386–3396. http://scitation.aip.org/content/avs/journal/jvsta/8/4/10.1116/1.576520.

[51] F. J. Giessibl, "High-speed force sensor for force microscopy and profilometry utilizing a quartz tuning fork," *Applied Physics Letters* **73** (Dec., 1998) 3956.

[52] J. C. Brice, "Crystals for quartz resonators," *Rev. Mod. Phys.* **57** (Jan, 1985) 105–146. http://link.aps.org/doi/10.1103/RevModPhys.57.105.

[53] L. Beaulieu, M. Godin, O. Laroche, V. Tabard-Cossa, and P. Grütter, "A complete analysis of the laser beam deflection systems used in cantilever-based systems," *Ultramicroscopy* **107** (2007) 422 – 430. http://www.sciencedirect.com/science/article/pii/S0304399106001987.

[54] R. Pérez, M. C. Payne, I. Štich, and K. Terakura, "Role of Covalent Tip-Surface Interactions in Noncontact Atomic Force Microscopy on Reactive Surfaces," *Phys. Rev. Lett.* **78** (Jan, 1997) 678–681. http://link.aps.org/doi/10.1103/PhysRevLett.78.678.

[55] P. Dieška, I. Štich, and R. Pérez, "Covalent and Reversible Short-Range Electrostatic Imaging in Noncontact Atomic Force Microscopy," *Phys. Rev.*

Lett. **91** (Nov, 2003) 216401.
http://link.aps.org/doi/10.1103/PhysRevLett.91.216401.

[56] L. Gross, F. Mohn, N. Moll, B. Schuler, A. Criado, E. Guitián, D. Peña, A. Gourdon, and G. Meyer, "Bond-Order Discrimination by Atomic Force Microscopy," *Science* **337** (2012) 1326–1329, http://www.sciencemag.org/content/337/6100/1326.full.pdf. http://www.sciencemag.org/content/337/6100/1326.abstract.

[57] G. Teobaldi, K. Lämmle, T. Trevethan, M. Watkins, A. Schwarz, R. Wiesendanger, and A. L. Shluger, "Chemical Resolution at Ionic Crystal Surfaces Using Dynamic Atomic Force Microscopy with Metallic Tips," *Phys. Rev. Lett.* **106** (May, 2011) 216102. http://link.aps.org/doi/10.1103/PhysRevLett.106.216102.

[58] T. Trevethan, M. Watkins, and A. L. Shluger, "Models of the interaction of metal tips with insulating surfaces," *Beilstein Journal of Nanotechnology* **3** (2012) 329–335.

[59] R. Smoluchowski, "Anisotropy of the Electronic Work Function of Metals," *Phys. Rev.* **60** (Nov, 1941) 661–674. http://link.aps.org/doi/10.1103/PhysRev.60.661.

[60] M. Rezeq, J. Pitters, and R. Wolkow, "Tungsten nanotip fabrication by spatially controlled field-assisted reaction with nitrogen," *The Journal of Chemical Physics* **124** (2006) –. http://scitation.aip.org/content/aip/journal/jcp/124/20/10.1063/1.2198536.

[61] R. Urban, J. L. Pitters, and R. A. Wolkow, "Gas field ion source current stability for trimer and single atom terminated W(111) tips," *Applied Physics Letters* **100** (2012) –. http://scitation.aip.org/content/aip/journal/apl/100/26/10.1063/1.4726112.

[62] L. Gross, F. Mohn, P. Liljeroth, J. Repp, F. J. Giessibl, and G. Meyer, "Measuring the charge state of an adatom with noncontact atomic force microscopy," *Science* **324** (2009) 1428–1431.

[63] R. Stomp, Y. Miyahara, S. Schaer, Q. Sun, H. Guo, P. Grutter, S. Studenikin, P. Poole, and A. Sachrajda, "Detection of single-electron charging in an individual InAs quantum dot by noncontact atomic-force microscopy," *Physical review letters* **94** (2005) 056802.

[64] O. L. Guise, J. W. Ahner, M.-C. Jung, P. C. Goughnour, and J. T. Yates, "Reproducible electrochemical etching of tungsten probe tips," *Nano Letters* **2** (2002) 191–193.

[65] B.-F. Ju, Y.-L. Chen, and Y. Ge, "The art of electrochemical etching for preparing tungsten probes with controllable tip profile and characteristic parameters," *Review of Scientific Instruments* **82** (2011) 013707.

[66] V. T. Binh, N. Garcia, and S. Purcell, "Electron Field Emission from Atom-Sources: Fabrication, Properties, and Applications of Nanotips," vol. 95 of *Advances in Imaging and Electron Physics*, pp. 63 – 153. Elsevier, 1996. http://www.sciencedirect.com/science/article/pii/S1076567008701563.

[67] H.-W. Fink, "Point source for ions and electrons," *Physica Scripta* **38** (1988) 260. http://stacks.iop.org/1402-4896/38/i=2/a=029.

[68] J. L. Pitters, R. Urban, C. Vesa, and R. A. Wolkow, "Tip apex shaping of gas field ion sources," *Ultramicroscopy* **131** (2013) 56 – 60. http://www.sciencedirect.com/science/article/pii/S0304399113000831.

[69] E. W. Müller and K. Bahadur, "Field Ionization of Gases at a Metal Surface and the Resolution of the Field Ion Microscope," *Phys. Rev.* **102** (May, 1956) 624–631. http://link.aps.org/doi/10.1103/PhysRev.102.624.

[70] R. G. Forbes, "Field electron and ion emission from charged surfaces: a strategic historical review of theoretical concepts," *Ultramicroscopy* **95** (2003) 1 – 18. http://www.sciencedirect.com/science/article/pii/S0304399102002930. {IFES} 2001.

[71] F. J. Giessibl, "Forces and frequency shifts in atomic-resolution dynamic-force microscopy," *Phys. Rev. B* **56** (Dec, 1997) 16010–16015. http://link.aps.org/doi/10.1103/PhysRevB.56.16010.

[72] F. J. Giessibl, S. Hembacher, M. Herz, C. Schiller, and J. Mannhart, "Stability considerations and implementation of cantilevers allowing dynamic force microscopy with optimal resolution: the qPlus sensor," *Nanotechnology* **15** (2004) S79. http://stacks.iop.org/0957-4484/15/i=2/a=017.

[73] F. J. Giessibl and H. Bielefeldt, "Physical interpretation of frequency-modulation atomic force microscopy," *Phys. Rev. B* **61** (Apr, 2000) 9968–9971. http://link.aps.org/doi/10.1103/PhysRevB.61.9968.

[74] H. Hölscher, A. Schwarz, W. Allers, U. Schwarz, and R. Wiesendanger, "Quantitative analysis of dynamic-force-spectroscopy data on graphite (0001) in the contact and noncontact regimes," *Physical Review B* **61** (2000) 12678.

[75] Nanonis, "Piezoelectric Quartz Tuning Forks for Scanning Probe Microscopy,". http://www.specs-zurich.com/upload/cms/user/TF2.pdf.

[76] U. Dürig, H. R. Steinauer, and N. Blanc, "Dynamic force microscopy by means of the phase-controlled oscillator method," *Journal of Applied Physics* **82** (1997) .

[77] L. Olsson, N. Lin, V. Yakimov, and R. Erlandsson, "A method for in situ characterization of tip shape in ac-mode atomic force microscopy using electrostatic interaction," *Journal of applied physics* **84** (1998) 4060–4064.

[78] G. Binnig and H. Rohrer, "Scanning tunneling microscopy¯from birth to adolescence," *Rev. Mod. Phys.* **59** (Jul, 1987) 615–625. http://link.aps.org/doi/10.1103/RevModPhys.59.615.

[79] S.-W. Hla, "Scanning tunneling microscopy single atom/molecule manipulation and its application to nanoscience and technology," *Journal of Vacuum Science & Technology B* **23** (2005) 1351–1360.

[80] L. Gross, F. Mohn, N. Moll, P. Liljeroth, and G. Meyer, "The chemical structure of a molecule resolved by atomic force microscopy," *Science* **325** (2009) 1110–1114.

[81] N. Moll, L. Gross, F. Mohn, A. Curioni, and G. Meyer, "The mechanisms underlying the enhanced resolution of atomic force microscopy with functionalized tips," *New Journal of Physics* **12** (2010) 125020. http://stacks.iop.org/1367-2630/12/i=12/a=125020.

[82] M. Guggisberg, *Lokale Messung von atomaren KrÃÂď ften*. PhD thesis, University of Basel, 2000.

[83] J. E. Sader and S. P. Jarvis, "Accurate formulas for interaction force and energy in frequency modulation force spectroscopy," *Applied Physics Letters* **84** (2004) .

[84] S. Morita and Y. Sugawara, "Atomically Resolved Imaging of Si(100) 2x1, 2x1:H and 1x1:2H Surfaces with Noncontact Atomic Force Microscopy," *Japanese Journal of Applied Physics* **41** (2002) 4857. http://stacks.iop.org/1347-4065/41/i=7S/a=4857.

[85] F. Mohn, L. Gross, and G. Meyer, "Measuring the short-range force field above a single molecule with atomic resolution," *Applied Physics Letters* **99** (2011) 053106.

[86] S. Hembacher, F. J. Giessibl, and J. Mannhart, "Force Microscopy with Light-Atom Probes," *Science* **305** (2004) 380–383,

`http://www.sciencemag.org/content/305/5682/380.full.pdf`.
`http://www.sciencemag.org/content/305/5682/380.abstract`.

[87] S.-i. Kitamura and M. Iwatsuki, "Observation of 7×7 reconstructed structure on the silicon (111) surface using ultrahigh vacuum noncontact atomic force microscopy," *Japanese journal of applied physics* **34** (1995) L145.

[88] F. J. Giessibl, S. Hembacher, H. Bielefeldt, and J. Mannhart, "Subatomic features on the silicon (111)-(7×7) surface observed by atomic force microscopy," *Science* **289** (2000) 422–425.

[89] L. Gross, F. Mohn, P. Liljeroth, J. Repp, F. J. Giessibl, and G. Meyer, "Measuring the Charge State of an Adatom with Noncontact Atomic Force Microscopy," *Science* **324** (2009) 1428–1431, `http://www.sciencemag.org/content/324/5933/1428.full.pdf`. `http://www.sciencemag.org/content/324/5933/1428.abstract`.

[90] M. P. Boneschanscher, J. van der Lit, Z. Sun, I. Swart, P. Liljeroth, and D. Vanmaekelbergh, "Quantitative Atomic Resolution Force Imaging on Epitaxial Graphene with Reactive and Nonreactive AFM Probes," *ACS Nano* **6** (2012) 10216–10221, `http://dx.doi.org/10.1021/nn3040155`. `http://dx.doi.org/10.1021/nn3040155`. PMID: 23039032.

[91] L. Gross, "Recent advances in submolecular resolution with scanning probe microscopy," *Nature chemistry* **3** (2011) 273–278.

[92] J. Welker, A. J. Weymouth, and F. J. Giessibl, "The Influence of Chemical Bonding Configuration on Atomic Identification by Force Spectroscopy," *ACS Nano* **7** (2013) 7377–7382, `http://dx.doi.org/10.1021/nn403106v`. `http://dx.doi.org/10.1021/nn403106v`. PMID: 23841516.

[93] W. Hofer, A. Fisher, R. Wolkow, and P. Grütter, "Surface Relaxations, Current Enhancements, and Absolute Distances in High Resolution Scanning Tunneling Microscopy," *Phys. Rev. Lett.* **87** (Nov, 2001) 236104. `http://link.aps.org/doi/10.1103/PhysRevLett.87.236104`.

[94] M. Schneiderbauer, M. Emmrich, A. J. Weymouth, and F. J. Giessibl, "CO Tip Functionalization Inverts Atomic Force Microscopy Contrast via Short-Range Electrostatic Forces," *Physical review letters* **112** (2014) 166102.

[95] S. Morita, "Atom world based on nano-forces: 25 years of atomic force microscopy," *Journal of Electron Microscopy* **60** (2011) S199–S211.

Appendices

Appendix A

Sader Jarvis Frequency Shift to Force Conversion Code

```
import pylab as pb
import numpy
import math
import numpy as np
from numpy import matrix
import matplotlib.pyplot as plt
f_0=22645.0 #resonance frequency (Hz)
k=1800.0 #spring constant of Cantilever. (N/m)
A=80*10**(-12) #Scanning amplitude used.
pb.clf()
ForceData=open("ForceData.txt","w")
f=open("filename.dat",'r')
for x in range(0):f.readline() #skip header
data=f.readlines() #reads the .dat file in line by line.
zrel=[] #lists for all variables in the file
Delta_f=[]
for line in data: # for each line read into "data" split it when you see a space
```

and put into the lists above

line=line.split()

zrel.append(float(line[0])) #add to the "zrel" list whatever is in the first column

Delta_f.append(float(line[1]))

zrel=np.array(zrel) #redefine all as numpy arrays and arrange so zi is closer to the surface than z(i+1) by flipping the order

Delta_f=np.array(Delta_f)

Omega = np.array([x/f_0 for x in Delta_f])

dOmega_dz=np.array(np.diff(Omega)/np.diff(zrel))

N=len(dOmega_dz)

zrel=zrel[0:N] #appends the size of the array to match dOmega_dz so all the same length. dOmega_dz is less in length than the original due to the subtractions between values.

Delta_f=Delta_f[0:N]

Omega=Omega[0:N]

F=numpy.zeros(np.size(zrel)-2)

for j in range (0,np.size(zrel)-3): #Loop that calculates the Force values

t= zrel[(j+1):] #Skip the first zrel value to avoid a division by zero later in the integral variable

Omega_tmp=np.array(Omega[(j+1):])

dOmega_dz_tmp=np.array(dOmega_dz[(j+1):])

integral=np.trapz((1.0+np.sqrt(A)/(8.0*np.sqrt(np.pi* (t-zrel[j]))))*Omega_tmp-(A**(3.0/2.0)/np.sqrt(2.0*(t-zrel[j]))*dOmega_dz_tmp),x=t) #Trapezoidal approximation of eq 3.30 as shown in eq 3.31

corr1 = Omega[j]*(zrel[j+1]-zrel[j]) #Correction terms for the trapezoidal approx as shown in eq 3.32

corr2 = 2.0*(np.sqrt(A)/(8.0*np.sqrt(np.pi)))*Omega[j]*np.sqrt(zrel[j+1]-zrel[j])

corr3 = (-2.0)*((np.sqrt(A))**3/np.sqrt(2.0))*dOmega_dz[j]*np.sqrt(zrel[j+1]-zrel[j])

F[j]=2*k*(corr1+corr2+corr3+integral);

zrel2=zrel[0:len(F)] #Match length of z values to F values

N2=np.size(F)

103

```
    for i in range(0,N2-1): #Write force and z data to file.
    ForceData.write("\n" + str(F[i])+"\t"+str(zrel2[i])) #Convert to string, then
use + to concatenate.
    plt.plot(zrel2/(1.0*10**(-12)), F/(1.0*10**(-9)), 'ko-') #Converts force into nN
and z into pm for plotting
    plt.title('Tip-Sample Force')
    plt.ylabel('Force Tip Sample (nN)')
    plt.xlabel('Zrel (pm)')
    plt.show()
```